

Electrical Conductivity and Hydrogen Diffusion in Synthetic Orthopyroxene Single-Crystals

Dissertation

zur Erlangung des mathematisch-naturwissenschaftlichen Doktorgrades

”Doctor rerum naturalium”

der Georg-August-Universität Göttingen

vorgelegt von

Elke Schlechter

aus Gehrden

Göttingen 2011

Referent: Prof. Dr. Roland Stalder

Institut für Mineralogie und Petrographie, Universität Innsbruck

Koreferentin: Prof. Dr. Sharon Webb

Abteilung Experimentelle und Angewandte Mineralogie, Geozentrum der Universität Göttingen

Tag der mündlichen Prüfung: 17.02. 2011

Abstract

Charge transport mechanisms and the proton contribution to electrical conductivity of synthetic orthopyroxene single crystals could be inferred by combining results from hydrogen diffusivity and electrical conductivity experiments.

Dehydration experiments were conducted with aluminous enstatite and orthopyroxenes with three different Fe/Al-ratios. The results confirm the earlier finding that iron enhances dehydration by charge-balancing escaping hydrogen with a counter flux of electron holes, enabling hydrogen to diffuse independently on its associated defect. The conjecture that aluminium decelerates dehydration by forming comparably stable hydrous point defect complexes, was also confirmed.

H/D-exchange experiments were conducted with pure and aluminous enstatite, and one Fe- and Al-bearing orthopyroxene. In orthopyroxene with 0-3 wt% FeO total iron, H/D-exchange is about two orders of magnitude faster than dehydration. In orthopyroxene with 6-10 wt% FeO total iron, dehydration is similar to H/D-exchange in pure enstatite, indicating that hydrogen diffuses independently from the associated point defect in both cases. Like dehydration, H/D-exchange is decelerated by aluminium with respect to pure enstatite, reflecting the greater stability of hydrogen associated with aluminium.

Electrical conductivity of synthetic and natural hydrogen-bearing orthopyroxene showed little correlation with hydrogen content in iron-free enstatite, and no correlation in iron-bearing orthopyroxenes. Comparing activation energies of electrical conductivity and hydrogen diffusion, three conduction mechanisms could be deduced: proton conduction, polaron conduction arising from iron redox processes, and ionic conduction via octahedral vacancies. In orthopyroxenes with >5 wt% FeO total iron, proton and polaron conduction are coupled, and polaron conduction is the major charge transport mechanism; compared to low-iron and iron-free enstatite, electrical conductivity is 0.5-1 order of magnitude higher. For lower iron content, the proton conduction mechanism is similar to H/D-exchange diffusion in pure enstatite. Although the aluminous enstatites contained up to ten times more hydrogen than the pure enstatites, both have very similar electrical conductivities, indicating that the fraction of hydrogen incorporated in association with aluminium does not contribute to electrical conduction.

Contents

Abstract	i
1. Introduction	1
1.1. Aim of the study and structure of the thesis	1
1.2. Hydrogen in Earth's Upper Mantle	2
1.3. H-incorporation and FTIR-spectra of orthopyroxene	9
2. Synthesis and preparation	15
2.1. Synthesis of orthopyroxene	15
2.2. Sample preparation	16
3. Chemical characterisation of samples	19
3.1. Chemical composition — electron microprobe analysis	19
3.2. Fe(II)- and Fe(III)-content — Mößbauer spectroscopy	22
3.3. H ₂ O-content — FTIR-spectroscopy	23
I. Hydrogen Diffusion in Orthopyroxene	27
4. Introduction	29
5. Diffusion experiments	31
5.1. Dehydration experiments	35
5.2. H/D-exchange experiments	35
5.3. Evaluation of IR-spectra of annealed samples	41
6. Results of hydrogen extraction experiments	47
7. Results of H/D-exchange experiments	55
8. Discussion	63

II. Electrical conductivity of Enstatite	69
9. Introduction	71
10. Impedance spectroscopy	73
11. Experimental setup	79
12. Results	85
13. Discussion	95
13.1. Comparison with earlier studies	96
13.2. Applicability to Earth's upper mantle	100
 III. Modelling electrical conductivity with the diffusivity of hydrogen	 107
14. Charge carriers and transport mechanisms	109
15. Modelling electrical conductivity	115
15.1. Pure enstatite	116
15.2. Al-bearing enstatite	119
15.3. Fe- and Al-bearing orthopyroxene	124
16. Conclusions	131
A. Syntheses and mineral formulas	133
B. Diffusion experiments	137
B.1. Dehydration experiments	137
B.2. H/D-exchange experiments	158
C. Electrical conductivity	175

1. Introduction

1.1. Aim of the study and structure of the thesis

Since hydrogen enhances the electrical conductivity of various nominally anhydrous minerals (NAMs) of the upper mantle (e.g., [Wang et al. \(2006\)](#); [Yoshino et al. \(2006\)](#); [Wang et al. \(1999\)](#); [Dai and Karato \(2009a\)](#)) highly electrically conductive regions in Earth's mantle were often explained with this phenomenon (e.g., [Karato \(1990\)](#); [Lizzaralde et al. \(1995\)](#); [Hirth et al. \(2000\)](#)). However, further constraints are needed to quantify the influence of hydrogen on electrical conductivity of NAMs and of Earth's mantle, because so far existing laboratory studies are inconsistent.

The aim of this study is to investigate the mobility and transport mechanisms of hydrogen and the influence of hydrogen on electrical conductivity in orthopyroxene, an abundant mineral of the upper mantle. The approach of this study is to compare hydrogen diffusivity and electrical conductivity in order to draw conclusions about charge transport mechanisms and the protonic contribution to electrical conduction.

The electrical conductivity of synthetic and natural hydrogen-bearing orthopyroxene single crystals was measured with impedance spectroscopy at ambient pressure and in hydrogen gas-flow. Dehydration experiments and H/D-exchange experiments were conducted in a variety of synthetic single crystals, such as pure enstatite, Al-bearing, and Fe-bearing orthopyroxenes. The H/D-exchange experiments, partly conducted during electrical conductivity measurements, allowed direct comparison of hydrogen mobility and electrical conductivity and to deduce the protonic contribution to electrical conduction. Conclusions about transport mechanisms and -kinetics of hydrogen-related

1. Introduction

point defects could be drawn from the comparison of hydrogen diffusivity in pure enstatite and orthopyroxenes doped with Fe, Al, and Al+Fe.

In the first part of the thesis, the hydrogen diffusion experiments are described and hydrogen incorporation and transport mechanisms are discussed. The second part deals with the electrical conductivity measurements; results are discussed and compared to earlier studies. The third part combines the results from the first and the second part, to mathematically model electrical conductivity results with diffusivities of hydrogen, polarons, and octahedral vacancies.

1.2. Hydrogen in Earth's Upper Mantle

The upper mantle extends from the Moho at 30-80 km depth below continental crust and at 5-7 km below oceanic crust down to the transition zone at about 410 km depth. The boundaries of the upper mantle are marked by a change in seismic wave velocity arising from density contrasts. At the Moho, the change is caused by the density contrast between the continental crust (mean density of 2.8 g/cm³) and mantle peridotite (mean density of 3.2 g/cm³). At the 410 km discontinuity olivine changes to the denser modification wadsleyite. At ~520 km wadsleyite changes to ringwoodite, which in turn breaks down to perovskite and ferropericlase at about 660 km depth, giving rise to the 660 km seismic discontinuity which marks the lower boundary of the transition zone (Fig 1.1). Assuming the pyrolite composition, ortho- and clinopyroxene are abundant in the uppermost 100 km of the mantle and, with increasing pressure, are transformed more and more into the majorite component of garnet. Orthopyroxene completely disappears at depth below ~350 km.

Chemically homogeneous MORB compositions with respect to major elements suggest a chemically homogeneous depleted upper mantle which is convectively stirred (e.g., [Hofmann \(1997\)](#)). [Meibom and Anderson \(2003\)](#) suggest an alternative model in which a depleted mantle is mixed with relatively small

1.2. Hydrogen in Earth's Upper Mantle

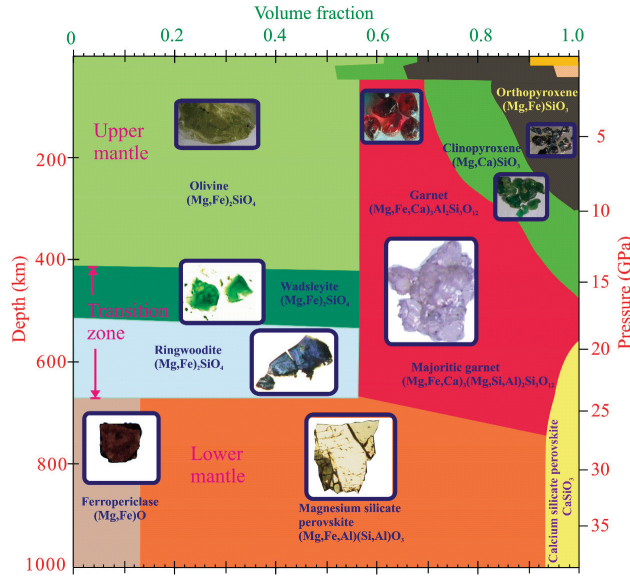


Figure 1.1.: Mineralogical composition of Earth's mantle; the figure was copied from [Frost \(2008\)](#)

parts of subducted oceanic crust on length scales 10^2 - 10^5 m and the source region of basaltic melts averages over these two components. The fact that basaltic rocks are homogeneous in major element composition but variable in trace element and radiogenic isotope composition shows that incompatible elements are more heterogeneously dispersed in the MORB source regions, reflecting their higher mobility ([Frost, 2008](#)). Hydrogen can also be considered a mobile incompatible element, and water contents in Earth's mantle vary likely both radially and laterally.

The water rich exosphere originates from volcanic outgassing of water. A substantial amount of water is recycled from the exosphere into the mantle with subducted oceanic crust via sea-floor sediments and serpentinised lithospheric mantle (e.g. [Kerrick and Connolly \(2001\)](#)). Pore water and water from decomposing hydrous minerals is released from the sediments. A part of this water causes serpentinisation of the subducted lithospheric mantle, a process which enables water transport to greater depth ([Ranero et al., 2003](#); [Rüpke](#)

1. Introduction

[et al., 2004](#)). The subducted crustal rocks are dehydrated further and eclogitised at greater depth in the mantle. Some of the released water causes partial melting in the overlying mantle wedge and generates arc volcanism in the obducted plate. Some water is transported further down and is incorporated into the minerals of the upper mantle and transition zone. It is controversial how much water resides in the mantle and how it is distributed.

In nominally anhydrous minerals (NAMs), hydrogen is incorporated as hydroxyl and causes point defects. In olivine, hydrogen might also form planar defects of the humite type ([Kitamura et al., 1987](#)). In pyroxenes, hydrogen related point defects form complexes with trivalent cation-related point defects. The hydrogen solubility is therefore enhanced by doping pyroxenes with trivalent cations, such as ferric iron, chromium, and aluminium. Aluminium incorporation in orthopyroxenes particularly enhances the hydrogen solubility in orthopyroxenes ([Stalder, 2004](#)). It has been argued that hydrogen related point defects in NAMs are the major repository for water in Earth’s mantle ([Bell and Rossman, 1992](#)). Concentrations of hydrogen in natural upper mantle peridotite xenoliths amount to 0-194 ppm-wt H₂O in olivine, 39-460 ppm-wt H₂O in orthopyroxene, and 140-957 ppm-wt H₂O in clinopyroxene ([Peslier, 2010](#)). Clinopyroxene typically contains twice as much water as orthopyroxene and olivine hosts about one tenth of the clinopyroxene’s water content. It is questionable, whether water concentrations in mantle xenoliths represent the actual upper mantle water concentrations, because dehydration profiles observed in olivine indicate partial re-equilibration of xenoliths during their ascent ([Demouchy et al., 2006](#); [Peslier and Luhr, 2006](#)). On the other hand, [Peslier \(2010\)](#) pointed out that dehydration profiles were observed only in olivine and never in the associated pyroxenes. Kinetics of hydration in iron-bearing San Carlos olivine along the fastest crystallographic direction [100] ([Kohlstedt and Mackwell, 1998](#)) is about 0.5 log units higher than dehydration along the fastest direction [001] in mantle orthopyroxene from Kilbourne Hole, which is the fastest dehydration diffusivity of pyroxenes available up to now ([Stalder and](#)

1.2. Hydrogen in Earth's Upper Mantle

Skogby, 2003). Dehydration in synthetic orthopyroxene (Stalder et al. (2007), this study) and diopside (Ingrin et al., 1995; Hercule and Ingrin, 1999; Carpenter Woods et al., 2000) is several log units lower. It may be concluded that hydrogen contents of the upper mantle might rather be inferred from the pyroxenes in xenoliths as long as the individual crystals do not exhibit a dehydration profile. However, dehydration and hydration kinetics in pyroxenes are still high enough to enable re-equilibration of minerals in a mantle xenolith with the host magma within days.

The common model for water contents of Earth's mantle is based on observations from mantle xenoliths, basaltic melts and experimentally determined hydrogen solubilities in mantle minerals. Water contents in the upper mantle probably increase with depth from ~ 200 ppm-wt H_2O at the MOHO to ~ 4000 ppm-wt H_2O at ~ 410 km depth (Bolfan-Casanova, 2005). The transition zone is believed to host about ten times more water than the upper mantle; the hydrogen storage capacity of wadsleyite and ringwoodite was experimentally determined to be 2-3 wt% H_2O at relevant P-T-conditions (Kohlstedt et al., 1996; Smyth et al., 1997). Solubility of water in lower mantle minerals — perovskites and ferropericlase — is low, i.e., <10 ppm-wt H_2O in Mg-perovskite and <20 ppm-wt H_2O in ferropericlase. Furthermore, it was found to be negatively correlated with temperature (Bolfan-Casanova et al., 2000, 2002, 2003). This suggests much lower water contents in the lower mantle than in the transition zone and in the upper mantle but this is controversial due to experimental difficulties.

If more water is present than can be incorporated into the minerals, a water-rich fluid phase or a hydrous silicate melt may form. A review on water induced partial melting in the mantle is provided by Hirschmann (2006). When partial melting occurs, hydrogen strongly partitions from the minerals into the melt; for example Tenner et al. (2009) estimated the partition coefficient between peridotite and coexisting melt to be 0.01-0.005 at upper mantle conditions. This suggests that partial melts potentially have a large influence on the con-

1. Introduction

centration and distribution of water in the mantle.

An important topic with implications for geophysical observations is the influence of hydrogen related point defects on physical properties of NAMs, comprising essentially the enhancement of all kinds of transport mechanisms in the minerals, including plastic deformation, through the weakening of interatomic bonds and causing of point defects. In silicates, hydrogen forms hydrogen bonds with two oxygen atoms, where one oxygen atom accepts an electron from the hydrogen atom and the positively charged proton attracts a second adjacent oxygen atom. In crystals, the hydrogen bond length, or alternatively the bond strength, depends on the distance between the two oxygen atoms in the undisturbed lattice. Hence, the mobility of hydrogen depends on the incorporation mechanism which determines its position in the crystal lattice. The interatomic bonds in the vicinity are disturbed and weakened through the formation of hydrogen bonds and the associated point defects.

The influence of hydrogen related point defects on the macroscopic rheology of mantle rocks persists in the reduction of shear strength (e.g., [Hirth and Kohlstedt \(1996\)](#); [Mei and Kohlstedt \(2000a,b\)](#); [Dixon et al. \(2004\)](#); [Chen et al. \(2006\)](#)) and in a change and enhancement of lattice preferred orientation of minerals through shear strain, causing a rheologic anisotropy (e.g., [Jung and Karato \(2001\)](#)). The presence of hydrogen, either in a fluid phase or incorporated into the minerals, also lowers the melting temperature of minerals, influencing the mechanical properties of mantle rocks by triggering partial melting (e.g., [Gaetani and Grove \(1998\)](#); [Asimow et al. \(2004\)](#); [Médard and Grove \(2008\)](#)). Therefore, seismic wave attenuation and seismic anisotropy might indicate the presence of hydrogen ([Karato and Jung, 1998](#); [Shito et al., 2006](#)). When the minerals become anelastic through hydrogen-induced weakening, seismic waves are attenuated due to energy dissipation. The anisotropic effect of hydrogen on anelasticity ([Mackwell et al., 1985](#)) as well as the anisotropic texture of sheared mantle rocks are possible explanations for seismic anisotropy ([Karato et al., 2008](#)).

1.2. Hydrogen in Earth's Upper Mantle

The weakening of interatomic bonds enhances the mobility of cations in mantle minerals. This is reflected by the enhancement of radiative heat conduction (Hofmeister, 2004; Hofmeister et al., 2006), of diffusivity of cations (e.g. Hier-Majumder et al. (2005)), and of electrical conductivity in mantle minerals (Karato, 1990). Electrical conductivity in hydrogen bearing NAMs is not only enhanced through higher mobility of cations, but also through the addition of mobile protons contributing to charge transport. The enhancing effect of hydrogen on electrical conductivity was observed in wadsleyite and ringwoodite (Dai and Karato, 2009b; Huang et al., 2005; Yoshino et al., 2008), in olivine (Wang et al., 2006; Yoshino et al., 2006, 2009), in diopside (Wang et al., 1999), in orthopyroxene (Dai and Karato, 2009a), and in bulk mantle peridotites (Wang et al., 2008). Thus, high electrical conductivities in the upper mantle were often interpreted in terms of hydrogen enhanced electrical conductivity in minerals (e.g., Karato (1990); Hirth et al. (2000)). In addition anisotropic electrical conductivity at the base of the lithosphere (Bahr and Duba, 2000; Leibecker et al., 2002; Gatzemeier and Moorkamp, 2005) was hypothesized to be caused by the anisotropic mobility of hydrogen in upper mantle minerals derived from laboratory electrical conductivity (e.g., Wang et al. (2006); Yoshino et al. (2006); Dai and Karato (2009a)) and hydrogen diffusion studies (e.g., Kohlstedt and Mackwell (1998); Stalder and Behrens (2006)).

However, neither enhanced electrical conductivities nor electrical anisotropy could consentaneously be attributed to proton conduction in hydrous mantle NAMs. Yoshino et al. (2006, 2009) found enhancement of electrical conductivity in olivine through hydrogen to be too low at upper mantle temperatures. Simpson and Tommasi (2005) tested the hypothesis of anisotropic proton conduction at the top of the asthenosphere and concluded that the electrical anisotropy cannot be attributed to proton conduction alone. On the other hand, Wang et al. (2006) and Dai and Karato (2009a) measured a large hydrogen-induced enhancement of electrical conductivity for olivine

1. Introduction

and orthopyroxene and interpreted the results as to explain highly conductive regions in the upper mantle. The reason for the high electrical conductivity of the transition zone is still controversial. Electrical conductivity of hydrous wadsleyite and ringwoodite was found to be higher than electrical conductivity of the transition zone by [Yoshino et al. \(2008\)](#) and [Manthilake et al. \(2009\)](#), whereas [Huang et al. \(2005\)](#) and [Dai and Karato \(2009b\)](#) inferred a transition zone water content of about 0.1-0.3 wt% H₂O beneath the Pacific from their experimental results. These water contents, however, are still only one tenth of the water storage capacity in wadsleyite and ringwoodite.

The presence of hydrogen in minerals provides a possible explanation for abnormal results from geophysical deep sounding, such as enhanced electrical conductivity, anisotropic electrical conductivity, and seismic wave attenuation. Provided the influence of hydrogen on electrical conductivity and rheology is well understood, water concentrations and the distribution of water in Earth's mantle could be inferred from seismic and magnetotelluric studies. However, laboratory studies, on which geophysical models could be based, are still either sparse and incomplete, or inconsistent. In order to derive reliable information about Earth's mantle from geophysical deep sounding, it is crucial to understand the influence of hydrogen on physical properties of mantle materials. In this study, hydrogen transport mechanisms and -kinetics in orthopyroxene were investigated by diffusion experiments and electrical conductivity measurements. The comparison between electrical conductivity and hydrogen diffusivity enabled the identification of the charge transport mechanisms and to constrain the contributions of different charge carriers to electrical conduction. Since orthopyroxene is an abundant mineral in Earth's upper mantle and contains about five times more water than olivine, it might have a substantial influence on physical properties of the upper mantle and needs to be considered in geophysical models based on laboratory data.

1.3. Incorporation of hydrogen in orthopyroxene and characteristics of FTIR-spectra

Infrared spectroscopy is a powerful tool to analyse and to quantify OH in minerals. The infrared spectrum of orthopyroxene shows often complex and unique OH-absorbance features caused by OH-stretching vibrations and being closely related to chemical composition. Since the position of an OH-absorption band depends on the length of the hydrogen bond (Novak, 1973), information about substitution reactions and proton locations in the crystal lattice can be deduced from FTIR-spectra. Criteria for the determination of the locations of protons and the associated point-defects are electrostatic considerations such as site electrostatic potentials (Smyth, 1989), charge-balance considerations, and spatial considerations taking into account the O-H...O bond lengths. Limited conclusions can be drawn from possible substitution reactions, from frequencies of OH-absorption bands, and from the comparison of OH-spectra of samples with different chemical compositions.

The OH-spectrum of **pure enstatite** consists mainly of one sharp band at 3362 cm^{-1} and two or three very broad and overlapping bands in the range $2800 - 3300\text{ cm}^{-1}$ (Fig. 1.2). The width and overlap of these peaks complicates the determination of the number and positions of peaks. In Si-deficient enstatite, two additional sharp OH-bands at 3592 and 3687 cm^{-1} are present. These are assigned to tetrahedral vacancies, the so called hydrogarnet defect, i.e., $V_{\text{tetr}} + 4\text{H}^+$, where V_{tetr} denotes a tetrahedral vacancy (Prechtel and Stalder, 2010). In the following, subscript "oct" denotes octahedral position and "tetr" tetrahedral position. In contrast to all other OH-bands in orthopyroxene, which are polarized parallel to the crystallographic c-axis (n_γ), these two bands are polarized parallel to the b-axis (n_α). Since all crystals in this study have been synthesised at silica oversaturated conditions, these two OH-bands were not observed. The main OH-bands exhibited by the samples of this study are very likely caused by hydrogen charge-balancing Mg-vacancies,

1. Introduction

i.e., $\text{Mg}^{2+} \Rightarrow \text{V}_{\text{oct}} + 2\text{H}^+$, where V_{oct} denotes a vacant octahedral position. The most likely position of protons in the crystal structure of pure enstatite is between the two O(3A) or between two O(3B) atoms, near the cavities between M2 octahedral positions (Stalder and Skogby (2002), Fig. 1.3).

Iron-bearing orthopyroxene shows two additional bands at 3330 and 3463 cm^{-1} . Both additional bands are associated with ferric iron through the substitution reaction: $2\text{Mg}^{2+} \Rightarrow \text{Fe}_{\text{oct}}^{3+} + \text{H}^+ + \text{V}_{\text{oct}}$ (Stalder, 2004). The ferric iron related OH-bands are small compared to OH-bands of pure enstatite at total iron content below about 3 wt% FeO total iron (Fig. 1.2). Hydrogen can also be incorporated by reducing preexisting trivalent iron: $[2\text{Fe}_{\text{oct}}^{3+} + \text{V}_{\text{oct}}] + \text{H}_2 \Rightarrow [2\text{H}^+ + \text{V}_{\text{oct}}] + 2\text{Fe}^{2+}$, where the point defect complexes are given in parentheses. The first hydrogen incorporation mechanism operates during crystal growth, whereas the second reaction denotes a solid-state hydration mechanism.

Additional bands at higher wavenumbers are exhibited by **aluminium-bearing orthopyroxene** and the main band of pure enstatite at 3362 cm^{-1} splits up into three peaks (3320, 3362, and 3385 cm^{-1}). The main Al-associated bands are located within $\pm 5 \text{ cm}^{-1}$ at 3477, 3520, 3550, 3583, 3602, and 3620 cm^{-1} . Intensity and overlap of the sharp bands in the higher range of wavenumbers (3450-3650 cm^{-1}) increase with Al-content of orthopyroxene. Due to the overlap, the number of clearly distinguishable peaks reduces with increasing Al-content. The deconvolution of high-Al orthopyroxene OH-spectra are deduced from low-Al orthopyroxene samples and possesses some uncertainty (two uppermost spectra in Fig. 1.2). If the Al-concentration is lower than about 1 wt%, the IR-spectrum still resembles the one of pure enstatite except for the additional bands at wavenumbers above 3450 cm^{-1} . It differs the more from it, the higher the Al-concentration. Most of the Al^{3+} is incorporated by the Tschermak's substitution (see also Section 3.1). Results from both X-ray single crystal diffraction (Smyth et al., 2007), and NMR-spectroscopy (Kohn et al., 2005) on Al-rich enstatite showed a nearly equal distribution of

1.3. H-incorporation and FTIR-spectra of orthopyroxene

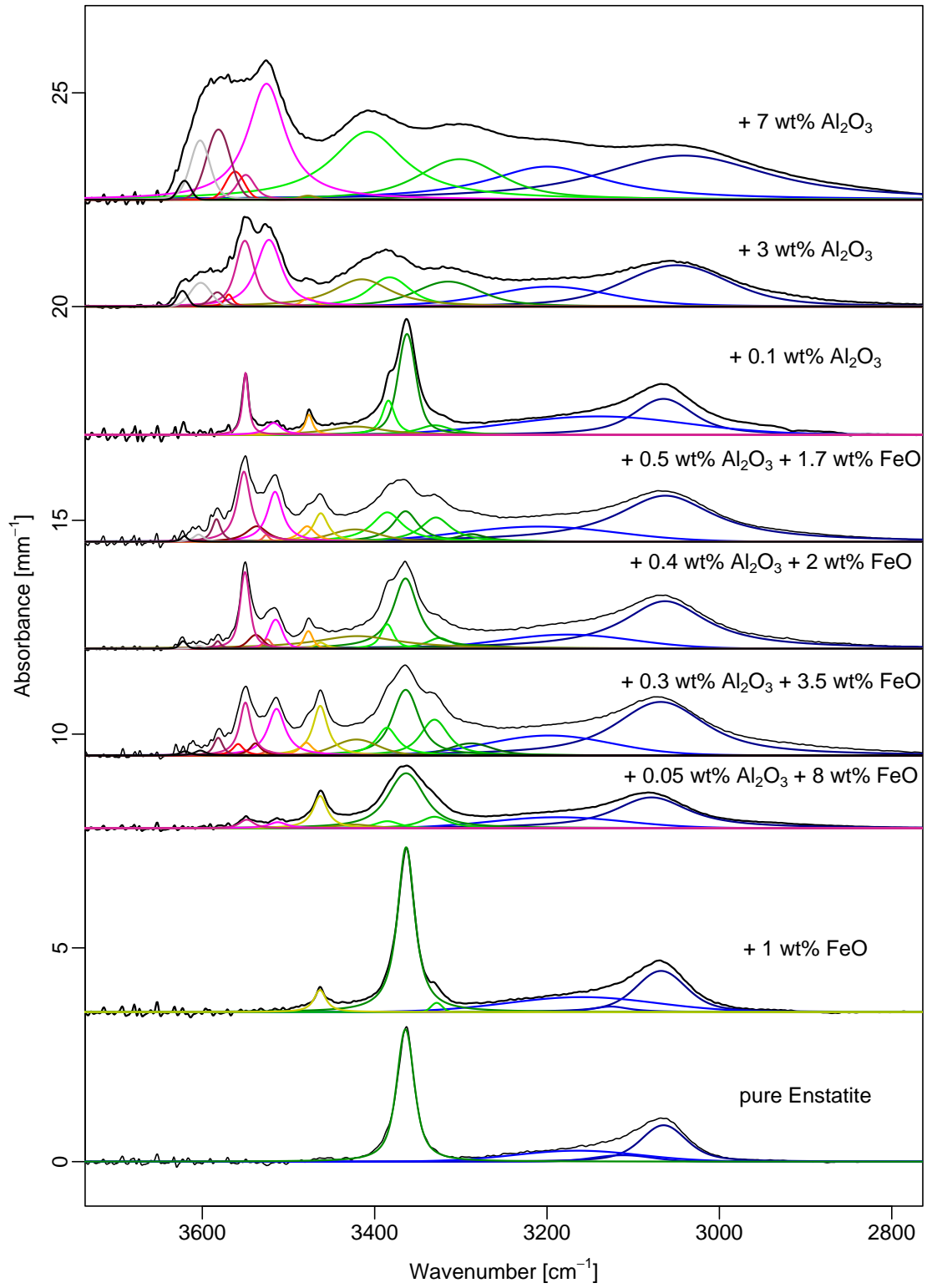


Figure 1.2.: OH-absorption spectra of several orthopyroxenes and their peak deconvolution; polarized IR-beam with $E \parallel [001]$

1. Introduction

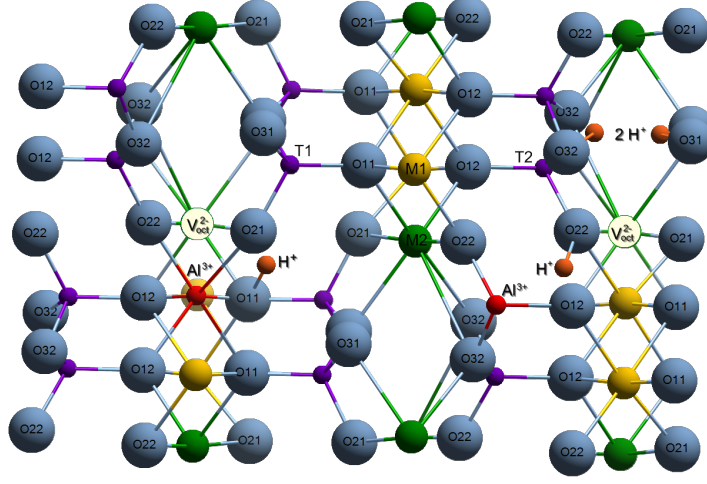
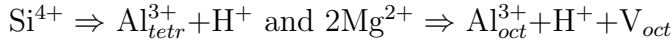


Figure 1.3.: Crystal structure of orthopyroxene cut $||[001]$ illustrating some protonated point-defects and possible proton locations. O-atoms are labelled, octahedral and tetrahedral positions are labelled exemplarily.

Al^{3+} on M1- and T2-sites, suggesting that the tetrahedral and the octahedral substitution mechanism involving H^+ :



are equally favourable. This interpretation agrees with the findings from IR-measurements, where, in contrast to the Cr^{3+} - or Fe^{3+} -doped crystals, two additional sets of OH-absorption bands occur upon doping with Al^{3+} . The most plausible band assignment is that the high wavenumber bands are caused by tetrahedral defects, as suggested for olivine (Matveev et al., 2001; Lemaire et al., 2004; Kovács et al., 2010), clinopyroxene (Stalder and Ludwig, 2007), and orthopyroxene (Prechtel and Stalder, 2010). The most likely positions of protons in Al-bearing enstatite were suggested to be between O(2A) - O(1A) and O(2B) - O(1B), near the M1 or M2 position, constrained from O-O distances and site electrostatic potential calculations (Stalder and Skogby (2002); Smyth et al. (2007), Fig. 1.3). These proton positions were assigned

1.3. H-incorporation and FTIR-spectra of orthopyroxene

to the bands around 3520 and 3550 cm^{-1} . The splitting of the main OH-band of pure enstatite at 3362 cm^{-1} in two additional "shoulders" at 3320 and 3385 cm^{-1} might result from distorted T2 tetrahedra due to Al^{3+} replacing Si^{4+} on tetrahedral positions, for example by the Tschermak's substitution reaction $\text{Mg}^{2+} + \text{Si}^{4+} \Rightarrow 2\text{Al}^{3+}$ (Stalder and Skogby, 2002). The concentration of protons bound to oxygen atoms of distorted tetrahedra increases with Al-concentration, explaining the increase of the flanks at the cost of the 3362 cm^{-1} -band with increasing Al-contents (Stalder and Skogby, 2002).

The infrared spectra of **aluminium plus iron bearing orthopyroxene** contain both the Al-bands and the Fe-bands, but additional small bands at 3524 and 3538 cm^{-1} near the most prominent Al-related bands 3550 cm^{-1} and 3520 cm^{-1} . Closely located centers of OH-absorption bands, related to distinct cations, could suggest a similar substitution reaction. Through incorporation of point-defect forming cations, the crystal lattice is distorted in the vicinity of the defect. If an analogous substitution reaction exists for distinct cations, their different ionic radii may cause different lattice distortions, resulting in slightly different in O-H...O bond lengths. For example, the bands at 3461 cm^{-1} and 3471 cm^{-1} , the former iron related and the latter aluminium related, could correspond to equivalent incorporation mechanisms (Stalder and Ludwig, 2007), such as $2\text{Mg}^{2+} \Rightarrow \text{Fe}_{oct}^{3+} + \text{H}^+ + \text{V}_{oct}$ and $2\text{Mg}^{2+} \Rightarrow \text{Al}_{oct}^{3+} + \text{H}^+ + \text{V}_{oct}$.

As long as doped solely, both aluminium and ferric iron incorporation enhance hydrogen solubility in orthopyroxene with respect to pure enstatite, because these trivalent cations provide additional substitution mechanisms involving hydrogen as charge balancing cation (Stalder, 2004). In contrast, if doped in combination with each other, different trivalent cations can promote the formation of anhydrous defects such as $\text{Al}_{tet}^{3+} + \text{Fe}_{oct}^{3+}$ (Stalder et al., 2005).

2. Synthesis and preparation

2.1. Synthesis of orthopyroxene

The syntheses were done by following the procedure described by [Stalder \(2002\)](#). A mixture of 70 wt-% SiO_2 powder and 30 wt-% MgO powder was used as the starting material for synthesising pure enstatite. In order to synthesise crystals with iron and aluminium, Fe_2O_3 and Al_2O_3 were added to the mixture (Appendix. [A.1](#)). About 80 mg of the solid oxide mixture, about 30 mg of H_2O or D_2O , and one or two seed crystals $< 100 \mu\text{m}$ in size were sealed in a platinum capsule of 6-7 mm length and 4 and 3.6 mm outer and inner diameter, respectively. The seed crystals seem to promote the growth of one to five larger individuals, but this was not investigated systematically.

The pressure assembly for the piston cylinder experiments (Fig. [2.1](#)) was made of an inner alumina sleeve hosting the sealed capsule. Heating was provided by a graphite tube surrounding the alumina sleeve with the capsule, through electrical resistance heating. Typical parameters at run conditions were 280 A and 6 V. Two outer tubes, one made of pyrex glass and the outermost one of talc, served as the pressure medium and reduced friction. An alumina filler piece was placed on top of the sleeve containing the capsule. The pressure assembly was inserted into a tungsten carbide die-plate. The remaining space in the pressure cavity was filled with a steel plug and a pyrophyllite ring. The assembly was pressurised by a piston from below via an oil-hydraulic system. The experimental pressure was deduced from the oil pressure of the hydraulic system, assuming a pressure reduction through friction of ten per cent. The temperature was measured with an S-type thermocouple near the

2. Synthesis and preparation

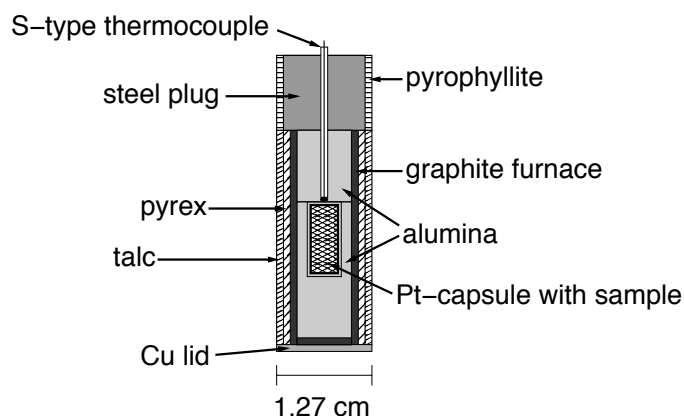


Figure 2.1.: Schematic picture (not to scale) of the pressure assembly.

capsule. The thermocouple was inserted through a borehole into the pressure assembly from the top.

The platinum capsule, containing the solid oxide mixture and some water, was simultaneously pressurised to 25 kbar and heated to 1400°C. The peak temperature was then held for one hour to melt and homogenise the mixture, before temperature was decreased isobarically with a rate of 10 or 6°C per hour down to 1150°C. During cooling, enstatite crystallised from the water rich melt. After reaching the end temperature, the sample was quenched by switching off the heating power. Crystal sizes ranged from some tens of micrometers to 3 mm with crystal habits varying from stubby prismatic to platy. Due to the high water content, the quench-phase was soft and presumably partly amorphous material, so the enstatite crystals could easily be separated from it.

2.2. Sample preparation

After synthesis, the capsule was opened and the largest crystals with little or no cracks and inclusions were hand picked and embedded in a thermoplastic resin. They were crystallographically oriented parallel to a crystallographical axis $\pm 5^\circ$ with a polarisation microscope with conoscopic illumination. The crystals were polished to plates of 120 to 350 μm in thickness. Most crystals

2.2. Sample preparation

were oriented $\parallel(010)$ because this orientation often provided the largest cross section. The least abundant orientation of the plates was $\parallel(001)$ because most crystals were elongated in this direction.

Because many of the synthesis runs with D_2O were not successful, some of the crystals synthesised with H_2O were deuterated in a cold seal-pressure vessel (CSPV) with H_2O as pressure medium at 2.5 kbar and $850^\circ C$ for about 7-10 hours. The crystals were sealed in a gold capsule with about 20 mg of D_2O and about 2 mg of SiO_2 to avoid reaction to olivine due to high SiO_2 solubility in the fluid phase at experimental conditions ([Anderson and Burnham, 1965](#)). In all samples, a small rest of hydrogen remained but it was regarded as negligible.

3. Chemical characterisation of samples

The major element composition was analysed with an electron microprobe (EMPA). Exemplarily, bulk ferric iron contents of some synthetic crystals were determined with Mößbauer spectroscopy to provide a basis for estimating ferric iron contents of the samples used for electrical conductivity experiments. The OH-contents were measured with FTIR-microspectroscopy either with a single element MCT-detector or with a focal plane array detector consisting of 64x64 MCT detectors.

3.1. Chemical composition — electron microprobe analysis

The chemical composition of the crystals used for diffusion and electrical conductivity experiments were determined after the experiments. The chemical compositions are given in the respective chapters describing the experimental results. Before the EMP-analyses, the crystals were embedded in epoxy resin, polished to a planar surface, and coated with carbon to avoid accumulation of charges at the surface during exposition to the electron beam. The crystals were analysed in terms of Si, Mg, Fe, Al, Ca, K, Ti, Mn, and Na.

Electron microprobe analyses were carried out in Göttingen with a JEOL JXA 8900 RL and in Hannover with a Cameca Camebax SX100. The focus diameter of the electron beam was 5 μm , with a beam current of 15 nA, and an acceleration voltage of 15 keV.

3. Chemical characterisation of samples

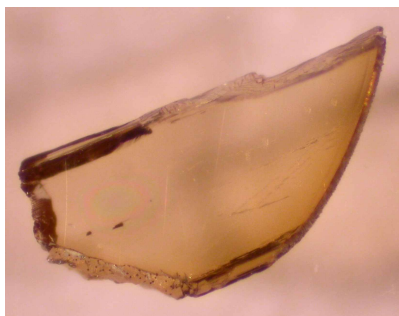


Figure 3.1.: Photomicrograph of sample es17-5. The chemical inhomogeneity is indicated by the colour gradient, the darker region is higher in iron and aluminium. The width of the picture is about 1.8 mm.

A slight chemical inhomogeneity was detected in aluminium and iron bearing orthopyroxenes, often also visible from a gradient in color (see polished sample in Figure 3.1). The samples did not show a radial zoning, but a gradient over the whole sample. However, the distribution of elemental concentrations over the respective whole samples could not be analysed in detail.

Figure 3.2 shows that the major elements Si, Mg, Fe, and Al, are linearly correlated in the same way as described by Stalder (2004). The cationic ratio of Al to Si and Al to Mg+Fe (total iron) is both 0.5, suggesting the Tschermak's substitution to be the most abundant mechanism of Al-incorporation in orthopyroxene ($\text{Mg}^{2+} + \text{Si}^{4+} \Rightarrow 2 \text{Al}^{3+}$). The increasing scatter towards lower Al-concentrations in both plots indicates increasing diversity of Al-related point defects, e.g., coupled Tschermak's substitution of ferric iron and aluminium ($\text{Mg}^{2+} + \text{Si}^{4+} \Rightarrow \text{Al}^{3+} + \text{Fe}^{3+}$). The equal distribution of Al between tetrahedral and octahedral positions is confirmed by an X-ray diffraction measurement on aluminous enstatite (Volker Kahlenberg, University Innsbruck, personal communication) and mineral formulas derived from the EMPA data (Appendix A.2). From the approximate Mg/Fe-ratio of 1:1 it can be concluded that most iron is incorporated "regularly" on octahedral positions. The mantle orthopyroxenes from San Luis Potosi, Mexico, do not fit into the trend given

3.1. Chemical composition — electron microprobe analysis

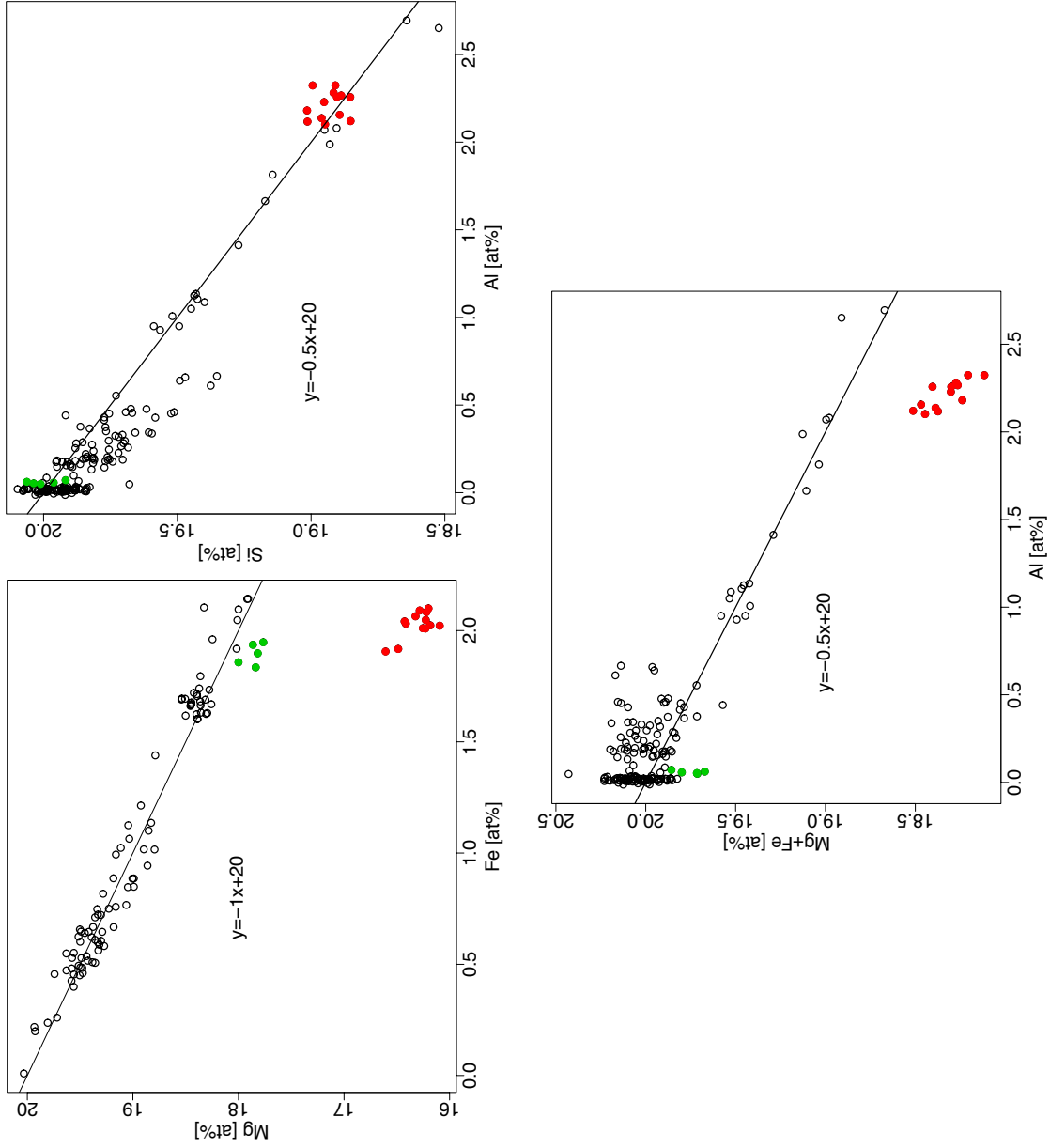


Figure 3.2.: Linear correlations between the major elements in synthetic orthopyroxenes (black), three natural mantle orthopyroxenes from San Luis Potosi, Mexico (red), and one natural orthopyroxene from Tanzania (green).

3. Chemical characterisation of samples

by the synthetic orthopyroxenes and the natural Tanzanian orthopyroxene, because they contain substantial amounts of calcium (0.4 at%) and chromium (0.1 at% [Heinrich and Besch \(1992\)](#)). Both elements were not analysed and not considered in the elemental correlations. Those two elements are incorporated on octahedral positions in orthopyroxene, probably leading to the shift with respect to the synthetic samples.

3.2. Fe(II)- and Fe(III)-content — Mößbauer spectroscopy

The Mößbauer spectroscopic measurements were carried out at room temperature with a ^{57}Co point-source operated in constant acceleration mode. The samples were doubly polished single crystal plates, fixed in an aperture in a 1 mm thick Pb-foil before placing them in front of the point source. After calibrating the results to $\alpha\text{-Fe}$, the spectra were fitted with the software "MDA" ([Jernberg and Sundqvist, 1983](#)), applying three or four doublets of Lorentzian peakshape. The doublets correspond to Fe(II) on octahedral M1 position, Fe(II) on octahedral M2 position, Fe(III) on any octahedral position, and Fe(III) on any tetrahedral position. The Fe(II)- and Fe(III)-contents were determined as percentage of total iron content (Table [3.1](#)). Because the samples would have been too small to produce a proper absorption signal ([Stalder, 2004](#)), the samples were enriched in ^{57}Fe in the syntheses through the addition of this isotope to the synthesis start mixture.

As indicated in Table [3.1](#), two samples were measured with Mößbauer spectroscopy before and after heating in H_2 or in air, respectively. After some minutes of heat treatment, a change in ferric iron content was already observable. All other samples in the table have been heated for several hours in air prior to the Mößbauer spectroscopic measurements. Samples es2-2 and es5-1 were used for electrical conductivity measurements (which were not successful), and the remaining samples in the table, es5-4 to es9-6, were used for

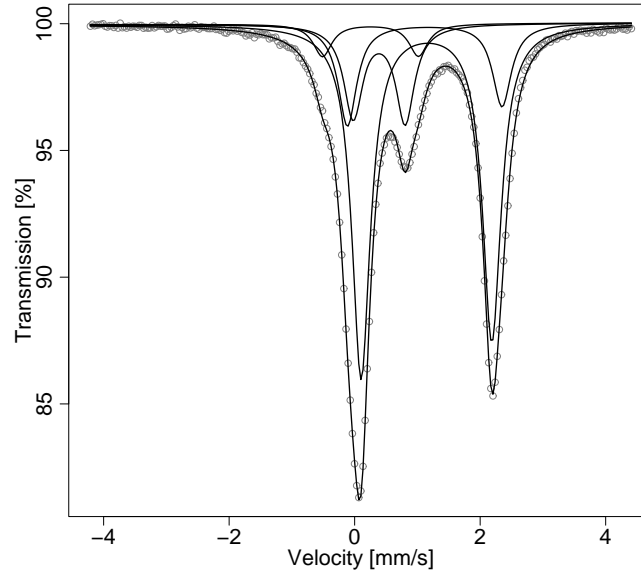


Figure 3.3.: Example of a Mößbauer spectrum fitted with four doublets. This fit corresponds to the values of samples es9-5 in Table 3.1.

dehydration experiments in air.

3.3. H_2O -content — FTIR-spectroscopy

Fourier transform infrared spectroscopy (FTIR-spectroscopy) was used to measure OH-concentrations in the samples. The measurements were done either with a Bruker IFS88 (Institute for Mineralogy, University of Hannover) or with a Perkin Elmer 2000 (Geozentrum, University of Göttingen) both equipped with an IR-microscope. The doubly polished crystal plates were placed in the confocal, polarised IR-beam either on a Suprasil- (Hannover) or a KBr-window (Göttingen). Single point analyses were done with a rectangular aperture of $50 \times 50 \mu\text{m}$ (Hannover) or with a round pinhole aperture of $100 \mu\text{m}$ in diameter (Göttingen). Profiles were measured with a slit aperture of $30 \mu\text{m}$ width and a micrometer-measurement-device for positioning. Two-dimensional spatial distribution of OH-absorbance over the crystal plate was measured with a Bruker Vertex 70 equipped with a focal plane array detector and a Hyperion

3. Chemical characterisation of samples

Table 3.1.: Results of Mößbauer spectroscopic measurements in percent of total iron.

	Fe(II)	M2	Fe(II)	M1	Fe(III)	oct	Fe(III)	tet	% Fe(III)	comment
es5-1a	79.98		17.31		2.70		0.00		2.70	untreated
	80.06		14.77		5.16		0.00		5.16	after 0:15 h in air 850°C
	78.08		18.2		3.73		0.00		3.73	after 1:23 h in H ₂ @ 900°C
es9-7	63.55		25.46		10.99		0.00		10.99	untreated
	64.55		26.67		5.37		3.41		8.78	after 1:45 h in H ₂ @ 905°C
es2-2	76.73		23.27		0.00		0.00		0.00	Electrical conductivity
es5-1	71.52		13.23		12.69		2.56		15.25	
es5-4	71.5		23.43		5.08		0.00		5.08	
es5-6	69.77		20.02		8.17		2.04		10.21	
es5-7	74.48		16.02		7.84		1.66		9.5	Dehydration
es9-5	60.53		16.70		17.08		5.69		22.77	
es9-6	55.05		20.63		20.19		4.14		24.33	

3.3. H_2O -content — FTIR-spectroscopy

3000 microscope in the Institute of Mineralogy and Petrography, University of Innsbruck, enabling a spatial resolution of down to 3 μm .

A linear or quasilinear baseline correction was applied to the region of OH-absorbance in the infrared spectra. The OH-absorbance was either determined by a peak-deconvolution using the software Peakfit (Jandel Scientific) or the absorbance was integrated over the respective wavenumber range 2800-3650 cm^{-1} . For quantitative analyses of the IR-spectra, the calibration by [Libowitzky and Rossmann \(1997\)](#) was used. A detailed description of infrared spectra evaluation is given in Section 5.3.

Part I.

**Hydrogen Diffusion in
Orthopyroxene**

4. Introduction

The diffusivity of hydrogen has important consequences for the reequilibration of mantle xenoliths during their ascent and on electrical conductivity of NAMs in the mantle. Hydrogen contents of mantle xenoliths do not necessarily reflect hydrogen contents in the source region, because mm-sized crystals could reequilibrate their hydrogen contents with the host magma during days. This has been shown by hydrogen diffusion studies of nominally anhydrous minerals (e.g., [Kohlstedt and Mackwell \(1998\)](#); [Demouchy et al. \(2006\)](#); [Ingrin et al. \(1995\)](#); [Hercule and Ingrin \(1999\)](#); [Stalder and Skogby \(2003\)](#); [Stalder and Behrens \(2006\)](#)). The contribution of protons to electrical conduction in orthopyroxene depends on their mobility. This study aims to further constrain hydrogen mobility in orthopyroxene, an abundant mineral of the upper mantle. Kinetics of dehydration and of H/D-exchange in iron and aluminium bearing orthopyroxenes as well as in pure enstatite were investigated. Hydrogen self-diffusivity is reflected by hydrogen deuterium exchange and the mobility of hydrogen associated point defects was investigated by dehydration experiments.

5. Diffusion experiments

Diffusion is a thermally activated process and is described by Fick's second law of diffusion

$$D = D_0 \times \exp(-E_a/RT) \quad (5.1)$$

with D being the diffusion coefficient, D_0 the preexponential factor, E_a the activation energy, which is the amount of energy required for a particle to pass the potential barrier between its equilibrium position and an adjacent one. R is the ideal gas constant, and T the absolute temperature. The parameters E_a and D_0 are deduced from the Arrhenius plot $\log(D)$ vs. $1/T$, in which the diffusion coefficients plot in a straight line due to

$$\log(D) = \log(D_0) - E_a/R \times \ln(10) \times 1/T \quad (5.2)$$

Hence, the activation energy is calculated from the slope:

$$E_a = \text{Slope} \times R \times \ln(10) \quad (5.3)$$

The preexponential factor equals the intercept of the line.

Two types of diffusion experiments were conducted: dehydration in air at ambient pressure, and H/D-exchange experiments at 2 kbar in argon-pressurized cold-seal pressure vessels (CSPV). The H/D-exchange experiments were conducted at the Institute of Mineralogy, University of Hannover, and the dehydration experiments were conducted at the Department of Geosciences, University of Göttingen. Most diffusion experiments were of the time-series type, i.e., after each of several short annealing experiments (ten minutes to four hours duration), OH- and OD-concentrations were measured with FTIR-spectroscopy,

5. Diffusion experiments

and the diffusion coefficient was deduced from the evolution of OH- and OD-concentrations with time. Additionally, some diffusion coefficients were deduced from profiles of OH- and OD-absorbance across samples. Pure enstatite and orthopyroxenes with variable contents of aluminium and iron were used, which have been synthesised in a piston-cylinder apparatus with excess silica at water saturated conditions as described in Section 2.1. Before the experiments, all crystals were polished to small plates oriented along the crystallographic axes to observe anisotropic diffusivity and to properly determine H₂O-concentrations in the crystals by FTIR-spectroscopy.

The heating time before reaching the final temperature of each annealing experiment was taken into account by computing a correction term for each experiment according to the following equation (Ingrin et al., 1995):

$$t_{corr} = \int_{t=0}^{t_{end}} \exp \left(\frac{-E_a}{R} \left(\frac{1}{T(t)} - \frac{1}{T_{end}} \right) \right) dt \quad (5.4)$$

with t_{corr} being the time to be added to the dwell time at the final temperature, t_{end} the point in time at which the final temperature was reached, E_a the activation energy in [J/mol], R the ideal gas constant in [J/molK], $T(t)$ the temperature at time t in [K], and T_{end} the final temperature. In practice the sum of the discrete steps of the time temperature record was computed:

$$t_{corr} = \sum_i \exp \left(\frac{-E_a}{R} \left(\frac{1}{T_i} - \frac{1}{T_{end}} \right) \right) \cdot \Delta t \quad (5.5)$$

with $\Delta t = t_i - t_{i-1}$ and $T_i = T(t_i)$. The activation energy was first estimated from Stalder and Behrens (2006) and adapted subsequently from the actual activation energy of diffusion obtained from this first estimate. Typically, the change in the diffusion coefficient was smaller than its error after only one iteration. The dwell times and corrected times are summarized in Table 5.2 and 5.1.

Diffusion coefficients were calculated from the time series of OH-extraction using the solution of Fick's second law for one dimensional-diffusion with homogeneous initial concentration in a solid bound by two parallel planes (Ingrin

et al., 1995; Carslaw and Jaeger, 1959)

$$\frac{C_{av}}{C_0} = \frac{8}{\pi^2} \sum_{n=0}^{\infty} \frac{1}{(2n+1)^2} \exp\left(-\frac{Dt(2n+1)^2\pi^2}{L^2}\right) \quad (5.6)$$

with C_{av} being the average OH-absorbance (or concentration in ppm-wt) measured through the bulk crystal plate, C_0 the initial concentration, D the diffusion coefficient in [m²/sec], and L the thickness of the crystal in [m]. For the increasing OD-concentration applies analogously

$$\frac{C_{av}}{C_0} = 1 - \left(\frac{8}{\pi^2} \sum_{n=0}^{\infty} \frac{1}{(2n+1)^2} \exp\left(-\frac{Dt(2n+1)^2\pi^2}{L^2}\right) \right) \quad (5.7)$$

Two assumptions were made for applying these two equations: (1) the diffusion coefficient is independent of concentration, and (2) the diffusion from the edges of the crystal plate does not influence the diffusion through the plate. The first assumption is approximately justified for the relatively small hydrogen concentrations in the samples of this study. To ensure that the second assumption is justified, care has been taken to keep the distance between the analysed spot and the edges or cracks of the sample much larger than the thickness of the sample.

From the concentration profile across the crystal a diffusion coefficient was computed using the following equation (Crank, 1975; Stalder and Behrens, 2006)

$$\frac{C(x) - C_0}{C_1 - C_0} = \operatorname{erfc}\left(\frac{x}{2\sqrt{Dt}}\right) + \operatorname{erfc}\left(\frac{X-x}{2\sqrt{Dt}}\right) \quad (5.8)$$

with $C(x)$ being the absorbance (or concentration) at the location x , C_0 the initial absorbance (concentration), C_1 the minimum absorbance, X the total length of the profile in [m]. The function $\operatorname{erfc}()$ is the complement of the error-function, i.e., $1-\operatorname{erf}()$. The profile-position x was measured with a Mitutoyo micrometer mounted on the x-y-table of the IR-microscope. The ideal value of C_1 is zero, but the fit of Equation 5.8 yielded usually $C_1 > 0$. In an H-extraction profile, the surface concentration can not directly be measured with FTIR-spectroscopy because the spatial resolution of the FTIR-spectrometer used

5. Diffusion experiments

here was about 30 μm . In addition, due to the finite thickness and irregularly shaped edges of the samples, reflection and scatter complicated measurements at the edges. One reason for $C_1 > 0$ certainly was, that initially OD-bearing samples also contained a small amount of OH due to contamination during capsule preparation and experimental conditions.

The error of the diffusion coefficient was computed with the Gaussian law of error propagation:

$$\Delta D = \sqrt{\left(\frac{E_a}{RT} \cdot \frac{\Delta T}{T}\right)^2 + \left(\frac{\Delta t}{t}\right)^2 + \left(\frac{2\Delta x}{x}\right)^2 + \left(\frac{\sigma_D}{D}\right)^2 + \left(\frac{\Delta A}{A}\right)^2} \cdot D \quad (5.9)$$

ΔD is the absolute error of the diffusion coefficient D , E_a the activation energy, R the ideal gas constant, T the temperature in Kelvin. The error of temperature was estimated individually for each experiment from temperature oscillations during the dwell time. The error of time Δt was estimated to be $1/2 \times t_{\text{corr}}$, the correction term resulting from Equation 5.5. Δx was either the uncertainty of measurement of sample thickness for time series, i.e., 5 μm , or for profiles, an uncertainty of 20 μm was assumed. For the diffusion profiles measured with a much more accurate automatic x-y-table, Δx was estimated to be 10 μm . σ_D is the standard deviation of D resulting from the fit of Equation 5.7 or 5.8 to the data. The error of absorbance ΔA was assumed to be 10%, resulting from the uncertainty of baseline correction. Errors were usually about 0.1-0.2 log units for diffusion coefficients derived from time series, and about 0.2-0.6 log units for diffusion coefficients derived from concentration profiles. Errors larger than 0.2 log-units originated mainly from the error of time, because some samples were heated relatively slowly. Errors between 0.1 and 0.2 log-units resulted almost exclusively from the standard deviation of the diffusion coefficient. All other errors, i.e., uncertainties of time, temperature, sample thickness, and IR-absorbance, had virtually no influence, particularly on the logarithmic scale. Nevertheless, for consistency reasons all errors were calculated with Equation 5.9.

5.1. Dehydration experiments

Several samples were placed together in an open gold crucible and heated in a vertical tube furnace at ambient pressure in air. The samples were heated several times and during heat treatment, hydrogen was released from the samples. After each dehydration step (the term "dehydration" is used synonymously with "dehydrogenation" and means hydrogen extraction), OH-absorbance was measured with FTIR-spectroscopy and polarized light. The samples were placed on a KBr-crystal and the focus diameter was reduced to 100 μm with a pinhole aperture. The polarisation direction of the IR-beam was aligned parallel to the two crystallographic axes lying in the plane of the sample plate, and the OH-absorbances of both measurements were added. From the decrease of absorbance as a function of time, a dehydration diffusion coefficient could be deduced for the temperatures 800°C, 850°C, 900°C, and 950°C. The temperature was monitored with a S-type thermocouple a few millimeters away from the crucible. The sample holder was inserted into the hot zone of the furnace after the final temperature in the furnace had stabilized. A temperature of 770°C was reached within a few seconds after the sample holder was pushed into the furnace and the time-temperature path was recorded from 770°C until the final temperature in 10°C steps or less. The heating time was used for the time correction and for calculating the error of the diffusion coefficient.

5.2. H/D-exchange experiments

Oriented crystal sections originally synthesised in H_2O , thus containing OH, were heated together with D_2O in sealed gold capsules at 2 kbar in argon-pressurised CSPV's. During the experiments, hydrogen was replaced by deuterium in the crystals. The experiments were conducted as a time-series and subsequent measurements of OH- and OD-absorbance of the bulk crystal plate with FTIR-spectroscopy after each experiment of the time-series. A diffusion coefficient was deduced from OH- and OD-absorbance versus time for the

Table 5.1.: Time increments of dehydration experiments in minutes, corrected according to equation 5.5. Dwell times at the target temperatures are given in parentheses. The corrected times are higher than the dwell times because the heating and cooling time was taken into account in the time correction calculation (Eq. 5.5).

Sample	T [°C]	Time increments [minutes]								
		1	2	3	4	5	6	7	8	9
es9-1	800	24 (10)	48 (34)	38 (29)	39 (30)		129 (120)	129 (120)	144 (136)	
es5-3		24 (10)	48 (34)	38 (29)	39 (30)	69 (60)	129 (120)	129 (120)	144 (136)	
es7-2		23 (10)	47 (34)	37 (29)	38 (30)	68 (60)	128 (120)	128 (120)	143 (136)	
es9-1	850	38 (32)	37 (30)	37 (31)	49 (40)	51 (40)	65 (60)	128 (122)	250 (242)	367 (361)
es9-2		38 (32)	37 (30)	37 (31)	49 (40)	51 (40)	65 (60)	128 (122)	250 (242)	367 (361)
es5-3		38 (32)	37 (30)	37 (31)	49 (40)	51 (40)	65 (60)	128 (122)	250 (242)	367 (361)
es5-4			37 (30)	37 (31)	49 (40)	51 (40)	65 (60)	128 (122)	250 (242)	367 (361)
es7-2		38 (32)	36 (30)	36 (31)	47 (40)	50 (40)	64 (60)	127 (122)	249 (242)	367 (361)
es9-5	900	37 (30)	66 (60)	128 (123)	255 (249)	366 (360)				
es5-6		37 (30)	66 (60)	128 (123)	255 (249)	366 (360)				
es7-2		37 (30)	66 (60)	128 (123)	255 (249)	366 (360)				
es7-5		37 (30)	66 (60)	128 (123)	255 (249)	366 (360)				
es9-6	950	38 (30)	68 (61)	133 (123)	185 (180)	207 (201)	192 (187)			
es5-7		38 (30)	68 (61)	133 (123)	185 (180)	207 (201)	192 (187)			
es7-2		38 (30)	68 (61)	133 (123)	185 (180)	207 (201)	191 (187)			
es7-3		38 (30)	68 (61)	133 (123)	185 (180)	207 (201)	191 (187)			
es17-1a	990	71 (61)								
es17-2	829	190 (162)								

5.2. H/D-exchange experiments

temperatures 650, 700, 750, and 820°C. H/D-exchange experiments were also conducted at ambient pressure with deuterium-bearing crystals exposed to a continuous flow of hydrogen gas. During these experiments, electrical conductivity of the samples was measured. After the experiments at ambient pressure, the samples were cut perpendicular to the original faces and polished, in order to measure a concentration profile of OH and OD with FTIR-spectroscopy. The advantage of H/D-experiments at 2 kbar was the reduced dehydration due to higher D₂O-fugacity. But since dehydration is about one order of magnitude slower than H/D-exchange, significant dehydration did not occur in the H/D-exchange experiments at ambient pressure either.

In order to prevent alteration of orthopyroxene to olivine during the experiments at 2 kbar in D₂O, about 2-3 mg of SiO₂-powder were added before the capsule was welded shut, to saturate the fluid phase in SiO₂ at experimental conditions ([Anderson and Burnham, 1965](#)). Two crystals were sealed in one capsule, separated by a kink in the capsule wall and hold in place by slightly flattening the capsule. This was necessary to avoid cracking of the samples, when the capsule was squeezed later under experimental pressure. Nevertheless, some crystals broke at initial cracks during the experiments. However, no crystal had to be discarded due to cracking, because the cracks were visible before, and the location of the spot analysed with FTIR-spectroscopy did not have to be changed after the crystals were broken in two pieces. To check the capsules for leakage, they were placed in an oven at 110°C for several hours and weighed before and afterwards.

In most cases, two capsules were loaded into one autoclave. To keep the capsules in position and reduce the volume inside the autoclave, filler rods of Ni+NiO were added. To reduce loss of deuterium from the capsule, for experimental durations longer than one hour, about 200 μ L of D₂O were filled directly into the autoclave. Before starting the experiment, the furnace was stabilized at the final temperature. The sealed autoclave was pre-pressurized with argon gas to 500 bar and then pushed into the furnace. During heating of

5. Diffusion experiments

the autoclave, the pressure increased until 2 kbar and was automatically held constant at this value ± 50 bar during the entire duration of the experiment. The temperature was measured with a K-type thermocouple and continuously recorded every 10 to 30 seconds. The temperature was measured about 1 cm apart from the capsules outside of the autoclave, and corrected according to a temperature calibration, conducted before the first run. To keep the heating time as short as possible, the furnace was stabilized at a temperature 50°C above the target temperature of the experiment. After the autoclave had been inserted into the furnace, the temperature was reduced with the controller in steps of 10°C , synchronously to the heating of the autoclave, so furnace and autoclave would ideally reach the target temperature at the same time. Nevertheless, a short overshoot of the autoclave temperature could not be avoided in most cases, but was taken into account in the time correction. At the end of the experiment, the samples were quenched by taking the autoclave out of the furnace and immediately cooling it with compressed air. Temperature decreased below 300°C within about two minutes. Instead of defining a beginning and an end of the temperature plateau, the effective experimental time Equation 5.5 was applied to the whole time-temperature record, thereby also taking into account small deviations from the target temperature during the dwell at the final temperature, or temperature drifts.

For experiments at the two higher temperatures, 750 and 820°C , experimental durations of 10 to 60 minutes were conducted with a tiltable autoclave. While the CSPV's used in this study all operated in a horizontal position, the tiltable autoclave could be tilted temporarily to a vertical position to slide the capsules from the cool end to the hot end and backwards, allowing the samples to heat and cool within about 90 seconds. The capsules were attached to a steel weight and loaded in the autoclave. After the autoclave was connected to the pressure line, it was tilted 90° backwards to the vertical, to ensure the sample's position is in the rear of the autoclave which remains cool during the experiment. Then, the autoclave was pre-pressurized to 500 bar and inserted

5.2. *H/D-exchange experiments*

into the furnace, which had already established the final temperature. As soon as the autoclave reached a stable temperature and pressure (2 kbar), it was tilted together with the furnace 90° ahead, so the weight with the attached capsules slid to the hot front end of the autoclave. To end the experiment, the autoclave was taken out of the furnace and - before cooling with compressed air - was tilted again backwards, so the capsules slid back into the cool part. In these experiments, heating and cooling processes could not be recorded, because the autoclave was already equilibrated at the final temperature before the experiment was started. It was assumed that heating and cooling time were negligibly short, and time correction was done on the recorded temperature between the two tilting-times of the autoclave, i.e., between capsule in and capsule out.

After the experiments, the flattened capsules were weighed, heated over a flame for expansion, cut open, and dried. The crystals could easily be regained from the inflated and dry capsules. In some cases, an overgrowth of small quartz crystals had to be removed by very slight polishing before IR-measurement. Although bulk OH- and OD-absorbances could be influenced by removing a surface layer from the diffusion profile, no such correlation between polishing and irregularities in the time series could be observed.

For the IR-measurements, the crystals were placed on an infrasil plate under the IR-microscope and a continuous flow of H₂O- and CO₂-reduced air was blown onto the samples. A quadratic aperture of 50x50 μm was used corresponding approximately to the size of the focus. Although no polariser was placed into the beamline, the IR-beam was not isotropic, but comprised a direction of maximum energy, which was aligned parallel to the two crystallographic axes in the plane of the sample plate. The OH-absorbances of both measurements were added.

Table 5.2.: Time increments of H/D-exchange experiments in minutes, corrected according to equation 5.5. Dwell times at the target temperatures are given in parentheses. The corrected times are usually higher than the dwell times because the heating and cooling time was taken into account in the time correction calculation (Eq. 5.5). For exemptions see the footnotes.

Sample	T [°C]	Time increments [minutes]							Comment
es23-2	650	1	2	3	4	5	6	7	
es3-4		96 (90) 95 (90)	155 (150) 154 (150)	258 (240)					
es4-8	700	32 (30)	66 (60)	68 (60)	73 (60)	142 (120)			
es29-2		36 (30)	74 (60)	79 (60)	81 (60)	125 (120)	213 (210)	261 (240)	
es29-3		36 (30)	74 (60)	79 (60)	81 (60)	213 (210)	261 (240)		
es15-2		32 (30)	67 (60)	68 (60)	73 (60)	125 (120)			
es4-9	750	15 (10)	21 (21)	39 (30)	268 (60) ^a				tilting autoclave
es24-3		15 (10)	21 (21)	39 (30)	268 (60) ^a				tilting autoclave
es4-7	810	6 (10) ^b	23 (20)						tilting autoclave
es29-1b		9 (10) ^b	13 (20) ^b	30 (30)	30 (30)	31 (26)			tilting autoclave
es5-5		10 (10)	15 (20) ^b	31 (30)	31 (30)				tilting autoclave
es27-1	768	122							1 atm, profile
pen1	797	77							1 atm, profile
es11-1	853	64							1 atm, profile
es11-2a	800	125							1 atm, profile
es16-3b	843	45							1 atm, profile

^aThe large discrepancy between the set time and the corrected time resulted from a 50° C too high experimental temperature.

^bThe corrected time is lower than the dwell time due to too low experimental temperatures.

5.3. Evaluation of IR-spectra of annealed samples

The subsequent IR-measurement of some samples revealed, that the baseline of IR-spectra can change significantly with repeated thermal treatment and handling of the crystals. This made the accuracy of OH- and OD-concentrations, deduced from the spectra, questionable, and complicated the interpretation of the time series. Therefore, IR-spectra were evaluated with particular attention for all possible sources of error and their influence on the spectra.

Although OH- and OD-absorbance was expected to change continuously in H/D-exchange experiments, a scatter in the time series (absorbance vs. time) was observed. Similarly, although a continuous decrease in OH-absorbance was expected in the dehydration experiments — in addition to scatter — in several samples an increase in absorbance was observed before it started to decrease (e.g., Appendix B.1, B.17). This phenomenon also occurred with some Al-bearing samples used for H/D-exchange experiments, but the increase was less pronounced.

Irregular variations of OH-absorbance were likely caused by scatter and reflection of the IR-beam at the two surfaces of the crystal plates due to their finite thickness. Sometimes, this produced an irregular sinusoidal baseline which was difficult to define. The OH-absorption spectrum of Al-bearing enstatite consists of many overlapping peaks and therefore does not reach zero in between the region of OH-absorption. In those cases, the amplitude of the sinusoidal background could only be estimated as illustrated in Figure 5.1.

A second source of analytical error in repeated measurements was the location of the focus of the IR-beam. A slight variation in the location of the focus could give a contribution to the observed scatter in the time series. This was especially true for crystals possessing cracks because concentration profiles were more evolved in the vicinity of cracks.

The increase in absorbance, which occurred in some diffusion experiments, cannot be explained by any experimental or analytical error. A possible rea-

5. Diffusion experiments

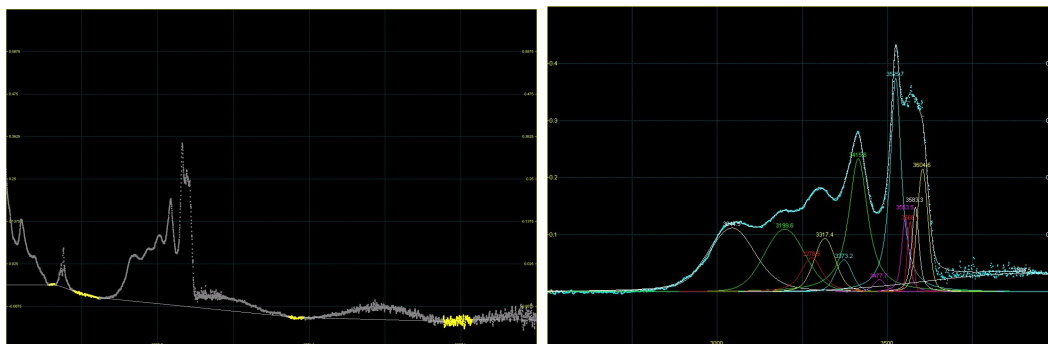


Figure 5.1.: Screenshots from Peakfit: baseline correction (left) and peak deconvolution (right) of a spectrum with sinusoidal baseline. The irregular oscillations are ignored in the baseline correction but the respective oscillation is included as an additional "peak" in the peakfitting model.

son is a change of the absorption coefficient due to an intrinsic process of equilibration to lower pressure and temperature, such as oxidation or lattice relaxation.

A common feature in some IR-spectra was an absorption band around 2350 cm^{-1} , resulting from atmospheric CO_2 . The CO_2 -band complicated the evaluation of OD-absorption spectra as the band is relatively broad and its intensity changed due to CO_2 -variations in the laboratory. At some point, this disturbance was eliminated by a stream of H_2O - and CO_2 -reduced air directed onto the sample and into the detector chamber.

In both cases — irregular and systematic variations — acceptable time series could be obtained by manual baseline correction and an internally consistent peak deconvolution. The best reproducibility was achieved by applying a linear baseline in the range of OH- and OD-absorption respectively. A large part of the unexpected variations in absorbance could be attributed to two broad peaks centered around 3200 cm^{-1} and 3420 cm^{-1} . These peaks were affected by the abovementioned presumably intrinsic processes, and were therefore neglected when appropriate (upper Figure 5.2). It was assumed that the actual

5.3. Evaluation of IR-spectra of annealed samples

OH-concentration and the diffusion process were not influenced by the intrinsic processes.

A third peak around 3060 cm^{-1} was influenced by CH-absorption around 2800 cm^{-1} resulting from contaminations on the surface. The CH-absorption feature could be identified by two sharp bands centered around 2850 and 2920 cm^{-1} . The band at 3060 cm^{-1} was also neglected when appropriate. Since not all peaks decreased equally on dehydration, the neglect of peaks poses an uncertainty for the diffusion coefficient deduced from the time series. The neglect of the large peaks around 3200 cm^{-1} and 3420 cm^{-1} led to a significant underestimation of the diffusion coefficient in some dehydration experiments with iron-bearing samples. An example for this is the time series of dehydration of sample es5-7, as illustrated in the lower Figure 5.2. The time evolution of individual peaks of es5-7 and a more detailed description of the assumptions made can be found in Appendix B.1.

H₂O-concentrations were calculated with the calibration of Libowitzky and Rossmann (1997) from IR-spectra with linear polarized beam and the electrical field vector oriented parallel to n_γ and either n_β or n_α . Because most samples were crystals polished to small plates, measurement of OH-absorbance of all three components — n_γ , n_β , and n_α — was only possible in a few cases, leading to an underestimation of H₂O-concentration. When the actual concentration was needed, for instance in the Nernst-Einstein equation, the actual H₂O-concentrations was estimated based on IR-measurements of chemically similar, untreated samples.

The OH- and OD-absorbance resulting from H/D-exchange experiments were measured without a polariser. Nevertheless, the IR-beam was not isotropic, but the intensity distribution was elliptic. Therefore, spectra were measured parallel to the two available crystallographic axes. Although H₂O-concentrations could not be computed from these measurements with the calibration of Libowitzky and Rossmann (1997), relative changes in absorbance were sufficient to deduce diffusion coefficients.

5. Diffusion experiments

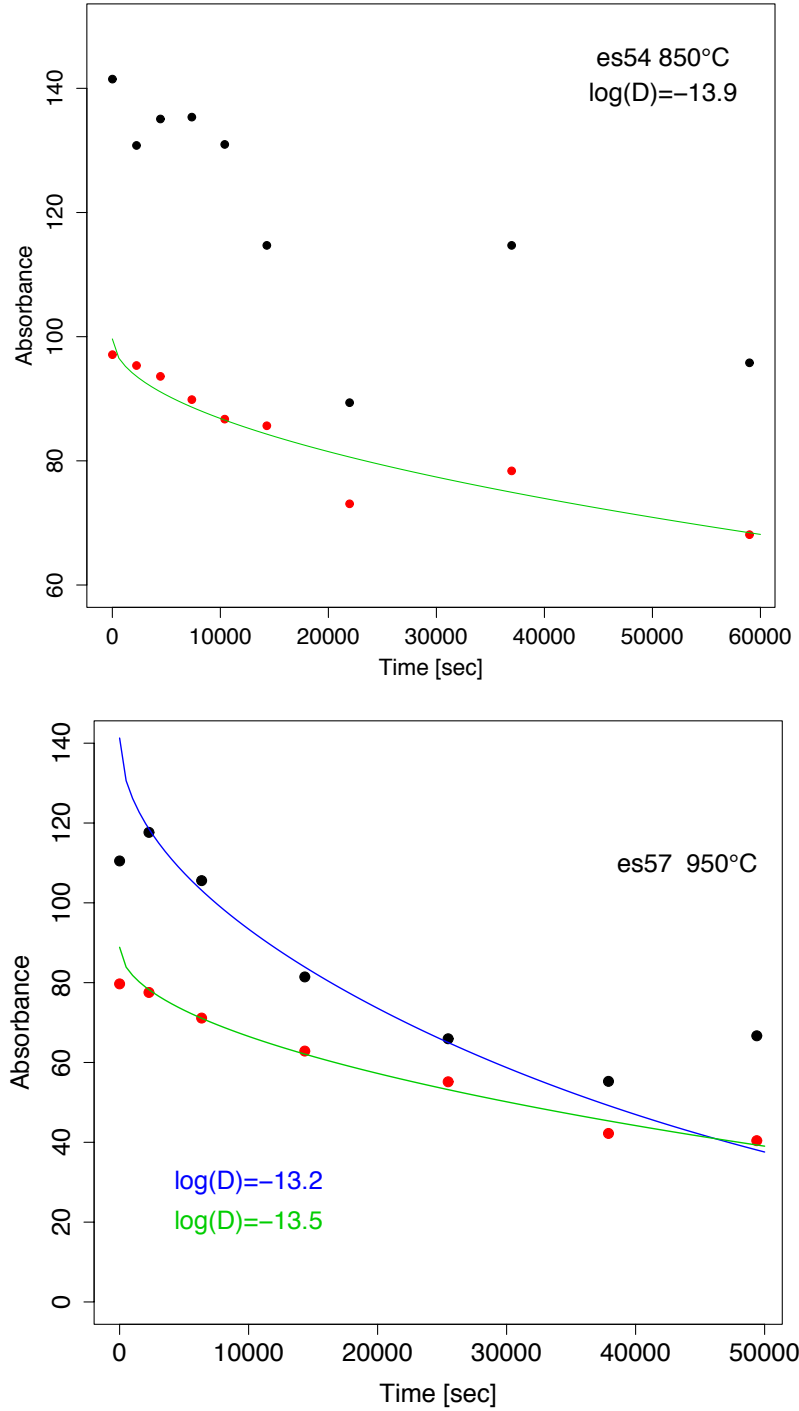


Figure 5.2.: Time series of dehydration; black dots: total absorbance, red dots: absorbance without neglected peaks around 3200 cm⁻¹ and 3420 cm⁻¹. Lines: fitted diffusion equation, diffusion coefficients given as $\log(D)$. Dopants: es5-4 contains 0.67 wt% Al₂O₃ and 2.26 wt% FeO; es5-7 contains 0.43 wt% Al₂O₃ and 1.60 wt% FeO (see also Tab. 6.2).

5.3. Evaluation of IR-spectra of annealed samples

In contrast to several calibrations for H_2O in NAMs, no calibration exists for IR-spectra of D_2O . OH- and OD-absorbance in enstatite are linearly correlated. The extinction coefficient for OH is 1.79 times greater than the extinction coefficient for OD in pure and Cr-doped enstatite (Stalder and Behrens, 2006). This factor, could not be confirmed in the H/D-exchange experiments of this study and was therefore not applied to the results. Possible reasons for the disagreement are the varying data quality, the abovementioned difficulties in spectra evaluation, and the fact that all H/D-exchanges were only partly completed in this study. The factors were deduced from a linear fit of OH-absorbance versus OD-absorbance, assuming that the concentration of hydrogen plus deuterium remains constant. Factors obtained from time series H/D-exchange experiments as well as from H/D-profiles across crystals after one annealing experiment are summarized in Table 5.3. The factor scatters around 1 for pure enstatite. For most doped samples, the factor is >1 , possibly due to the more complicated baseline correction in these samples. The chemical compositions of the samples in Table 5.3 are summarized in Table 7.3. Factors with values between 0.8 and 1.2 were ignored in the calculation of the diffusion coefficient.

5. Diffusion experiments

Table 5.3.: Linear correlation factors between the extinction coefficients of OH and OD. More details about the samples are given in Table 7.2. Sample es23-2: the peaks around 3060 and 3200 cm^{-1} and the equivalent OD-peaks were excluded, because otherwise the variability of these peaks would hamper the linear correlation. Sample es24-3: the peaks around 3060, 3200, and 3410 cm^{-1} and the equivalent OD-peaks were excluded for the same reason.

	Sample	T [$^{\circ}\text{C}$]	Orientation	Factor	Experiment
pure enstatite	es4-7	810	(100)	1.19	time series, 2 kbar
	es4-9	750	(100)	0.97	time series, 2 kbar
	es4-8	700	(100)	1.10	time series, 2 kbar
	es23-2	650	(010)	0.98	time series, 2 kbar
	pen1	796	(100)	0.88	profile, 1 atm
	es27-1	768	(010)	0.82	profile, 1 atm
enstatite + Al	es29-1b	810	(100)	1.57	time series, 2 kbar
	es29-3	700	(001)	2.01	time series, 2 kbar
	es29-2	700	(100)	1.17	time series, 2 kbar
	es11-2a	800	(001)	2.72	profile, 1 atm
	es11-1	853	(010)	1.26	profile, 1 atm
	es11-3	802	(100)	0.84	profile, 1 atm
enstatite + Al + Fe	es5-5	810	(100)	2.33	time series, 2 kbar
	es5-5	810	(010)	0.95	time series, 2 kbar
	es24-3	750	(100)	1.68	time series, 2 kbar
	es3-4	650	(100)	2.36	time series, 2 kbar
	es16-3b	843	(100)	1.42	profile, 1 atm

6. Results of hydrogen extraction experiments

Synthetic single crystals of three different types were used for the hydrogen extraction experiments: aluminium-bearing enstatite, and aluminium and iron bearing orthopyroxenes with three different Fe:Al ratios. The aim of these experiments was to investigate the influence of aluminium and iron on dehydration kinetics and mechanisms in orthopyroxene, two abundant constituents in the Mg-rich orthopyroxenes of Earth's upper mantle. It has been found earlier, that iron in pyroxene accelerates dehydration, because removal of a proton can be charge balanced by oxidation of divalent iron to trivalent iron, enabling hydrogen atoms to move through the crystal lattice by the redox reaction $1/2 \text{H}_2 + \text{Fe}^{3+} \Rightarrow \text{H}^+ + \text{Fe}^{2+}$ (e.g., [Skogby and Rossman \(1989\)](#); [Bromiley et al. \(2004\)](#); [Stalder and Skogby \(2007\)](#)). In contrast, aluminium was expected to decelerate dehydration, because the mobility of protons associated with Al-defects would be governed by the mobility of the whole point-defect. This is supported by the results depicted in Figure 6.1. The iron bearing samples clearly dehydrate faster than the iron free, aluminium-bearing orthopyroxenes and dehydration becomes faster with increasing iron content.

Despite the large errors of the diffusion coefficients of the two most iron rich samples (es17-1a, es17-2, Tab. 6.2), the enhancing effect of iron on dehydration is illustrated by these samples. One of the given diffusion coefficients possesses a comparatively large error, as the samples were dehydrated during electrical conductivity measurements. Both samples were heated up relatively slowly to the final temperature, during about 50 minutes. In the case of the

6. Results of hydrogen extraction experiments

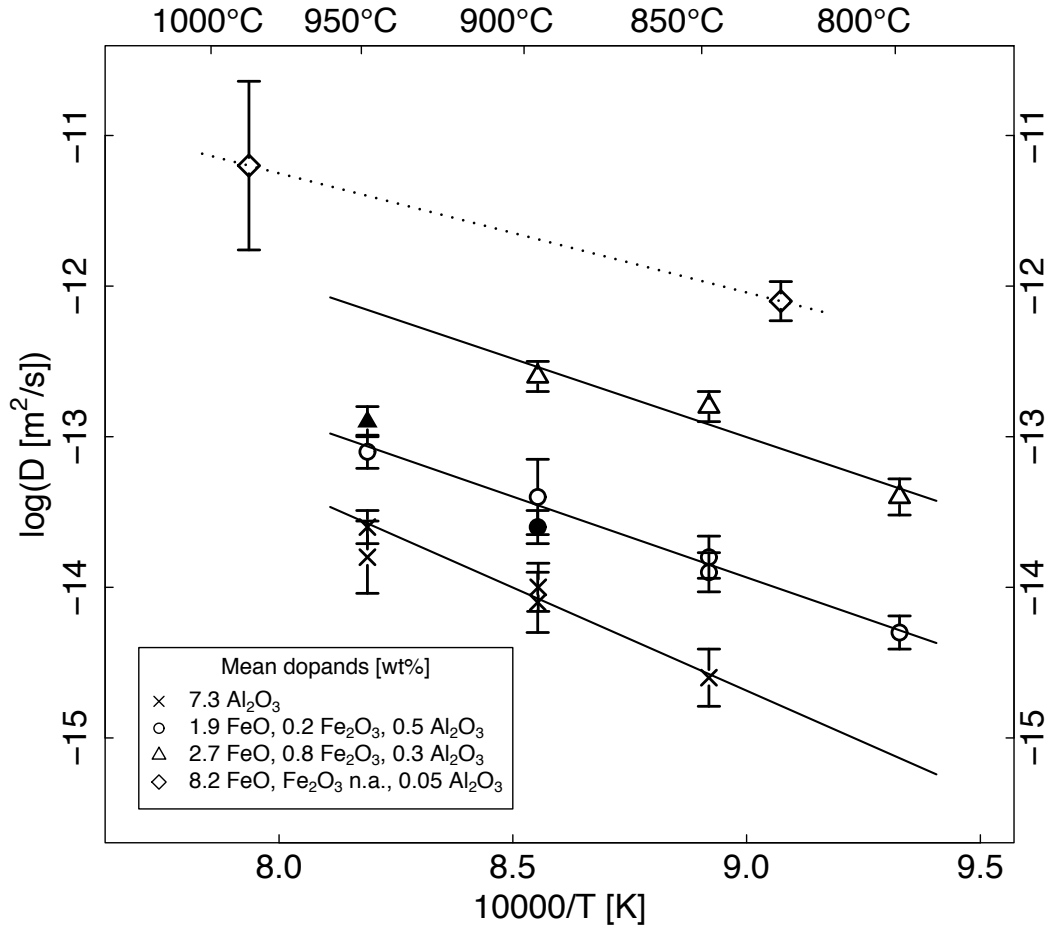


Figure 6.1.: Arrhenius plot for dehydration of orthopyroxenes of various compositions. Open symbols are $\parallel[100]$ and closed symbols are $\parallel[010]$. The mean chemical compositions are given in the legend. The exact chemical compositions of the samples are summarized in Table 6.2.

Table 6.1.: Diffusivity-parameters for dehydration of orthopyroxene: D_0 is the preexponential factor and E_a the activation energy. "Samples" denotes the sample group, e.g., es7-x means samples es7-2, es7-3, and es7-5. Errors of D_0 and E_a are given in parentheses. All diffusion parameters are determined for the crystallographic direction [100]

Samples	Mean wt-% of dopant	D_0 [m ² /s]	E_a [kJ/mol]
es7-x	7.8 Al ₂ O ₃	4.3 (± 1.8) e-03	262 (± 30)
es5-x	1.9 FeO + 0.2 Fe ₂ O ₃ + 0.5 Al ₂ O ₃	5.3 (± 0.7) e-05	205 (± 20)
es9-x	2.7 FeO + 0.8 Fe ₂ O ₃ + 0.3 Al ₂ O ₃	2.4 (± 0.9) e-04	200 (± 51)
es17-x	8.2 FeO + 0.05 Al ₂ O ₃	1.2 (± 0.1) e-05	151 (± 65)

diffusion coefficient at the higher temperature, 990°C, the end temperature was held constant for 25 minutes, yielding a large time error. The diffusion coefficient at the lower temperature, 830°C, has a smaller error because the final temperature was held constant for two and a half hours. Each diffusion coefficient was calculated for the final temperature. Due to the absence of a concentration plateau in both profiles (Appendix B.10), the initial concentrations C_0 were estimated, based on the OH-absorbances of the untreated samples. In order to measure a concentration profile across the samples, they were cut perpendicular to the faces after the dehydration experiment. Comparison of several IR-measurements of samples from the same synthesis yielded absorbance contributions of $\sim 60\%$ $\parallel[001]$, $\sim 30\%$ $\parallel[010]$, and $\sim 10\%$ $\parallel[100]$. Because the faces of the two iron rich samples were originally oriented $\parallel(100)$ and were oriented $\parallel(010)$ after cutting perpendicular, the IR-measurements of the untreated samples consisted of the contributions $\parallel[001]$ and $\parallel[010]$, adding up to about 90% of the total absorbance. The parameter C_0 was therefore estimated from the fresh sample's OH-absorbance minus 20%.

Three samples (es7-2, es9-1, and es5-3) were first dehydrated at 800°C and subsequently annealed at higher temperatures. The Fe- and Al-bearing samples es5-3 and es9-1 were both annealed at 800 and 850°C, and the Al-bearing sample es7-2 was used for all four temperatures. The diffusivity might be

6. Results of hydrogen extraction experiments

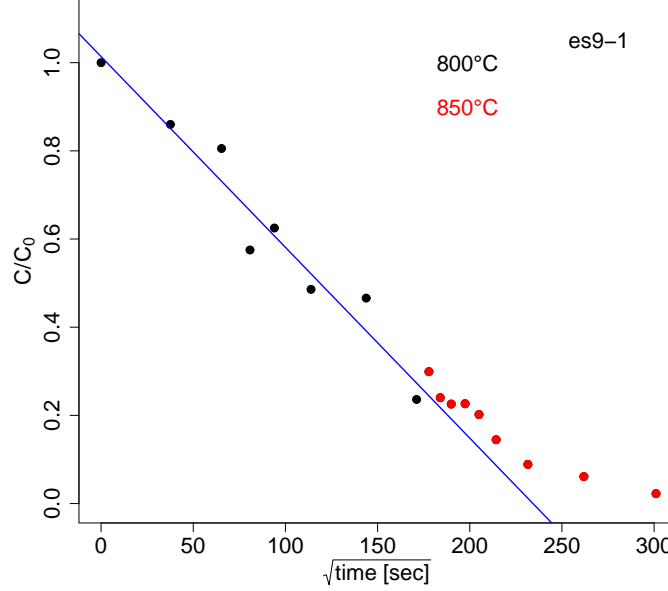


Figure 6.2.: Linearised time series of sample es9-1

underestimated for a sample, which already had developed a concentration profile before. The degree of underestimation depends on the length of the initial concentration profile, and could possibly be smaller than the analytical error of the diffusion coefficient.

The quasilinear representation of the time series C/C_0 vs. \sqrt{t} flattens out at $C/C_0 < 0.5$, as shown for sample es9-1 in Fig. 6.2. The diffusion coefficient deduced from sample es9-1 at 850°C is underestimated by ~ 0.3 log-units compared to the chemically similar, initially untreated sample es9-2 (Tab. 6.3). This is due to a too low C/C_0 at the beginning of the second annealing temperature, so later points deviate substantially from linear behaviour.

The diffusion coefficient is related to the slope S in the linear range of data by

$$D = \frac{\pi d^2 S^2}{16} \quad (6.1)$$

with d being the sample thickness.

The diffusion coefficient for the second temperature of es5-3 is within error supported by a chemically similar, initially untreated sample, es5-4, annealed at the same temperature (Tab. 6.3). For sample es7-2 no diffusion coefficient could be deduced for 800°C, the first temperature, because the OH-absorbance did not decrease during the heat treatment. The diffusion coefficient for the third temperature, 900°C, is supported by the diffusion coefficient of the chemically similar, initially untreated sample es7-5. The diffusion coefficient of es7-2 for 850°C is justified by the consistency of the diffusion coefficients at 900°C, determined after the heat treatment at 850°C, and by the fact, that during the heat treatment at 800°C, virtually no change in hydrogen concentration occurred. The diffusion coefficient for the fourth temperature, 950°C, is not well constrained due to few datapoints in the time series. Nevertheless it matches the more reliable diffusion coefficient of the initially untreated sample es7-3 within error.

The errors given in Table 6.1 were computed from the standard deviation of the linear regression. Details on the fitting of diffusion profiles and assumptions are given in Appendix B.1.

6. Results of hydrogen extraction experiments

Table 6.2.: Chemical composition of samples used for dehydration experiments. Standard deviations of EMPA-data are given in parantheses. Möbbauser analyses were done after the dehydration experiments. Estimated percentage of trivalent iron is indicated as "est.". .

Sample	EMPA analyses [wt%]					Möbbauser analyses [% of total Fe]				
	SiO ₂	MgO	Al ₂ O ₃	FeO		Fe _{M2} ²⁺	Fe _{M1} ²⁺	Fe _{oct} ³⁺	Fe _{tet} ³⁺	% Fe ³⁺
es9-1	58.97(0.31)	38.34(0.19)	0.21(0.03)	2.43(0.27)			— n.a.	—		20 (est.)
es9-2	57.89(0.98)	36.47(1.54)	0.47(0.28)	5.00(1.71)			— n.a.	—		20 (est.)
es9-5	58.59(0.46)	37.53(0.76)	0.25(0.09)	3.51(0.85)		60.53	16.7	17.08	5.69	22.77
es9-6	58.64(0.20)	38.02(0.32)	0.18(0.04)	2.90(0.43)		55.05	20.63	20.19	4.14	24.33
es5-3	58.70(0.16)	38.49(0.22)	0.47(0.06)	2.03(0.19)			— n.a.	—		8 (est.)
es5-4	58.78(0.31)	38.23(0.12)	0.67(0.08)	2.26(0.21)		71.50	23.43	5.08	0.00	5.08
es5-6	58.44(0.64)	38.15(0.72)	0.51(0.23)	2.37(0.41)		69.77	20.02	8.17	2.04	10.21
es5-7	59.04(0.34)	38.82(0.25)	0.43(0.05)	1.60(0.06)		74.48	16.02	7.84	1.66	9.50
es7-2	55.63(1.06)	37.47(0.78)	6.55(1.48)	0.03(0.01)						
es7-3 ^a	54.29(1.21)	36.08(0.57)	9.25(1.66)	0.02(0.01)						
es7-5	55.83(1.11)	37.75(0.87)	5.93(1.48)	0.02(0.01)						
es17-1a	57.55(0.89)	33.24(2.08)	0.07(0.05)	10.24(0.80)			— n.a.	—		20 (est.)
es17-2	58.82(0.18)	36.32(0.36)	0.03(0.02)	6.08(0.51)			— n.a.	—		20 (est.)

^aBecause no EMS analysis of sample es7-3 was done, the chemical composition given for sample es7-3 is an estimate, based on several EMS analyses of crystals of the same synthesis.

Table 6.3.: Results from H-extraction experiments. $\Delta \log(D)$ is calculated using the Gaussian error propagation law.

Sample	Thickness [μm]	Temperature [$^{\circ}\text{C}$]	$-\log(D \text{ [m}^2/\text{s]})$	$\Delta \log(D)$	Crystallogr. dir.	Data
es9-1	105	800	13.4	0.12	[100]	time-series
es9-1		850	13.1	0.11		
es9-2	110	850	12.8	0.10	[100]	time-series
es9-5	150	900	12.6	0.10	[100]	time-series
es9-6	130	950	12.9	0.10	[010]	time-series
es5-3	150	800	14.3	0.11	[100]	time-series
es5-3		850	13.8	0.14		
es5-4	188	850	13.9	0.13	[100]	time-series
es5-6	120	900	13.6	0.11	[010]	time-series
es5-6			13.4	0.25	[100]	profile
es5-7	165	950	13.1	0.11	[100]	time-series
es7-2	265	800	n.a.	0.19 0.20 0.24	[100]	time-series
es7-2		850	14.6			
es7-2		900	14.1			
es7-2		950	13.8			
es7-5	140	900	14.0	0.16	[100]	time-series
es7-3	105	950	13.6	0.11	[100]	time-series
es17-2	185	829	12.1	0.13	[100]	profile
es17-1a	305	987	11.2	0.56	[100]	profile

7. Results of H/D-exchange experiments

Three types of orthopyroxenes were used for H/D-exchange experiments: pure enstatite, enstatite with ~ 2 wt% of Al_2O_3 , and with ~ 0.6 wt% Al_2O_3 plus ~ 2 wt% FeO total iron. In the hydrogen-bearing samples, OH- and OD-absorbances were monitored as a function of time through the bulk crystal plate. In addition, initially deuterium-bearing crystal-plates were cut perpendicular to the faces after one annealing experiment with hydrogen gas at ambient pressure and a profile of OH- and OD-absorbance was measured across the sample. Experimental conditions and diffusion coefficients of H/D-exchange are given in Table 7.2 and the resulting activation energies and preexponential factors are summarised in Table 7.1.

The experimental pressure has no or very little effect on the diffusivity. Diffusion coefficients obtained in this study for pure enstatite agree well with the results of [Stalder and Behrens \(2006\)](#), although the first were obtained at 2 kbar and the latter at ambient pressure. Thus, diffusion parameters for H/D-exchange in pure enstatite were calculated from combining the data of this study, including diffusion coefficients of 2 kbar and ambient pressure experiments, and the previously determined diffusion coefficients by [Stalder and Behrens \(2006\)](#). The resulting activation energy of H/D-exchange in pure enstatite is higher than previously determined by these authors: $+22$ kJ/mol $\parallel[100]$, the deviation is still in the range of error, and $+56$ kJ/mol $\parallel[010]$.

The anisotropy of diffusion, $D \parallel [010] < D \parallel [100] < D \parallel [001]$, reported for pure enstatite by [Stalder and Behrens \(2006\)](#), is supported also for aluminous enstatite

7. Results of H/D-exchange experiments

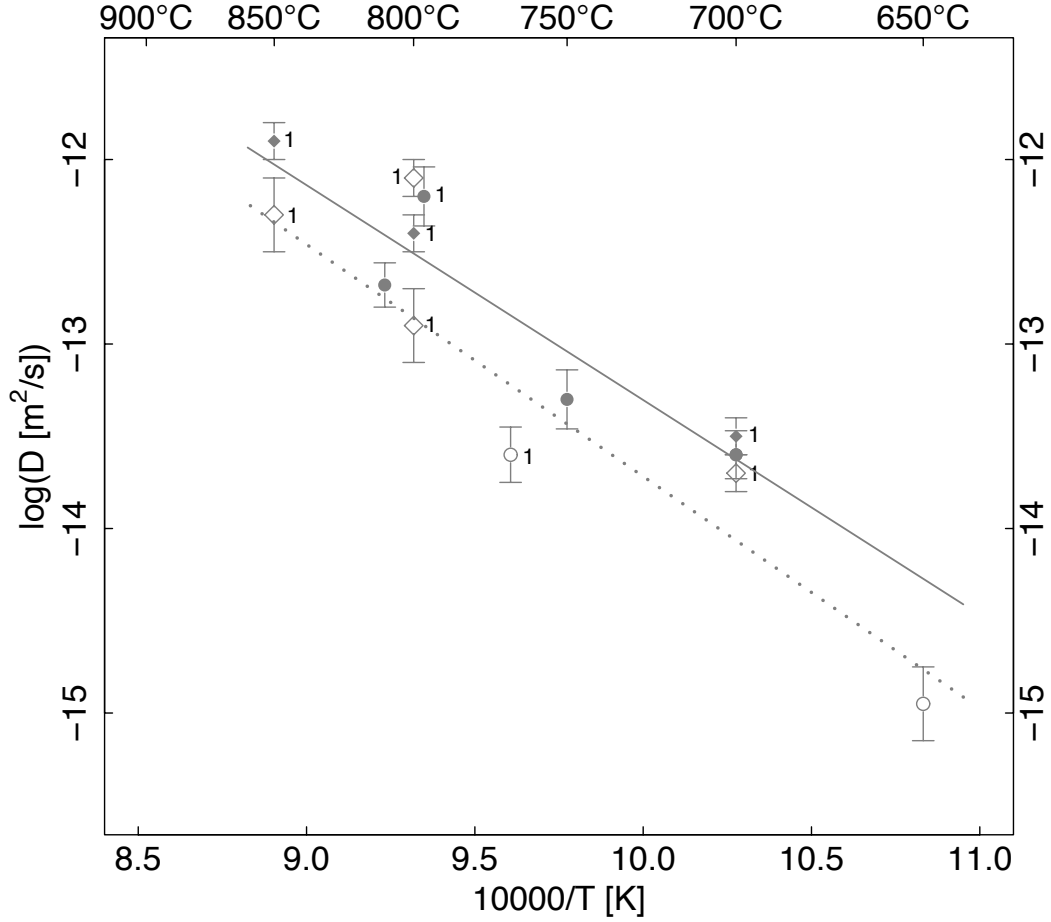


Figure 7.1.: Arrhenius plot of H/D-exchange diffusivity of pure enstatite. Dots and circles indicate data of this study, diamonds denote data from [Stalder and Behrens \(2006\)](#). The annotation "1" denotes data obtained at ambient pressure, other data was obtained from experiments at 2 kbar. Open symbols are diffusion coefficients $\parallel[010]$ and closed symbols are $\parallel[100]$. The solid line represents the linear regression of diffusion coefficients $\parallel[100]$, the dotted line is the regression line for diffusion $\parallel[010]$.

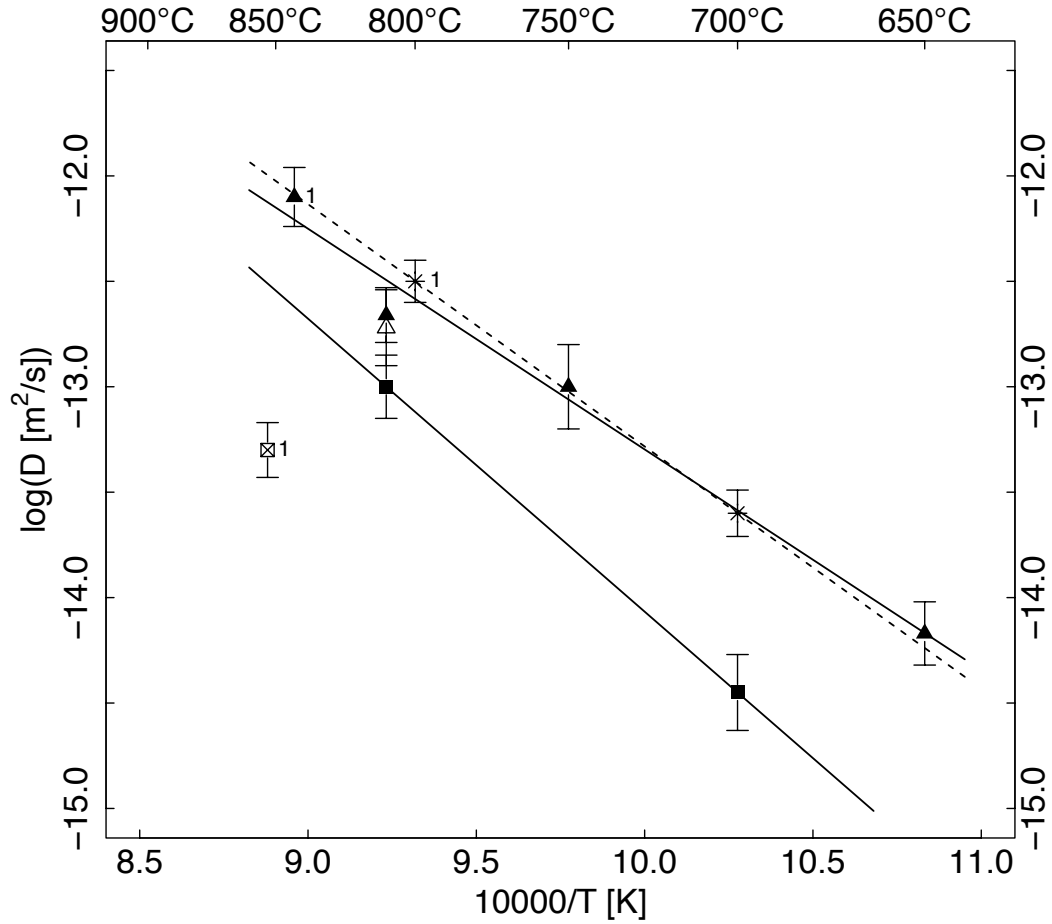


Figure 7.2.: Arrhenius plot of H/D-exchange diffusivity of doped enstatite. Triangles: enstatite with ~ 2 wt% FeO and ~ 0.6 wt% Al_2O_3 , squares and asterisks: enstatite with ~ 2 wt% Al_2O_3 . The annotation "1" indicates data obtained at ambient pressure, all other data were obtained at 2 kbar. Open symbols are diffusion coefficients $\parallel[010]$, filled symbols are $\parallel[100]$, and asterisks are $\parallel[001]$. Solid lines represent the linear regression of diffusion coefficients $\parallel[100]$, the broken line is the regression line for diffusion $\parallel[001]$.

7. Results of H/D-exchange experiments

Table 7.1.: Diffusion-parameters for H/D-exchange in orthopyroxene: D_0 is the preexponential factor and E_a the activation energy. The errors of D_0 and E_a were deduced from the standard deviation and are given in parentheses.

Dopant		D_0 [m ² /s]	E_a [kJ/mol]
Al ₂ O ₃	[001]	1.6 (± 1.1) e-02	220 (± 40)
	[100]	5.7 (± 1.5) e-02	246 (± 60)
FeO + Al ₂ O ₃	[100]	1.5 (± 0.2) e-03	200 (± 20)
pure enstatite	[100]	2.2 (± 0.2) e-02	223 (± 22)
	[010]	7.2 (± 0.2) e-02	241 (± 31)

(Fig. 7.2). The activation energy of H/D-exchange diffusivity of Fe-Al-doped orthopyroxene is smaller than of iron-free enstatite. The activation energy of aluminous enstatite ||[100] is the highest, but possesses a large uncertainty originating from the limited availability of diffusion coefficients and from the difficulties of IR-spectra evaluation (see also Appendix B.22, B.25, and B.36).

The most obvious effect of the dopant aluminium in enstatite is that H/D-exchange diffusivity is decelerated with respect to pure enstatite. The dopand iron has — at least in the investigated concentration — only little effect on H/D-exchange. Since the activation energy of the iron-bearing samples is lower, their diffusivity is enhanced with respect to pure enstatite only at temperatures below 730°C.

In most cases, the diffusion coefficient of hydrogen is equal or higher than the diffusion coefficient of deuterium (Table 7.2). There are two possible reasons for $D_H > D_D$: (1) The isotope effect, which says that the heavier isotope is the slower one. The ratio of the diffusion coefficients of two isotopes is $D_1/D_2 = \sqrt{m_2/m_1}$, where m_1 and m_2 are the molar weights of the isotopes, leading to a constant ratio of $D_H/D_D = \sqrt{2} = 1.4$. For samples es27-1 and es16-3b applies $D_H/D_D=1.4$ and $D_H/D_D=1.2$, respectively, indicating an isotope effect. (2) Desorption is faster than sorption. This seems to apply to

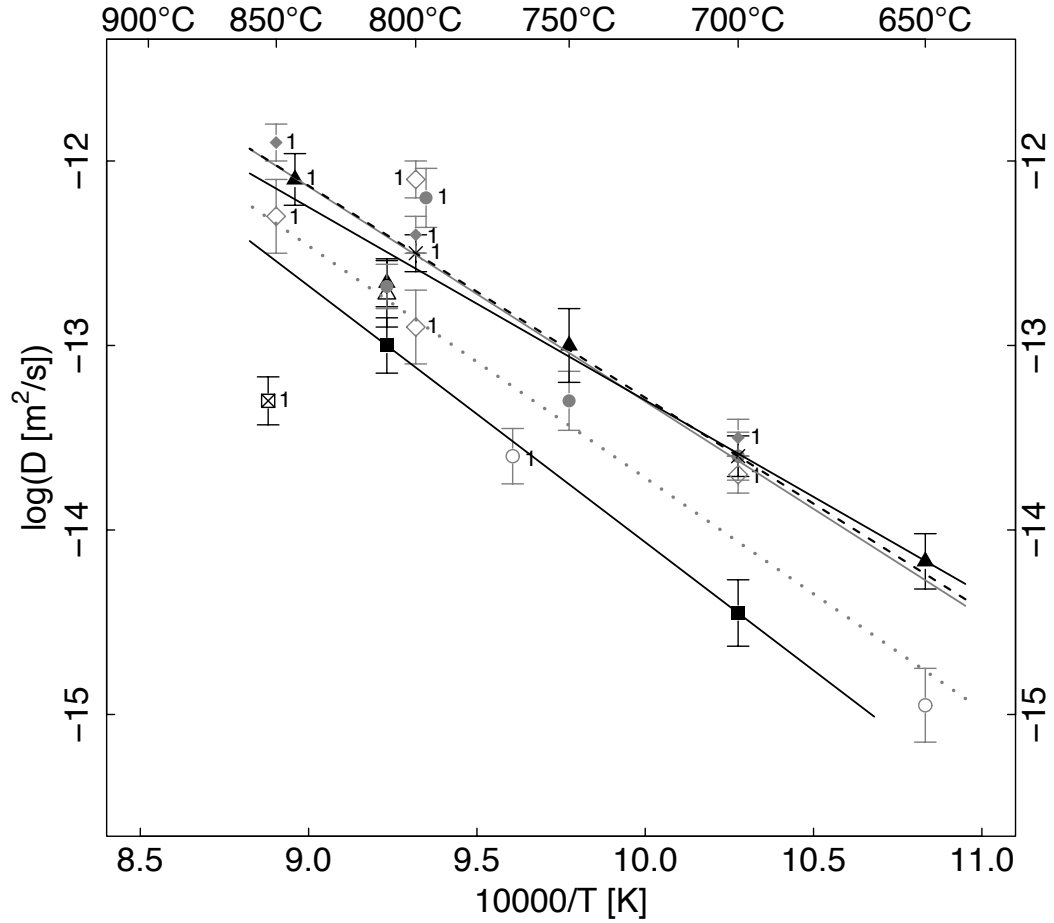


Figure 7.3.: Arrhenius plot comparing the H/D-exchange diffusivities of all samples. Grey data indicate pure and black doped enstatite. Diamonds: pure enstatite from [Stalder and Behrens \(2006\)](#), dots and circles: pure enstatite this study, squares and asterisks: enstatite with Al, triangles: enstatite with Fe and Al. Diffusion coefficients obtained from experiments at 1 atm are indicated with a "1", all other diffusion coefficients were obtained from experiments at 2 kbar. Open symbols: [010], filled symbols: [100], asterisks: [001]. Solid lines: linear fit [100], dotted line: linear fit [010], broken line: linear fit [001].

7. Results of H/D-exchange experiments

sample pen1, in which $D_D > D_H$ and D was the desorbed species. The difference between sorption and desorption might be somehow caused by the interface between fluid/gas phase and solid crystal. The result of sample es5-5 $\parallel[010]$ cannot be explained in this way, because $D_D > D_H$ and H is the desorbed species. Because the reason for the differing diffusion coefficients is not clear, always the greater diffusion coefficient was considered.

Table 7.2.: Results from H/D-exchange experiments. Errors are given in parentheses. The pressure of the time-series experiments was 2 kbar and the profiles were obtained from experiments at ambient pressure.

Sample	Thickness [μm]	Temperature [$^{\circ}\text{C}$]	$-\log(D_H [\text{m}^2/\text{s}])$	$-\log(D_D [\text{m}^2/\text{s}])$	Crystallogr. dir.	Data
es3-4	178	650 $^{\circ}\text{C}$	14.2 (0.15)	14.2 (0.13)	[100]	time-series
es23-2	133		15.0 (0.20)	15.2 (0.12)	[010]	time-series
es4-8	125	700 $^{\circ}\text{C}$	13.6 (0.13)	13.6 (0.12)	[100]	time-series
es15-2	210		15.3 (0.49)	15.3 (0.20)	[010]	time-series
es29-2	182		14.5 (0.18)	14.6 (0.13)	[100]	time-series
es29-3	238		13.6 (0.11)	13.6 (0.12)	[001]	time-series
es4-9	132	750 $^{\circ}\text{C}$	13.3 (0.16)	13.4 (0.12)	[100]	time-series
es24-3	208		13.0 (0.20)	13.0 (0.10)	[100]	time-series
es4-7	157	810 $^{\circ}\text{C}$	12.7 (0.12)	12.8 (0.11)	[100]	time-series
es5-5	277		12.7 (0.13)	12.7 (0.10)	[100]	time-series
	423		12.7 (0.18)	12.6 (0.11)	[010]	time-series
es29-1b	292		13.0 (0.15)	13.0 (0.13)	[100]	time-series
pen1	190	850	12.4 (0.24)	12.2 (0.16)	[100]	1 atm, profile
es11-1	180	900	13.3 (0.14)	13.3 (0.13)	[010]	1 atm, profile
es11-2a	220	950	12.5 (0.10)	12.6 (0.13)	[001]	1 atm, profile
es16-3b	193	950	12.1 (0.14)	12.2 (0.16)	[100]	1 atm, profile
es27-1	193	829	13.4 (0.15)	13.6 (0.24)	[010]	1 atm, profile

Table 7.3.: Chemical composition of samples used for H/D-exchange experiments. Standard deviations of EMPA-data are given in parantheses. Data of samples es4-7 and es23-2 are estimated, based on similar samples; pen1 is pure enstatite. Compositions of samples es3-4 and es5-5 are based on analysis of several other crystals of the same synthesis.

Sample	SiO ₂	MgO	Al ₂ O ₃	FeO
es4-7	59	38	0.03	0.03
es4-8	59.83(0.28)	38.70(0.25)	0.04(0.01)	0.01(0.05)
es4-9	58.82(0.17)	37.85(0.05)	0.03(0.01)	0.04(0.01)
es23-2	59	38	0.03	0.03
pen1	n.a.	n.a.	n.a.	n.a.
es27-1 ^a	60.23(0.23)	38.87(0.14)	0.03(0.02)	0.03(0.02)
es3-4	58.38(0.71)	37.34(1.25)	0.90(0.56)	3.20(1.39)
es5-5	56.89(4.46)	37.11(2.93)	0.64(0.21)	2.25(0.42)
es15-2	58.45(0.32)	35.93(0.43)	0.72(0.16)	2.92(0.42)
es24-3 ^b	59.07(-)	37.23(-)	0.77(-)	3.08(-)
es16-3b	58.04(0.41)	36.59(0.31)	0.51(0.05)	1.70(0.14)
es29-1b	57.39(0.29)	36.60(0.32)	2.25(0.43)	0.01(0.06)
es29-2	58.08(0.27)	37.16(0.31)	2.71(0.12)	0.01(0.03)
es29-3	58.49(0.18)	37.32(0.26)	1.61(0.06)	0.02(0.03)
es11-1	58.43(0.73)	39.20(0.57)	3.65(1.26)	0.01(0.02)
es11-2a	59.19(0.20)	37.42(0.27)	1.99(0.08)	0.00(0.03)

^aThe chemical composition given for sample es27-1 is the EFM-analysis of es27-3, originating from the same synthesis.

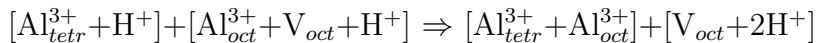
^bBecause only one analysis was made, no standard deviations are available.

7. Results of H/D-exchange experiments

8. Discussion

The diffusivities of H/D-exchange are higher than most of the diffusivities of hydrogen extraction (Fig. 8.1). Only the samples containing 6 and 10 wt% FeO total iron dehydrate as fast as the results from H/D-exchange experiments. H/D-exchange and dehydration in the samples containing about 0.6 wt% Al_2O_3 and 2 wt% FeO differ by 1.5 log-units. The difference for pure enstatite is slightly larger than one order of magnitude. Aluminium bearing, iron free samples show a difference of ~ 2 log-units between both diffusivities. Taking into account that the samples used for dehydration experiments contained ~ 7 wt% Al_2O_3 and H/D-exchange was determined for enstatite with 2 wt% Al_2O_3 , the difference between the two diffusivities might be somewhat smaller than 2 log units for equal Al-concentrations.

Dehydration of orthopyroxene is slower than H/D-exchange, because the protonated point-defects can only release their proton, when a new local configuration of charge neutrality is provided and lattice strain is minimized. This involves either rearrangement or annihilation of the respective point-defects. The decelerating effect of aluminium on hydrogen diffusion suggests that aluminium forms stable point defect complexes in orthopyroxene. As microscopic exsolution of an Al-phase at surfaces or microscopic Al-rich inclusions were never observed, the point defect complexes are possibly dehydrated by forming pairs or submicroscopic complexes of more than two Al-atoms. A possible rearrangement reaction is:



where the point-defect complexes are in square brackets. Two protonated Al-defects fuse to one Tschermak's defect, and the remaining octahedral vacancy

8. Discussion

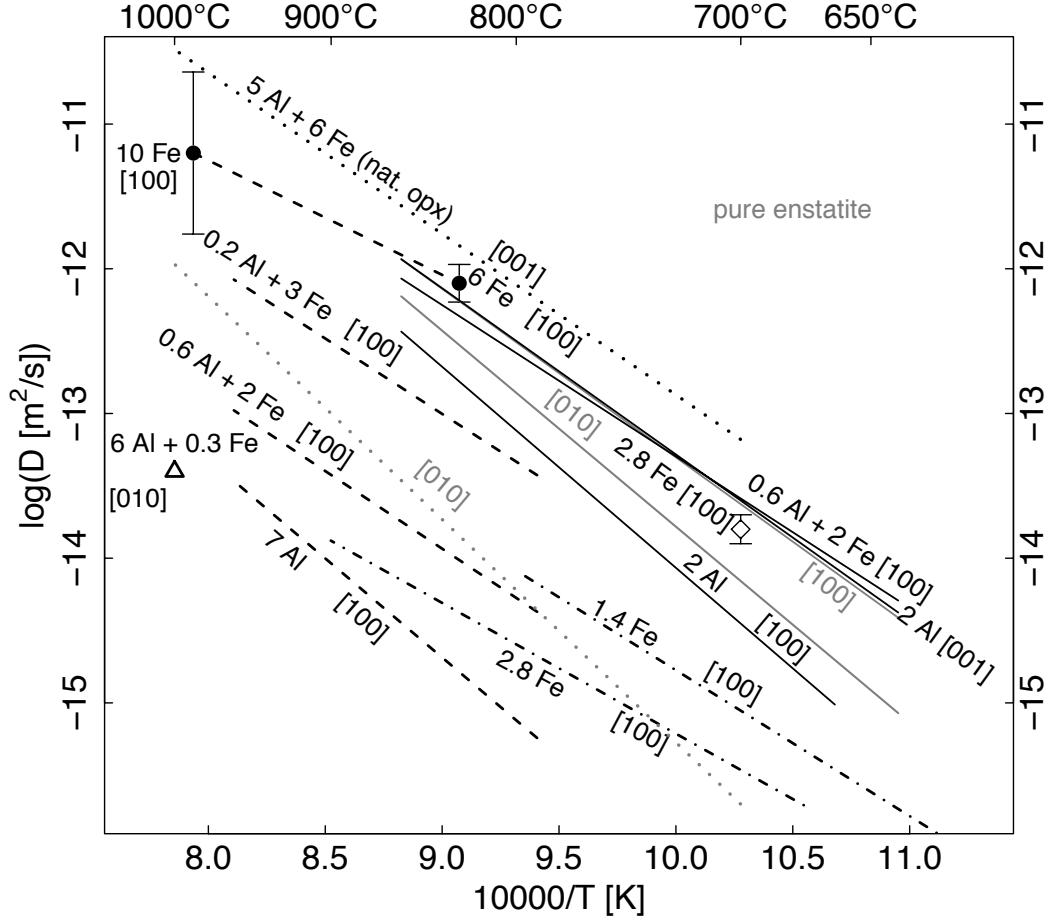
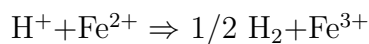


Figure 8.1.: Compilation of hydrogen diffusion data of orthopyroxene. Solid lines: H/D-exchange, dashed lines: H-extraction, dotted lines: H-extraction from [Stalder and Skogby \(2003\)](#), dashed-dotted lines: H-extraction from [Stalder et al. \(2007\)](#), diamond: H/D-exchange from [Stalder et al. \(2007\)](#), triangle: H-extraction from [Stalder and Skogby \(2007\)](#), dots: H-extraction from this study. The numbers indicate the Al_2O_3 - and FeO-content in wt% respectively. All grey lines refer to pure enstatite. The natural orthopyroxene contains several minor elements which are not indicated here, the iron-bearing samples of the two dots contain additionally 0.05 wt% Al_2O_3 . Crystallographical orientations are indicated in square brackets.

is charge balanced by the two protons. This configuration may be energetically favourable, because dehydration diffusivity for pure enstatite (Stalder and Skogby (2003), grey dotted line in Fig. 8.1) shows that the protonated octahedral vacancies are more mobile than the Al-point-defects and can be annihilated by diffusing to the surface of the crystal. Moreover, EMPA-analyses suggest that Al is incorporated mainly through the Al-Tschermak's substitution (Section 3.1). However, the above reaction implies that in Al-bearing samples, some OH-bands increase at the cost of others, i.e., the OH-bands of the defects $[\text{Al}_{\text{tet}}^{3+} + \text{H}^+]$ and $[\text{Al}_{\text{oct}}^{3+} + \text{V}_{\text{oct}} + \text{H}^+]$ would decrease relatively fast, whereas the OH-band which corresponds to the defect $[\text{V}_{\text{oct}} + 2\text{H}^+]$ would increase or decrease more slowly. In fact, increasing IR-bands in Al-bearing samples were observed in dehydration experiments, but leading to a total increase of OH-absorbance (e.g., Appendix B.17, B.18, B.19). It is noteworthy that a possible site specific absorption coefficient, as it has been reported by Kovács et al. (2010) for olivine, has not been studied yet for orthopyroxene. A relatively high absorption coefficient of the increasing IR-band around 3400 cm^{-1} , which in addition may be pressure and/or temperature dependent, could lead to a total increase of absorbance. Except for the OH-peaks, which exhibited some irregular behaviour or increased with time, all peaks in aluminous orthopyroxene samples decreased approximately on the same timescale during dehydration. In any case, the irregular development of OH-absorbance indicates that an intrinsic relaxation process occurred during tempering which was similar or equal to the above reaction. The slower dehydration is probably related to the necessity of the deprotonated point-defects to achieve charge balance or diffuse to the surface of the crystal.

The dehydration process is facilitated by ferrous iron changing to ferric iron in order to charge balance an escaping hydrogen atom



(e.g., Skogby and Rossman (1989); Stalder (2004); Stalder and Skogby (2007)).

In other words, if Fe-bearing orthopyroxene is dehydrated, the flux of hydrogen

8. Discussion

atoms is charge-balanced by a counter flux of electron holes and the dehydration is governed by the diffusivity of electron holes. The fact that this hydrogen transport mechanism enhances hydrogen diffusivity and reduces the activation energy shows that electron holes are more mobile than any other point-defect in orthopyroxenes. The high dehydration diffusivities of the samples with 6 and 10 wt% FeO total iron suggest that dehydration is governed by the highly mobile electron holes in these samples.

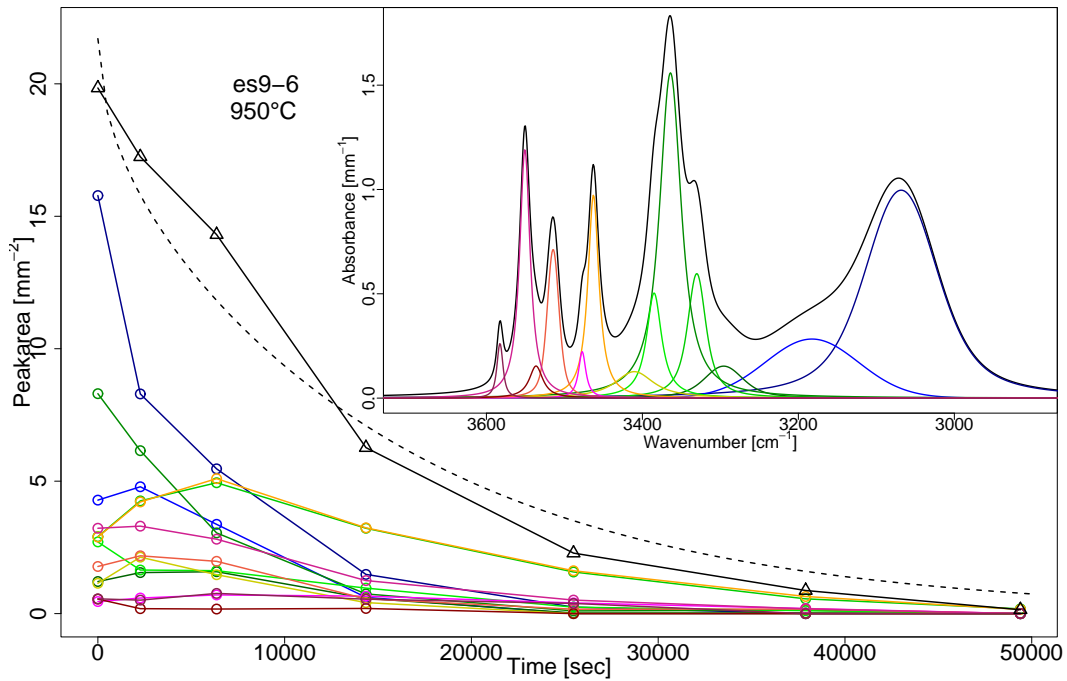


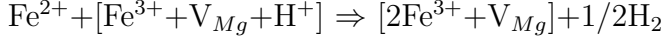
Figure 8.2.: OH-absorbance of individual peaks and total OH-absorbance (black) as a function of time. The broken line is the fitted diffusion Equation 5.6, the peak model applied to the IR-spectra is shown exemplarily in the inset. The OH-bands related to Fe^{3+} (3330 and 3460 cm^{-1}) show an initial increase, whereas the OH-bands assigned to Mg-vacancies (3060, 3200, 3360 cm^{-1}) decrease faster than the other peaks.

The dehydration reaction involving iron oxidation consists of two steps

(Stalder and Skogby, 2007):

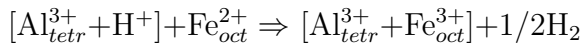


and



This is confirmed by the results of this study and is most clearly shown exemplarily with the evolution of the individual peaks of sample es9-6, dehydrated at 950°C in air (Fig. 8.2, B.16). The initial increase of the OH-bands centered at 3330 and 3460 cm^{-1} , probably corresponding to the point defect complex $[\text{Fe}^{3+} + \text{V}_{Mg} + \text{H}^+]$ (see also Section 1.3), mirrors the first partial reaction. The OH-bands assigned to protonated octahedral vacancies, centered at 3060, 3200, and 3360 cm^{-1} , decrease much faster than the other peaks, due to the enhanced deprotonation of octahedral vacancies through both reactions. In Fig. 8.2, the peaks at high wavenumbers, assigned to protonated aluminium point-defects, in between 3470 to 3650 cm^{-1} , increase also slightly. This increase is also exhibited by iron free aluminous samples and can be attributed to the abovementioned intrinsic equilibration of Al-point-defects. Although the Fe^{3+} -related OH-bands do not increase in all iron-bearing samples, the faster decrease of V_{oct} -related OH-bands was always observed (Appendix B.1).

Since the iron-bearing samples contained also aluminium and also exhibited aluminium related OH-bands, an analogous dehydration reaction involving the protonated Al-defects is possible:



Previous H-extraction results of synthetic, iron-bearing orthopyroxenes (dashed-dotted lines in Fig. 8.1) show that dehydration does not exclusively depend on iron content (Stalder et al., 2007). The results of this study suggest that dehydration is enhanced through aluminium, possibly due to the opportunity for deprotonated point-defects to fuse to Al-Fe-Tschermak's defects.

The **kinetics of H/D-exchange** show a similar dependency on the defect chemistry as dehydration, i.e., diffusivity becomes slower through incorporation of Al and is slightly enhanced in the Al- plus Fe-bearing samples with

8. Discussion

respect to pure enstatite. The results reflect that protonated Al-point-defects are more stable and less mobile than protonated octahedral vacancies. H/D-exchange in iron-bearing samples is slightly higher than in pure enstatite only below 730°C due to the low activation energy. H/D-exchange in orthopyroxene might increase with higher iron contents and exceed hydrogen diffusivity in pure enstatite also at higher temperatures. But since dehydration in the high-iron orthopyroxenes is very likely governed by the abovementioned iron-redox reaction, it probably marks approximately the upper limit for hydrogen diffusivity in iron-bearing orthopyroxene. Diffusivity of H/D-exchange therefore could possibly be enhanced through iron only up to this limit, and as a consequence, pure enstatite would possess the largest hydrogen diffusivity above ~850°C.

It can be concluded, that hydrogen is incorporated in orthopyroxene in point defect complexes involving vacancies and trivalent cations. Dehydration is governed by the kinetics of rearrangement-reactions and diffusivities of the point defect complexes. Aluminium reduces the mobility of hydrogen in orthopyroxene by the formation of relatively stable point defect complexes. Also H/D-exchange is decelerated through aluminium due to the higher stability of Al-H-point defect complexes. An exemption is provided by the presence of iron, which enables hydrogen to diffuse independently of the associated point defects and charge-balances protons by a counterflux of electron holes. The mobility of hydrogen in the most iron-rich orthopyroxenes, investigated in this study, is similar to hydrogen self-diffusivity, as indicated by the similarity between dehydration in the iron-rich samples and H/D-exchange. The results confirm the previous finding of the enhancing effect of iron on hydrogen diffusivity ([Stalder and Skogby, 2007](#)), and the hypothesis of the decelerating effect of aluminium on hydrogen diffusivity.

Part II.

Electrical conductivity of Enstatite

9. Introduction

The electrical conductivity of silicate minerals is determined by the concentration and mobility of point-defects and the concentration of polyvalent cations, providing mobile electrons. In a pure phase, electrical conductivity arises from intrinsic point-defects in the crystal, i.e., vacancies, interstitial ions, electrons, and electron holes. Impurities cause extrinsic point-defects, which may enhance electrical conductivity with respect to the pure phase. Electrical conduction in silicates is a thermally activated process, and these minerals can therefore be classified as semiconducting materials. An important characteristic of semiconductors is that even small concentrations of impurity cations have an enhancing effect on electrical conductivity by decreasing the energy gap between the valence band and the conduction band. Consequently, it is very difficult to determine the electrical conductivity of a pure phase.

The aim of this study was to investigate the effect of impurities, such as aluminium, ferric iron, and hydrogen, on the electrical conductivity of enstatite. Electrical conduction in orthopyroxene single crystals is dominated by ionic and electronic transport processes, but it is not a direct probe of them. Comparison of electrical conductivity with hydrogen diffusivity via the Nernst-Einstein relation (Eq. 14.1) is necessary to draw conclusions on the charged species and their transport mechanisms which cause the measured electrical conductivity.

10. Impedance spectroscopy

Impedance spectroscopy is used to characterise electronic components and to analyse various liquid and solid materials. A major application for solids is the investigation of transport properties of charge carriers. Through analysis of frequency domains, unwanted polarisation effects at the electrodes or other interfaces can be ruled out and low electrical conductivities can be measured. The methods of impedance spectroscopy and of data analysis are as diverse as the applications of this measurement technique. In the following, only the subject relevant for this study is described.

An alternating voltage (AC) is applied to the sample via two electrodes, brought into contact with the sample by dipping them into an electrolytic liquid or attaching them to the surface of a solid. Solid samples are usually planparallel plates with the electrodes attached to the faces. The alternating voltage can be described by the equation:

$$U = U(t) = U_0 \sin(\omega t + \phi_U) \quad (10.1)$$

U_0 is the amplitude, $\omega = 2\pi f$ is the angular frequency, and ϕ_U is the phase angle, which depends on the definition of the zero point of time. For convenience, the alternating signal is written in the complex form.

$$U = U(t) = U_0 \cos(\omega t + \phi_U) + i \sin(\omega t + \phi_U) \quad (10.2)$$

The voltage induces an alternating current in the sample, which is phase shifted with respect to the voltage and described by

$$I = I(t) = I_0 \cos(\omega t + \phi_I) + i \sin(\omega t + \phi_I) \quad (10.3)$$

10. Impedance spectroscopy

I_0 is the amplitude of the alternating current, and $\phi_I \neq \phi_U$ due to the phase shift. The impedance analyser measures the amplitude and the phase shift of

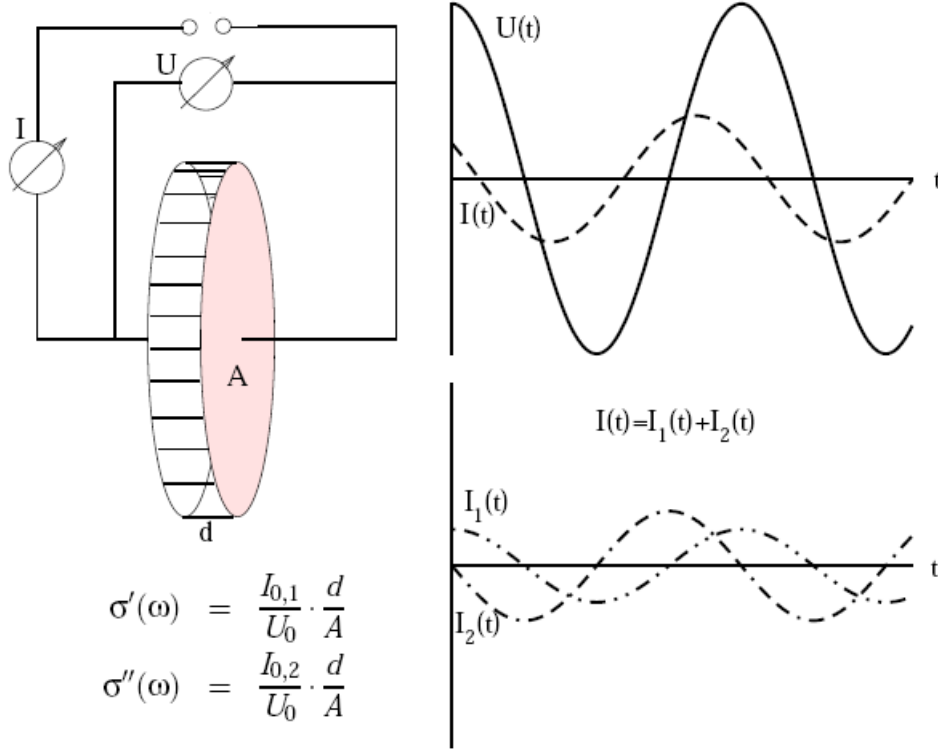


Figure 10.1.: Principle of impedance spectroscopy: A sample of thickness d is placed between two electrodes with area A . The induced current is characterized by its amplitude and phase shift. The real part (I_1) of the complex electrical conductivity is proportional to the amplitude and the imaginary part (I_2) is proportional to the phase shift. The picture was copied from [Funke \(2002\)](#).

the induced current. From the two quantities, the current signal can be divided into two parts, one oscillating in phase with the voltage, $I_1(t)$, the other one is phase shifted by $\pi/2$, $I_2(t)$ (Fig. 10.1). The amplitudes of the two currents are proportional to the real and the imaginary part of the complex electrical conductivity, respectively.

$$\sigma'(\omega) = \frac{I_{0,1}}{U_0} \cdot \frac{d}{A} \quad (10.4)$$

$$\sigma''(\omega) = \frac{I_{0,2}}{U_0} \cdot \frac{d}{A} \quad (10.5)$$

$$\sigma(\omega) = \sigma'(\omega) + i\sigma''(\omega) \quad (10.6)$$

d is the thickness of the sample, A the area of the electrodes, and $\sigma(\omega)$ the admittance, the AC-equivalent to the conductivity to continuous current (DC). The inverse of the admittance is the impedance, the AC-equivalent to the DC-resistance. The applied voltage is small, between 1 and 1.5 V, to maintain the linear ohmic relationship between voltage and current. The real part of the electrical conductivity, $\sigma'(\omega)$, is a measure for the dissipated energy in the system and can be regarded as an analogue to an ohmic resistance. It is called the conductance and reflects the translational jumps of ionic and electronic charge carriers. The imaginary part, $\sigma''(\omega)$, represents the stored energy in the system, analogous to a capacitor. It is also called the susceptance, as it is a measure of the ability of a material to interact with an electrical field in terms of rotational alignment of permanent dipoles and polarisation of atoms and molecules.

To investigate the transport properties and mobility of cations in orthopyroxene, only the conductance needed to be considered. The electrical conductivity was deduced from the conductance spectrum, $\log(\sigma')$ versus $\log(f)$; the frequency f is given in Hertz, σ' in Siemens per meter (Fig. 10.2). The conductance spectrum ideally consists of four regions: polarisation at low frequencies, the low frequency- or DC-plateau, the frequency dispersive region at higher frequencies, and the high frequency plateau at even higher frequencies. If no polarisation would occur at the interface between the sample and the electrodes, the DC-plateau would extend to zero frequency, corresponding to continuous voltage. The polarisation at the electrode-sample interface is expressed in a decrease of $\log(\sigma')$ towards the low frequencies. This region extends the further with increasing temperature. The DC-plateau is the frequency domain of interest for this study. The level of the "DC-conductance"

10. Impedance spectroscopy

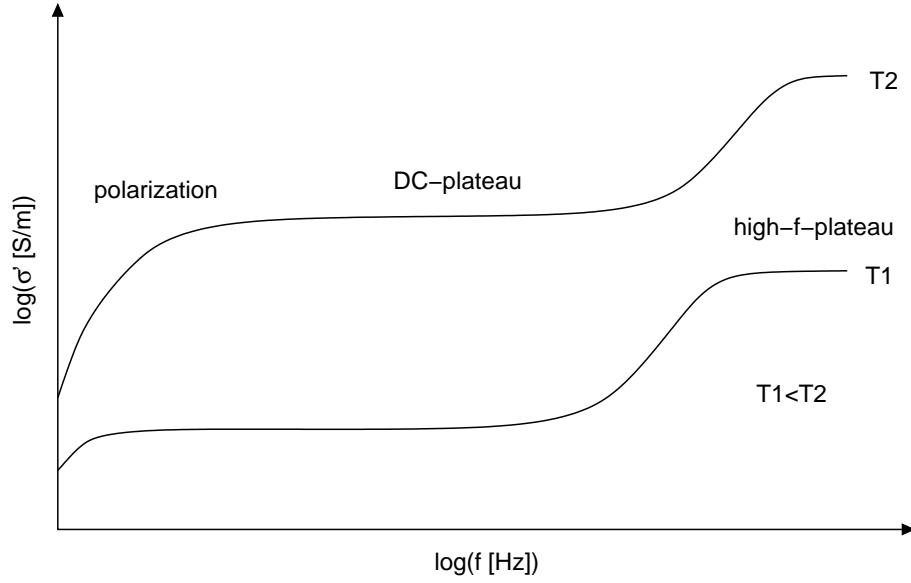


Figure 10.2.: Schematic conductance spectra. f is the frequency, T is arbitrary temperature.

is the sum of the contributions of all mobile charge carriers to the electrical conduction.

$$\sigma = \sum_i \sigma_{i^+} + \sigma_{e^-} \quad (10.7)$$

where the sum is taken over all cations i^+ , e^- denotes electrons. The oxygen anions in silicates are very immobile due to their large atomic radius compared to the cations and are therefore assumed to not contribute to electrical conduction.

The frequency dispersive region and the high frequency plateau also arise from movement of the charge carriers, but the higher the frequency, the more thermal atomic oscillations around their equilibrium position contribute to the signal. If the frequency approaches the Debye frequency, i.e., the maximum vibrational frequency of the crystal lattice at a given temperature, the spectrum again flattens out to the high frequency plateau, where all oscillatory movements of charged particles contribute to the conductance. The high frequency plateau was never observed in this study, because it appears very

rarely below 10^6 Hz. The kinetic energy of the atoms increases with increasing temperature, and hence the frequency of successful jumps of charge carriers to an adjacent new equilibrium position increases. Therefore, the DC-plateau extends to higher frequencies with increasing temperature. Due to the increasing mobility of charge carriers with temperature, the level of the DC-plateau then also increases, i.e., the whole impedance spectrum shifts towards the upper right.

11. Experimental setup

Electrical conductivity was measured by applying an alternating voltage with an amplitude of 1.5 V to the samples via two platinum electrodes. The electrodes were made of platinum conductor paste (OS2, Heraeus), which was heated for 5 minutes at 500°C and subsequently for another 5 minutes at 850°C in air. The platinum paste reduced to a nearly pure platinum film with good adhesion to the polished crystal surfaces.

The measurements were carried out at ambient pressure in the temperature range 700 to 1040°C. Hydrogen loss due to heating was minimized by flushing the furnace with a continuous flow of either argon with 7% H₂ or with pure H₂. The flushing also established a "clean" atmosphere by replacing the air in the furnace. Samples containing deuterium were exposed to pure H₂ gas, to derive H/D-exchange diffusion coefficients from the H/D-concentration profiles measured with FTIR-spectroscopy after the experiments. The results of the diffusion experiments are described in Chapter 7.

The oxygen fugacity was measured with an Yttrium doped ZrO₂-ceramic cell. The dopant caused oxygen vacancies, leading to enhanced oxygen mobility in the ceramic. One end of the ZrO₂-ceramic-piece was exposed to the furnace atmosphere and the other end was exposed to the surrounding air. The difference in oxygen fugacity caused a voltage U between both ends proportional to the difference in oxygen fugacity:

$$U = \frac{RT}{z_e F} \ln \left(\frac{p_{O_2}'}{p_{O_2}''} \right) \quad (11.1)$$

The voltage U was measured with two platinum wires brought into contact with one end each. Temperature T was measured with an S-type thermocouple near

11. Experimental setup

the sensor ceramic. R is the gas constant, F the Faraday's constant, $p_{O_2'}$ the oxygen fugacity in the furnace, and $p_{O_2''}$ the reference oxygen fugacity, in our case air. z_e is the number of electrons transferred per mole, here $z_e=4$ because $O_2 + 4e^- = 2O^{2-}$. Oxygen fugacities, calculated with Equation 11.1, were in the range of $\log(p_{O_2})=-55$ to -130 , i.e., the air was nearly completely replaced by the ArH_2 - or H_2 -gas flow. Stable values were reached within minutes.

For automated impedance analyses, a modular system from Novocontrol was used. The Alpha-A9 mainframe provided basic functionality of signal generation and analysis. The mainframe was combined with a ZG4 test interface which enabled impedance measurements with our self-made sample holders in four wire mode, among a variety of other measurement configurations. In four wire mode, two cables were used for current and voltage each. With only two electrodes used, the four wire mode was not essential, but provided the best possible accuracy. The measurement system was controlled with the software WinDETA (Novocontrol), which allowed automated data acquisition, online graphical data preview and ASCII-file data export. The impedance range was 10^{-2} to $10^{14} \Omega$ in the frequency range $3 \mu\text{Hz}$ to 20 MHz .

In order to reduce the rate of failed measurements, the design of the sample holder was changed at some point. A number of successful measurements were done with the first sample holder (upper picture in Figure 11.2), but due to the low signal of the small samples with electrode areas around 0.2 mm^2 , a possible contribution of the alumina ceramics to the measured conductance had to be considered. The first sample holder was constructed of one alumina ceramics tube with six capillaries for the leading wires, so a current between the leading wires could not be excluded. In the second sample cell, the Pt-leading wires were hosted in two spatially separated ceramic tubings, similar to the one described by [Özkan and Moulson \(1970\)](#), avoiding an electrical current between wires of different potential through the ceramics (lower picture in Figure 11.2).

The samples were either clamped directly between the faces of two truncated

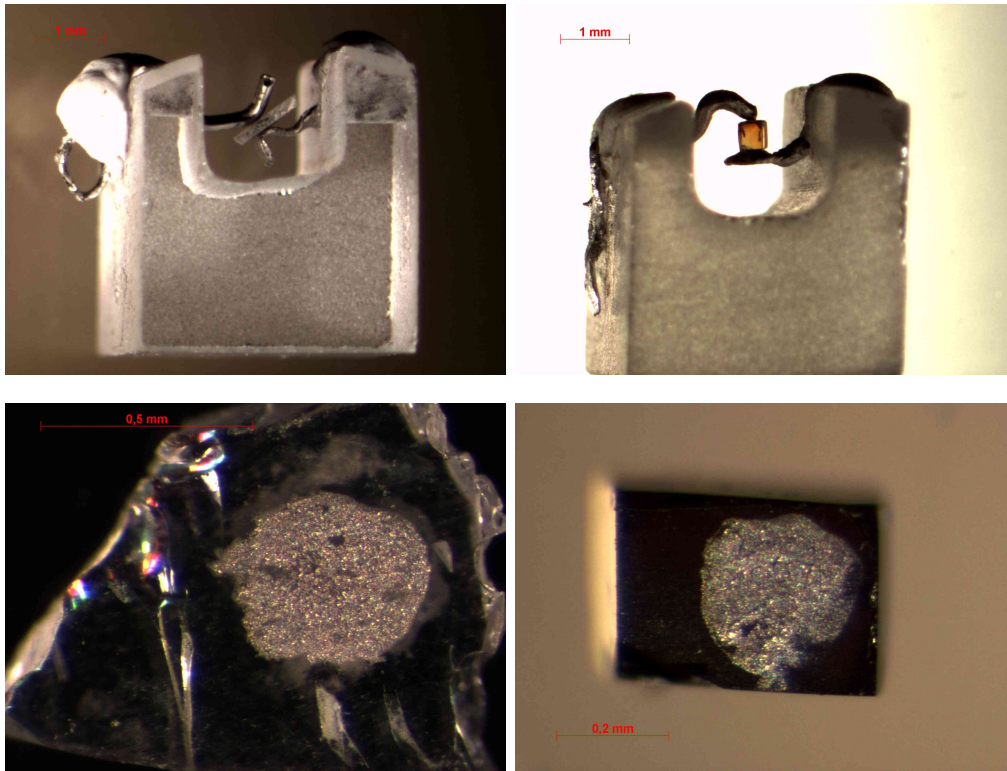


Figure 11.1.: Photomicrographs of two samples (es27-3 left, es9-3 right), showing the Pt-paste electrodes and the fixation between two Pt-wires in an sapphire single-crystal. The cube shaped sample was measured $\parallel[100]$ and $\parallel[001]$, the measurement $\parallel[010]$ failed due to poor electrical contact.

11. Experimental setup

cones made of Pt₉₀Rh₁₀-alloy, or they were fixed in an additional inset between two Pt-wires (Fig. 11.1). All measurements with the first sample cell were done without the inset, all but two of the measurements with the second sample cell were done with the inset. The inset was made of a sapphire single-crystal and its surface was kept clean to avoid accumulation of carbon or iron at reducing conditions and at high temperatures. Hydrocarbon compounds were removed by heating the inset in air. A coating of iron oxide on the surface was sometimes observed after heating. The iron oxide was removed by dipping the contaminated parts in concentrated HCl, so no contribution to the measured electrical conductivity was expected to originate from the inset.

The purpose of the inset was to minimize the risk of surface conduction as the samples used in this study were much smaller than commonly used for impedance spectroscopic measurements. The faces of the truncated cones were larger than the sample faces, which could facilitate conduction across the edges of the crystal plates. Reproducible electrical conductivities of chemically equal samples, but differing in size and geometry, suggest conduction through the bulk samples, rather than along the surface. Sample es16-4a was measured twice with different electrodes of the same area, but at different locations on the sample. In one case, the electrodes lay directly in the middle of the sample, in the other case, the electrodes were located near the edge. Furthermore, one measurement was done without the inset. The results are in excellent agreement, therefore surface conduction can be ruled out (Fig. 12.3).

Nevertheless, some measurements with exceptionally high or low electrical conductivities were neglected. Very low values were always accompanied by noisy spectra and could therefore be attributed to poor electrical contacts, e.g., between the Pt-electrodes and the wires of the sapphire inset. Very high electrical conductivities were caused by bypass or leakage currents. In cases where the Pt-paste was not applied carefully, the current could bypass the sample leading to too high conductivities. Another example is the abovementioned carbon or iron accumulation on sample edges or on the alumina inset. Further-

more, air turned out to be more conductive than the samples, so measurements in air were neglected.

The temperature was continuously monitored with an S-type thermocouple (Pt₉₀Rh₁₀-Pt₁₀₀). In earlier experiments, the temperature was recorded manually at the start, at several frequencies of the DC-plateau, and at the end of every spectrum acquisition. In later experiments, the temperature was recorded automatically every 10 to 30 seconds. The sample cell was not inserted in the furnace before a stable starting temperature, usually 750°C, was established. Heating of the sample was therefore very fast and took just 5-10 minutes. Immediately after the sample cell was pushed inside, the ArH₂-gas valve was opened. In most cases, the gas flow was switched to hydrogen gas after about three minutes. To terminate the experiment, the gas flow was again switched to ArH₂ gas mixture for about three minutes before the sample cell was pulled out of the furnace. The sample cooled down to temperatures below 500°C in less than two minutes.

Since electrical conductivity depends on the thickness of the sample and on the area of the electrodes, both needed to be determined before or after the experiment. The sample thickness was measured with a Mitutoyo micrometer with an accuracy of $\pm 2 \mu\text{m}$. The area of the Pt-spot was measured from photomicrographs with the software Adobe Photoshop. Photos of both sides of the sample were superimposed, so the overlapping area of the Pt-spots — the effective electrode area — could be determined. Due to the irregular shape of the Pt-spots, the effective area could differ significantly from the area of each single spot.

11. Experimental setup

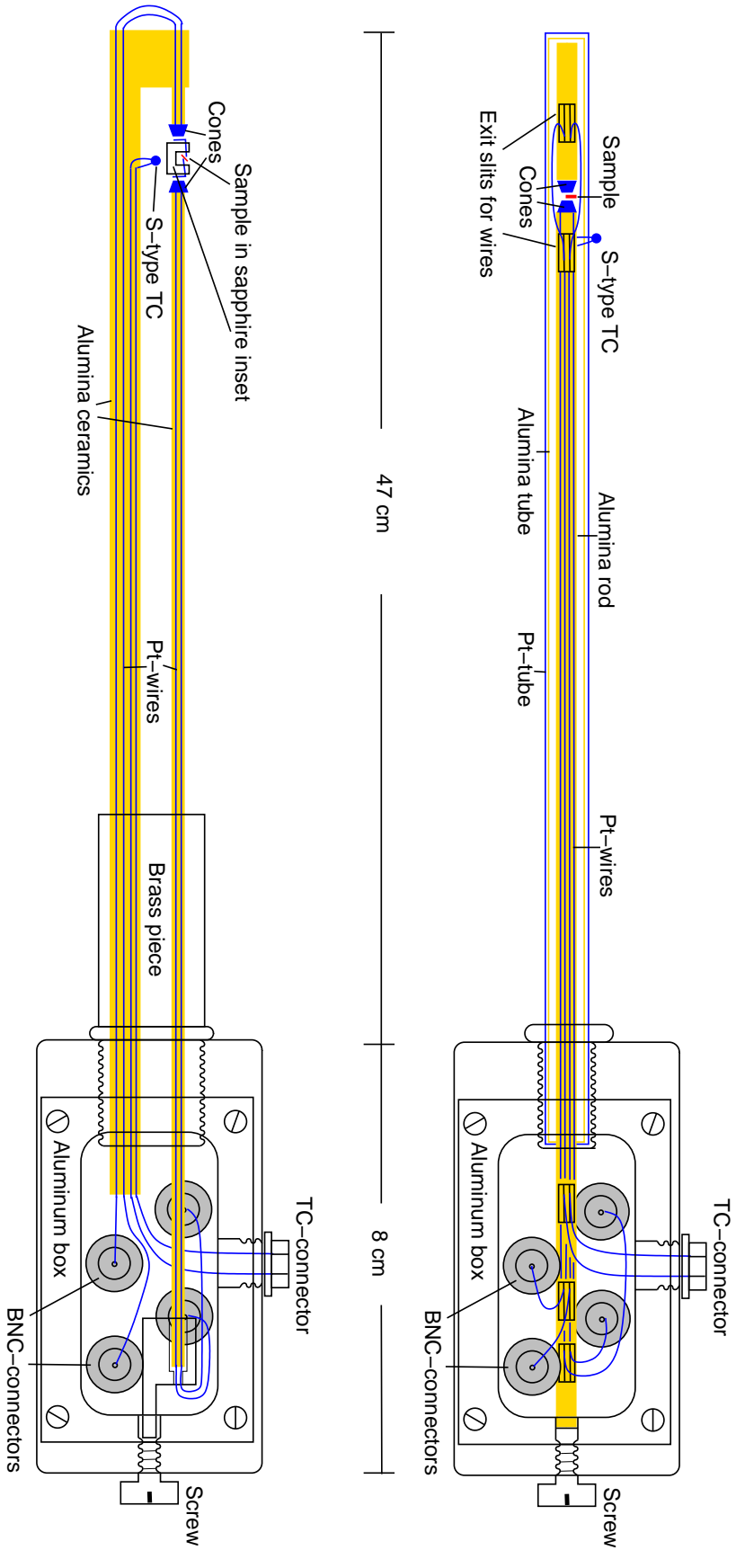


Figure 11.2.: Sample cells for electrical conductivity measurements. All yellow parts are made of alumina ceramics, all blue parts are either made of Pt or $\text{Pt}_{90}\text{Rh}_{10}$, TC denotes thermocouple. In the aluminium box the Pt-wires were connected via connector pins and thin, insulated copper wires to the BNC-connectors. These connections are not shown in the pictures for clarity reasons. The upper one is the first design with one ceramic rod hosting all six Pt-wires. The lower figure shows the new design with two separated ceramic rods.

12. Results

In the log-log representation of an electrical conductivity spectrum, the higher-frequency domain is attributed to charge transport through the sample, the lower-frequency domain reflects trapping of ions and polarisation mechanisms at the interface between the electrode and the crystal. Depending on temperature and quality of the electrodes, the polarisation region could significantly overlap with the DC-plateau, complicating identification of the level of the plateau (upper Figure 12.1). A comparison with the impedance in the complex representation helps to distinguish both frequency domains as they usually appear as two distinct features in the complex impedance plot (Fig. 12.2): the impedance of the bulk sample is represented by the semicircle, whereas the electrode-sample interface contribution gives the adjacent "tail". In the complex impedance plot, the frequency increases from right to left, opposing the x-axis, so the "tail" is at low frequencies. The electrical conductivity of the sample equals the inverse diameter of the impedance arc. The frequency at the vertex of the semicircle is the inverse relaxation time of the conduction-process.

Activation energies of electrical conductivity range from 133 to 290 kJ/mol; the natural mantle orthopyroxenes having the lowest and pure enstatite the highest activation energy. In some measurements, the activation energy changes with temperature. The slope in the arrhenius plot either increases (es4-4, es16-4a) or decreases (br1-2a, es7-8). The increase can be explained by a change of the dominating charge transport mechanism, as discussed in detail in Part III. A decreasing slope can not be explained in terms of transport processes, but is related to degeneration of electrodes and alteration of samples. A time-dependent increasing influence of polarisation effects at the sample electrode

12. Results

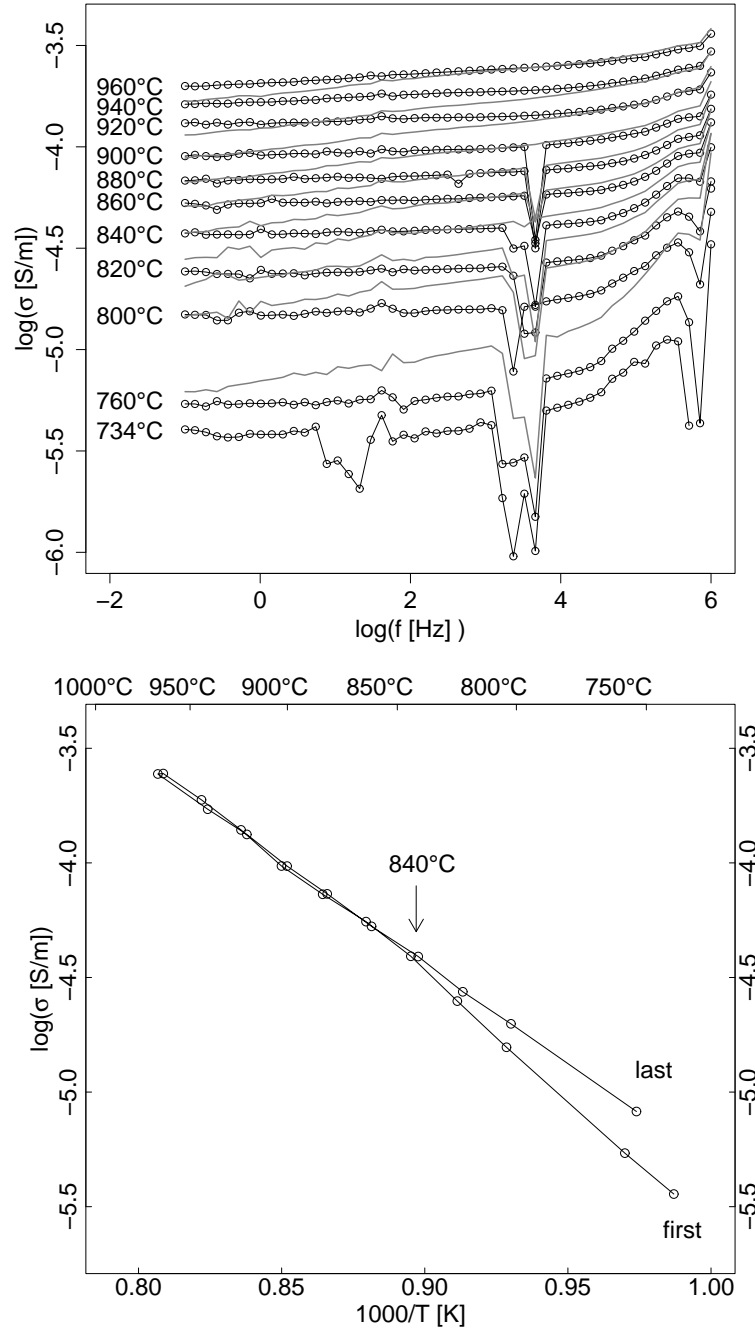


Figure 12.1.: Conductivity spectra and corresponding arrhenius plot of sample es7-8. Black spectra with datapoints indicate measurements during heating and grey spectra with omitted datapoints were measured during cooling at the same temperatures. The increasing downward slope of the spectra is caused by an increasing influence of polarisation, probably degeneration of the electrodes.

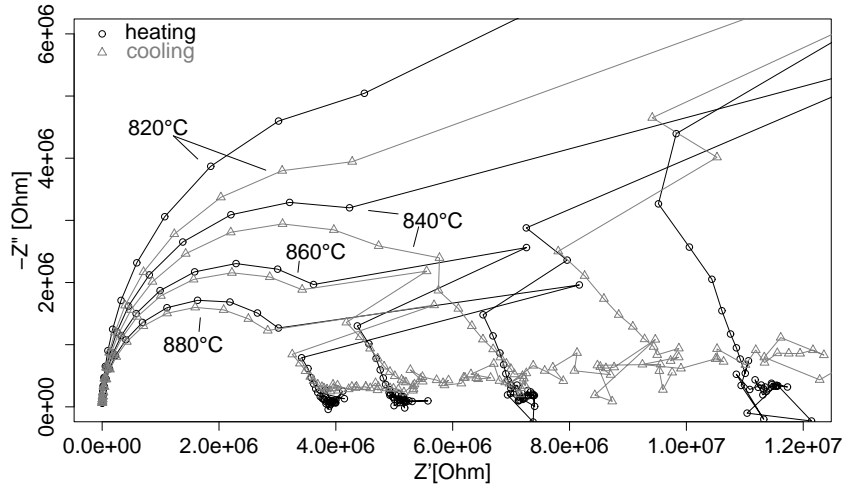


Figure 12.2.: Complex impedance plots of selected measurements of sample es7-8. Increasing influence of the electrode-sample interface is expressed in the low frequency feature (right of the semicircles). In addition, the semicircles get increasingly flattened and elongated to the left, as if the semicircle splitted up into two overlapping semicircles.

interface is expressed in a growing low-frequency feature adjacent to the high-frequency impedance arc. Formation of cracks in the sample due to heating, cooling, or dehydration may cause the same effect. Measurements with significant polarisation effect are often also rather noisy, indicating poor electrical contact between the sample and the electrodes. For this reason, several measurements have been rejected.

The electrical conductivity result of sample es7-8 (6 wt% Al_2O_3) is an example for increasing polarisation. Activation energy of this sample decreases at 840°C upon heating from 225 to 186 kJ/mol and remains constant upon cooling (lower Figure 12.1). With time, the high-frequency impedance arc becomes more flat and elongated to the right, probably due to the development of a second, overlapping arc (Fig. 12.2). The second arc indicates a second relaxation process with a similar relaxation time. Although no inhomogeneities were found with the microscope or with SEM, such as exsolution of talc or of

12. Results

an Al-rich phase, alteration of the sample cannot be excluded. Consequently, the first five measurements, having the higher activation energy, more reliably represent electrical conductivity of aluminous enstatite than the later measurements and the lower activation energy.

The decrease of activation energy of br1-2a happens at similar temperatures as the one of es7-8 (Fig. 15.3, right). The change in slope is smooth between 840 and 860°C. Exsolution of an Al-rich phase is unlikely, because br1-2a contains only 0.21 wt% Al_2O_3 . However, FTIR-spectra of this sample reveal a strong OH-stretching vibration band of talc at 3674 cm^{-1} and fine lamellae could be observed microscopically in the crystal (Appendix C.1). The complex impedance arc of this sample shows a slight elongation to the right after several minutes of tempering, similar to sample es7-8. Moreover, the activation energies of both samples are similar (Tab. 12.2).

Many samples show a hysteresis with heating and cooling branches in the Arrhenius plot having different slopes. In some cases this is probably an effect of the abovementioned degeneration of electrodes and alteration of samples. Sometimes, the hysteresis suddenly occurs when the temperature is lowered. In this case, also mechanical stress and loosening of fragile electrical contacts, e.g., between wires and Pt-paste, could influence the measurements. In some cases, a decrease in electrical conductivity can be attributed to a superimposed decrease in charge carrier concentration with time.

The electrical conductivity of pure enstatite sample es27-3 was measured in three experiments. Although electrical conductivity did not increase during the experiments, it increased from experiment to experiment. Figure C.4 illustrates the change in electrical conductivity. After each experiment, the sample was analysed with FTIR-spectroscopy and heated in air for 10 minutes at 400°C for fixation in the sample cell. Since it is unlikely, that the sample was altered during the heating, the cause of the increase remains unclear. The first experiment lasted 3:30 hours at 905°C in ArH_2 -gas flow. Neither the H_2O -content nor electrical conductivity changed during this time. In the second

experiment, the peak temperature of 861°C was held constant for 16 hours in H₂-gas flow and electrical conductivity and hydrogen content did not change either. In order to observe the effect of dehydration on electrical conductivity, the third experiment was carried out in air, without a gas-flow. Five minutes before each measurement was started, the ArH₂-gas flow valve was opened and shut immediately after the measurement was finished. Conductivity measurements in ambient atmosphere yielded much too high values, probably due to conducting contaminants in the air.

In the Arrhenius plot, the first one or two datapoints at the lowest temperatures often have a lower slope than the later datapoints. This can be attributed to moisture on surfaces and a large error in temperature measurement due to fast heating during the first minutes. A stable temperature and atmosphere was established in the furnace before inserting the sample. Therefore, the sample cell was heated from room temperature to about 700°C during the first minutes.

Most electrical conductivity results of this study cluster in a narrow region (Fig. 12.3). Only the samples oriented $||[001]$ and the three most iron-rich samples exhibit higher conductivities. No systematic anisotropy between $[100]$ and $[010]$ could be revealed. The anisotropy pattern of electrical conductivity of orthopyroxene therefore is $[001] > [010] \approx [100]$. In contrast to earlier studies on olivine and orthopyroxene (e.g. Wang et al. (2006), Yoshino et al. (2009), Dai and Karato (2009a)), the electrical conductivity does not show a clear correlation to hydrogen concentration. The enhancement of electrical conductivity through doping with aluminium, as observed by Duba et al. (1979), is also not supported by the results. Some aluminous enstatites have approximately the same electrical conductivity as pure enstatite, others exhibit slightly higher electrical conductivities. If the iron concentration exceeds a threshold of about 5 wt% FeO total iron, it has an enhancing effect on electrical conductivity of orthopyroxene due to polaron conduction. The contribution of polarons to electrical conductivity is discussed in detail on the basis of model calculations

12. Results

in Part III.

The variation of electrical conductivity with oxygen fugacity (Stocker, 1978) was not investigated in this study, but the influence of variations in experimental oxygen fugacity on the results needs to be discussed briefly. As already mentioned, $\log(f_{O_2} \text{ [bar]})$ varied between -55 to -130 at 700-1200°C. Oxygen fugacity during syntheses of orthopyroxene is not exactly known, but was several orders of magnitude higher than during the electrical conductivity experiments. Oxygen fugacity during syntheses of iron-bearing orthopyroxenes was probably buffered by the ferrosilite-hematite-quartz system (Stalder, 2004), and oxygen fugacity during iron-free orthopyroxene-syntheses was estimated by Stalder et al. (2005) as to be buffered by the cell assembly, therefore being constrained by the C-CO-CO₂-O₂ system. It can not be excluded that the samples at least partially equilibrated to the lower oxygen fugacity during the conductivity measurements. The dependence of electrical conductivity on oxygen fugacity in multiply doped orthopyroxenes is not known, but according to the point defect models by Stocker (1978), the concentration of cationic vacancies and electronic defects should decrease in general with decreasing oxygen fugacity. Therefore, we would expect electrical conductivity to decrease with time upon equilibration of samples during the experiments. A decreasing oxygen fugacity was observed in two iron-free samples but was attributed to hydrogen loss (Chapter 15). The change in charge carrier concentration should affect the iron-bearing samples even more because of the reduction of mobile electronic defects, but no other sample showed a superimposed continuous decrease of electrical conductivity. The effect of oxygen fugacity on the electrical conductivities determined in this study can be considered as negligible.

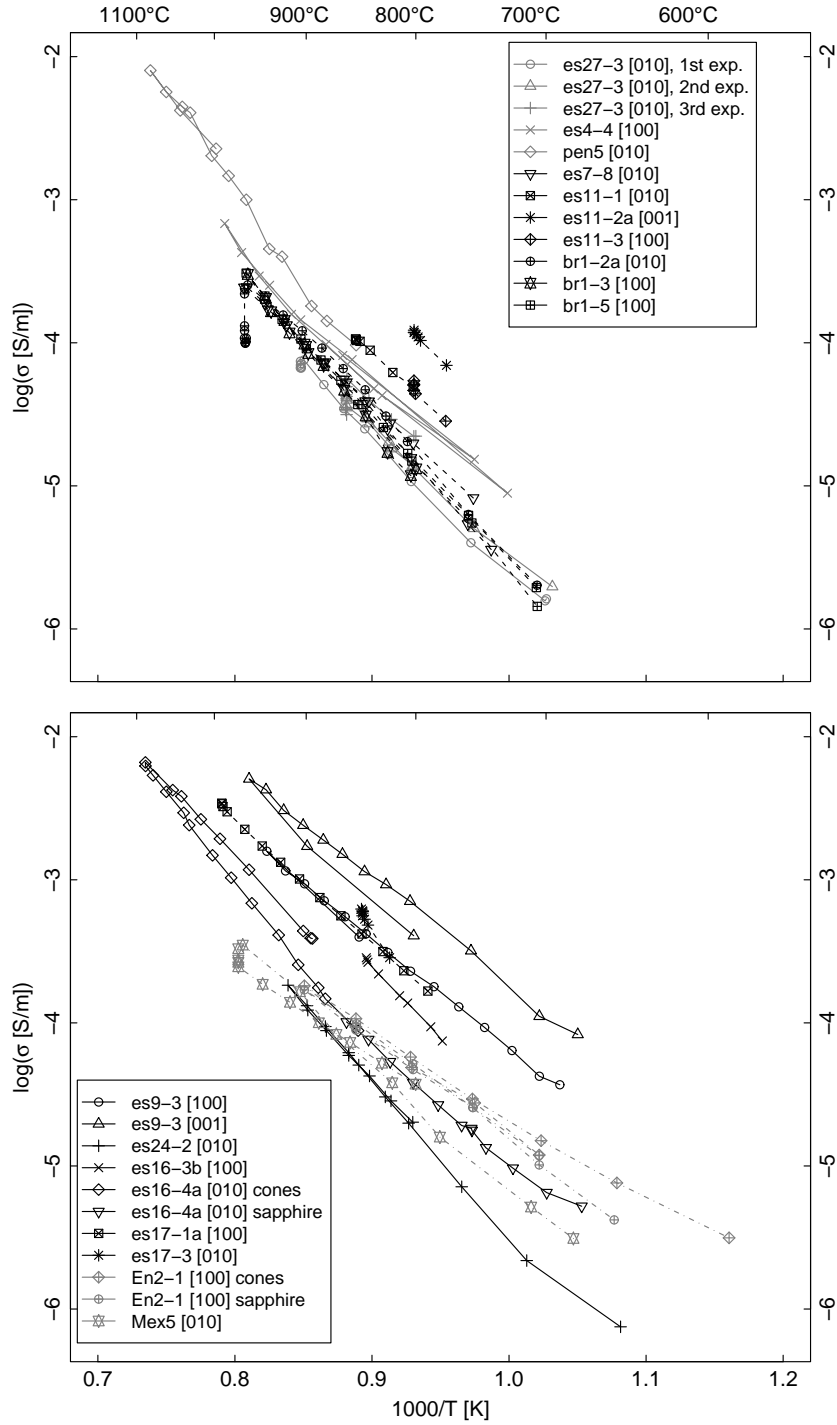


Figure 12.3.: Electrical conductivity (σ) of synthetic and two mantle orthopyroxenes. Upper figure: grey color indicates pure enstatite, black enstatite with 0.1-6 wt% Al_2O_3 . Lower figure: black indicates synthetic orthopyroxenes with 0.1-1.4 wt% Al_2O_3 and 2-12 wt% FeO , and grey natural orthopyroxenes with 6 wt% FeO and 0.1 and 6 wt% Al_2O_3 . Sample names and crystallographical orientations are given in the legends. Details on the samples are given in Tabs. 12.1, 12.2.

Table 12.1.: Chemical composition of samples used for impedance spectroscopy. Standard deviations of EMPA-data are given in parentheses.

Sample	SiO ₂	MgO	Al ₂ O ₃	FeO	TiO ₂	MnO	CaO	Na ₂ O
es27-3	60.23(0.23)	38.87(0.14)	0.03(0.02)	0.03(0.02)	0.00	0.00	0.01(0.01)	0.00
es4-4	— n.a. —							
pen5	— n.a. —							
es7-8	56.06(0.54)	35.71(0.35)	6.02(0.82)	0.03(0.03)	0.00	0.00	0.00	0.00
es11-3	57.25(1.61)	36.19(2.22)	1.76(0.30)	0.00	0.00	0.00	0.00	0.00
es11-2a	59.19(0.20)	37.42(0.27)	1.99(0.08)	0.00	0.00	0.00	0.00	0.00
es11-1	58.43(0.73)	39.20(0.58)	3.65(1.26)	0.00	0.00	0.00	0.02(0.02)	0.00
br1-5	59.61(0.55)	38.03(0.27)	0.09(0.01)	0.00	0.00	0.00	0.04(0.04)	0.00
br1-3	59.85(0.35)	37.93(0.36)	0.10(0.02)	0.03(0.03)	0.00	0.00	0.00	0.00
br1-2a	60.33(0.44)	38.84(0.28)	0.21(0.05)	0.00	0.00	0.00	0.00	0.00
es17-1a	57.55(0.89)	33.24(2.08)	0.07(0.05)	10.23(2.80)	0.00	0.00	0.03(0.02)	0.00
es17-3	— n.a. —							
es9-3	56.79(2.24)	33.62(2.51)	0.43(0.13)	4.72(0.81)	0.00	0.00	0.00	0.00
es24-2	58.82(0.23)	36.32(0.25)	0.44(0.04)	1.99(0.13)	0.00	0.00	0.00	0.00
es16-3b	58.04(0.41)	36.59(0.31)	0.51(0.05)	1.70(0.14)	0.00	0.02(0.02)	0.00	0.00
es16-4a	57.93(0.32)	37.94(0.37)	1.39(0.39)	3.74(0.59)	0.00	0.00	0.02(0.01)	0.00
En2-1	58.31(0.39)	34.92(0.41)	0.15(0.02)	6.61(0.18)	0.04(0.01)	0.25(0.02)	0.17(0.03)	0.05(0.02)
Mex5	53.86(0.29)	30.91(0.11)	5.53(0.09)	6.95(0.12)	0.11(0.02)	0.15(0.07)	1.01(0.06)	0.11(0.02)

Table 12.2.: Experimental and sample characteristics. "b/a" are the measured H₂O- and D₂O-concentrations before/after the experiment. E_a is the activation energy according to equation $\sigma T = A \exp(-E_a/RT)$, log(A) is the intercept in the arrhenius plot log(σT) vs. 1000/T. "Or." is the crystallographical orientation of the sample. "1st" and "2nd" refer to the first sample cell and the second cell design, respectively. "Cones" means, the sample was clamped directly between the cones, "sapphire" indicates use of the sapphire inset.

Sample	Cell constant t/A [m ⁻¹]	b/a [ppm-wt]	Or.	Cell type	Gas	E _a [kJ/mol]	log(A) [K S/m]	comment
es27-3	1.75e-4/1.4e-7=1250	D ₂ O+H ₂ O 102+7/n.a.	(010)	sapphire/2nd	ArH ₂	209.9	8.25	complete H/D-exch.
	1.75e-4/1.4e-7=1250	H ₂ O n.a./159	(010)	sapphire/2nd	H ₂	195.6	7.67	2nd exp.
	1.75e-4/1.4e-7=1250	H ₂ O 159/50 ^a	(010)	sapphire/2nd	air/ArH ₂	167.7	6.94	3rd exp., dehydr.
es4-4	1.43e-4/2.0e-7=715	H ₂ O 227/165	(100)	cones/1st	H ₂	162.2/289.5	6.40/11.91	
pen5	1.90e-4/8.0e-8=2375	H ₂ O 0/0	(010)	cones/1st	H ₂	258.2	11.01	dry sample
es7-8	1.91e-4/7.0e-7=273	H ₂ O 1499/1464	(010)	sapphire/2nd	H ₂	186.1/224.8	7.37/9.14	
es11-3	1.70e-4/1.1e-7=1545	D ₂ O+H ₂ O 566+106/n.a.	(100)	sapphire/2nd	H ₂	n.a.	n.a.	H/D-exchange
es11-2a	2.20e-4/6.0e-8=3667	D ₂ O+H ₂ O 367+59/410+147 ^a	(001)	sapphire/2nd	H ₂	198.3	8.75	H/D-exchange
es11-1	1.80e-4/4.7e-7=383	D ₂ O+H ₂ O 1195+196/1106+199 ^a	(010)	cones/1st	H ₂	165.4	6.75	H/D-exchange, talc ^b
br1-5	2.60e-4/6.0e-8=4333	H ₂ O 242/234	(100)	sapphire/2nd	H ₂	226.1	9.09	
br1-3	2.23e-4/1.4e-7=1593	H ₂ O 207/n.a.	(100)	sapphire/2nd	H ₂	209.6	8.39	
br1-2a	2.32e-4/1.1e-07=2109	H ₂ O 272/185	(010)	sapphire/2nd	H ₂	167.5/212.2	6.59/8.60	talc ^{b,c}
es17-1a	3.05e-4/3.4e-7=897	H ₂ O 307/300	(100)	cones/1st	H ₂	175.8	7.87	
es17-3	3.50e-4/2.7e-7=1296	D ₂ O+H ₂ O 153+31/n.a.	(010)	cones/2nd	H ₂	n.a.	n.a.	amphibole ^c
es9-3	4.20e-4/7.0e-8=6000	H ₂ O 870/971	(100)	sapphire/2nd	H ₂	155.1	6.92	
	4.80e-4/1.0e-8=48000	H ₂ O 971/964	(001)	sapphire/2nd	H ₂	154.9	7.35	
es24-2	1.46e-4/8.0e-8=1825	H ₂ O 298/353	(010)	sapphire/2nd	H ₂	214.3	8.72	
es16-3b	1.93e-4/7.0e-8=2757	D ₂ O+H ₂ O 371+99/269+196 ^a	(100)	cones/1st	H ₂	203.6	9.02	H/D-exchange
es16-4a	1.12e-4/9.0e-8=1244	H ₂ O 0/277	(010)	cones/1st	H ₂	244.5	10.31	1st exp.
	1.12e-4/9.0e-8=1244	H ₂ O 277/n.a.	(010)	sapphire/2nd	ArH ₂	177.1	7.24	2nd exp.
En2-1	3.50e-4/4.9e-6=71	H ₂ O 12/n.a.	(100)	cones/2nd	ArH ₂	133.4	5.24	natural opx, 1st exp.
	3.50e-4/4.45e-6=79	H ₂ O n.a./n.a.	(100)	sapphire/2nd	ArH ₂	141.0	5.59	2nd exp.
Mex5	2.80e-4/3.6e-7=778	H ₂ O 141/52	(010)	sapphire/2nd	ArH ₂	173.3	6.90	natural opx

^aValues representing the middle of the diffusion profile across samples

^bThin lamellae microscopically visible

^cOH-Peak at 3674 cm⁻¹, or corresponding OD-peak at 2711 cm⁻¹ in the IR-spectrum indicates submicroscopic amphibole or talc inclusions.

13. Discussion

Due to the relatively high diffusivity of hydrogen, electrical conductivity is expected to depend strongly on the hydrogen concentration (Karato, 1990). The "dry" pure enstatite sample (pen5) and the Al-rich sample (es7-8) which contains more than 1500 ppm-wt H_2O , illustrate clearly that this is not the case for orthopyroxene in general. Both samples, as well as pure enstatite with only about 250 ppm-wt H_2O , have similar electrical conductivities (upper Fig. 12.3). A possible reason for this is the relatively low mobility of hydrogen incorporated in association with aluminium, as demonstrated by the diffusion experiments (Part I). Only the fraction of hydrogen incorporated as charge compensation for octahedral vacancies might contribute to electrical conduction. This fraction, as estimated from the corresponding OH-peaks in the IR-spectra, is approximately the same for all iron-free enstatites regardless of their aluminium content (200-350 ppm-wt H_2O). The high activation energy of the hydrogen-free pure enstatite (pen5) suggests ionic conduction via octahedral vacancies to be the dominating charge transport mechanisms in this sample. The fact that electrical conductivity of the "dry" pure enstatite is even higher than the one of hydrous pure enstatite (es27-3, es4-4) and the rather small effect of dehydration on electrical conductivity, as discussed in Chapter 15, suggest that protons and deuterons are not in general the major charge carriers in the orthopyroxene samples of this study. Ionic conduction via octahedral vacancies probably gives a substantial contribution to electrical conductivity, in particular at temperatures higher than $\sim 900^\circ\text{C}$. In iron-bearing orthopyroxenes, hydrogen associated with ferric iron can be replaced by electron holes having the same mobility as the protons. Electri-

13. Discussion

cal conductivity of the iron-bearing samples is therefore insensitive to changes in hydrogen content (es16-4a, see Section 15.3). The model calculations revealed that polarons originating from ferric iron are the dominating charge carriers in most iron-bearing samples, because their concentration is usually much higher than the hydrogen concentration. It can be concluded that electrical conductivity can not directly be correlated to hydrogen concentration in orthopyroxenes, as the mobility of protons is governed by the mobility of the associated point defects. The concentration and mobility of anhydrous point defects might also equal or exceed that of hydrogen related point defects. Consequently, anhydrous point defects, such as octahedral vacancies and polarons, often provide substantial contributions to electrical conduction, and the influence of protons on electrical conductivity is the smaller the larger the contribution of anhydrous point defects.

13.1. Comparison with earlier studies

Several studies on electrical conductivity of orthopyroxene exist with disperse results (e.g. Duba et al. (1976, 1979); Will et al. (1979); Voigt et al. (1979); Xu and Shankland (1999); Dai and Karato (2009a)). The differences have been attributed to differing experimental conditions, such as oxygen fugacity or silica activity (Huebner and Voigt, 1988). Most data of this study also disagree with the earlier studies on orthopyroxene. Although the data agree roughly, most activation energies of this study are higher than the ones of earlier measurements (Fig. 13.1).

In contrast to the majority of samples used in this study, earlier studies used natural crystals, except for Will et al. (1979) and Voigt et al. (1979), who both used synthetic, polycrystalline orthopyroxene. Besides some minor elements, the natural samples contain higher amounts of Al_2O_3 and FeO than the synthetic samples of this study. Figure 13.2 illustrates that only the two natural samples of this study agree with some of the recent studies on electrical

13.1. Comparison with earlier studies

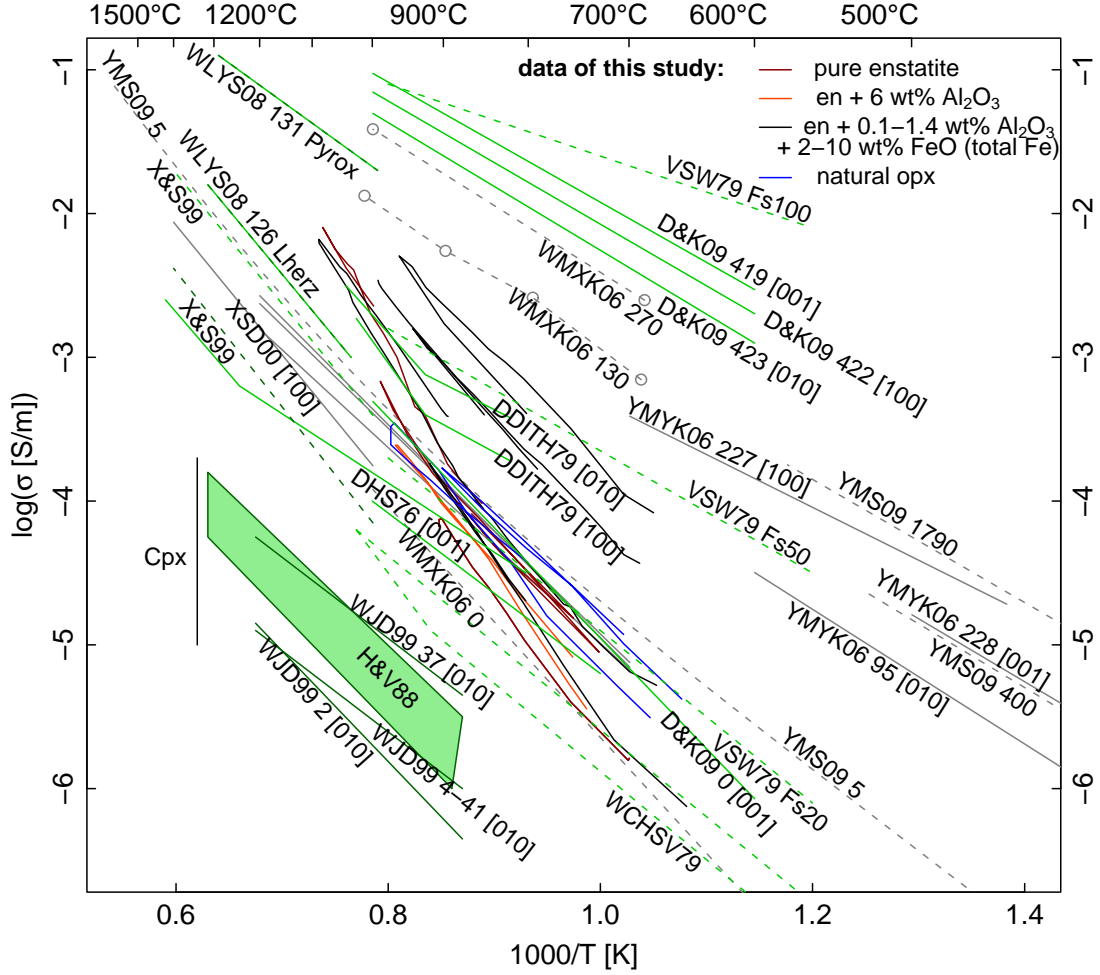


Figure 13.1.: Compilation of results of this study and of previous studies on electrical conductivity of olivine (grey), orthopyroxene (lightgreen) and clinopyroxene (diopside, darkgreen and green tetragon, indicated with "Cpx"). Solid lines denote single crystal measurements and broken lines indicate polycrystalline samples. Crystallographic orientations of the single crystals are given in square brackets. If applicable, water contents are given in ppm-wt H_2O after the authors initials and the year of the publication. DDITH79 (Duba et al., 1979), DHS76 (Duba et al., 1976), D&K09 (Dai and Karato, 2009a), H&V88 (Huebner and Voigt, 1988), VSW79 (Voigt et al., 1979) with Fs100/Fs50/Fs20 percentage of ferrosilite, WCHSV79 (Will et al., 1979), WJD99 (Wang et al., 1999), WLYS08 (Wang et al., 2008), WMXK06 (Wang et al., 2006), XSD00 (Xu et al., 2000), X&S99 (Xu and Shankland, 1999), YMYK06 (Yoshino et al., 2006), YMS09 (Yoshino et al., 2009). Further informations on these publications are listed in Table 13.1.

13. Discussion

conductivity of "dry" or hydrogen-poor orthopyroxene. In addition, electrical conductivity of olivine with few or no hydrogen also agrees with some results of this study.

Since electrical conductivities of En2-1 and Mex5 are probably dominated by polaron conduction, the interpretation of [Xu and Shankland \(1999\)](#) and [Dai and Karato \(2009a\)](#) is supported, who suggested the same for their anhydrous orthopyroxene samples. The activation energy of the "dry" sample from [Dai and Karato \(2009a\)](#), 147 ± 6 kJ/mol $\parallel[001]$, is comparable not only to the natural samples, but also to the synthetic iron and aluminium bearing sample es9-3, which has an activation energy of 155 kJ/mol $\parallel[100]$ and $\parallel[001]$ (Fig. 13.2). But electrical conductivity of es9-3 $\parallel[001]$ is more than one log unit higher, although the iron contents of this sample is about half that from [Dai and Karato \(2009a\)](#). The difference is either caused by the difference in experimental pressure (8 GPa vs. ambient pressure), or by differing charge carrier concentrations. The higher electrical conductivity of es9-3 could be explained by higher contents of hydrogen and ferric iron. The sample measured by [Xu and Shankland \(1999\)](#) is chemically very similar to Mex5 of this study and electrical conductivities of both samples are in good agreement. Both have an activation energy of 174 kJ/mol, even though [Xu and Shankland \(1999\)](#) measured a polycrystalline sample at 5 GPa. Hence, pressure has probably only a minor influence on electrical conduction through the bulk crystal, as already stated for olivine by [Xu et al. \(2000\)](#).

Apart from these agreements, an increase of electrical conductivity of several log units due to hydrogen, as reported by ([Dai and Karato, 2009a](#)), was not observed in this study. The increase in hydrogen content of olivine, as observed by [Wang et al. \(2006\)](#), is possibly caused by the presence of an aqueous fluid during the high pressure experiments. The authors report the subtraction of a substantial amount of OH-absorbance in the IR-spectrum after the experiment, designated as grain boundary water (as illustrated in the supplementary figure of the publication). In [Dai and Karato \(2009a\)](#) there is no indication on a

13.1. Comparison with earlier studies

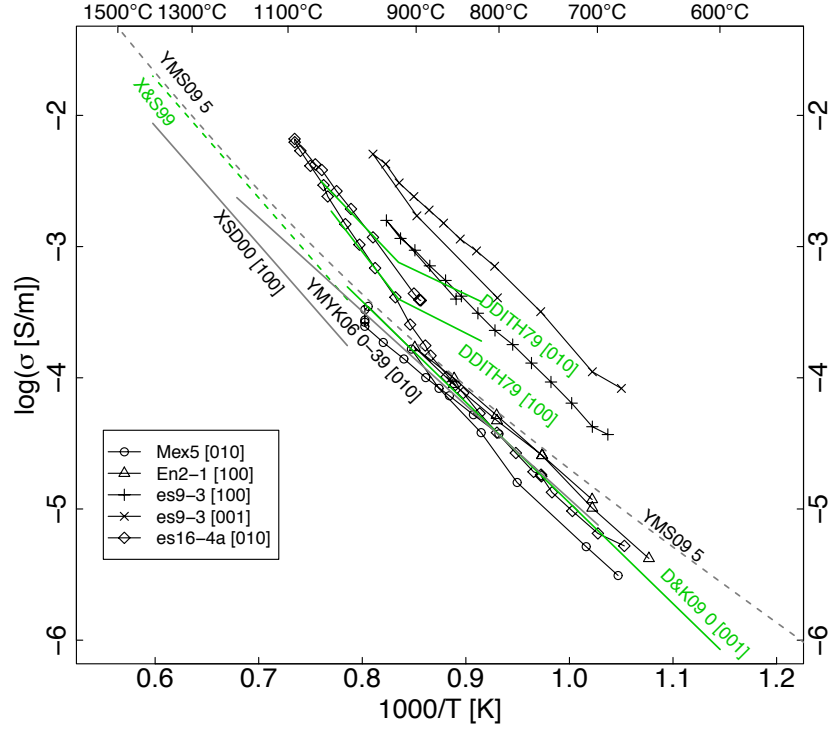


Figure 13.2.: Selection of data from Fig. 13.1, showing the agreement of earlier studies with data of this study. Note that electrical conductivity of olivine (grey) is very similar to electrical conductivity of orthopyroxene (green and black), and that the olivine-sample from YMYK06 gains 39 ppm-wt of H_2O during the experiment. Annotations: DDITH79 (Duba et al., 1979), D&K09 (Dai and Karato, 2009a), XSD00 (Xu et al., 2000), X&S99 (Xu and Shankland, 1999), YMS09 (Yoshino et al., 2009), YMYK06 (Yoshino et al., 2006).

13. Discussion

change in hydrogen content during the high pressure experiments, but the enhancement of electrical conductivity in the hydrous orthopyroxene samples is nearly identical to that observed by Wang et al. (2006). An increase in electrical conductivity with time together with a low activation energy as a consequence of dehydration and formation of aqueous fluid was observed and discussed by Yoshino et al. (2009). Although the problem of dehydration was avoided by relatively low experimental temperatures, Yoshino et al. (2009) found the electrical conductivity of hydrous olivine to be positively correlated with hydrogen content. In contrast to orthopyroxene, which can contain a variety of defect forming cations, olivine is rather "intolerant" to defect cations. For instance in San Carlos xenoliths, the mean total amount of defect-forming cations in olivine is ~ 0.6 wt% including Ca, Mn, and Ni. The mean total amount of defect cations in orthopyroxene is ~ 5.3 wt% including Ti, Al, Cr, Mn, Ca, Na (the given amounts in weight percent refer to the oxides of the given cations in Frey and Prinz (1978)). The concentration of point defects, and hence electrical conductivity in olivine is probably directly enhanced by the incorporation of hydrogen, whereas orthopyroxene has a larger concentration of anhydrous point defects, and the influence of hydrogen on the point defect chemistry is therefore less pronounced. Provided the electrical conductivity of Earth's upper mantle is influenced by proton conduction in the minerals, this implies that electrical conductivity is rather a measure for water content in olivine than in orthopyroxene.

13.2. Applicability of experimental results to electrical conductivity of Earth's upper mantle

The electrical conductivity of upper mantle rocks ranges from 10^{-3} to 10^0 S/m. At temperatures from 1000 to 1400°C, electrical conductivities of orthopyroxene and olivine agree with the lower range of conductivities in mantle rocks of

Table 13.1.: Summary of previous studies on electrical conductivity plotted in Fig. 13.1. In the comment, additional features are mentioned which may have affected electrical conductivity.

	Mineral	Sample form	P	T [°C]	f _{O₂}	Comment
Wang et al. (2008)	natural rocks: Dumite Lherzolite, Pyroxenite		2-3 GPa	1000-1300	Mo-MoO ₂	Pyroxenite + ~5% iron oxide
Wang et al. (2006)	olivine	polycrystalline synthetic	4 GPa	600-1000	Ni-NiO	+2% Opx
Xu et al. (2000)	olivine	polycrystalline synthetic	4 GPa	1000-1400	Mo-MoO ₂	100-800 ppm-wt H ₂ O +5% Opx
Yoshino et al. (2006)	olivine	single crystal natural	3 GPa	227-1227	Ni-NiO	0-228 ppm-wt H ₂ O
Yoshino et al. (2009)	olivine	polycrystalline synthetic	10 GPa	527-1727	Mo-MoO ₂	5-1790 ppm-wt% H ₂ O + Opx
Duba et al. (1979)	Opx	single crystal natural	0.1 MPa	820-1050	CO ₂ :CO=1.66:1	14 wt% FeO + 7 wt% Al ₂ O ₃ + 1 wt% Fe ₂ O ₃
Duba et al. (1976)	Opx	single crystal natural	0.1 MPa	727-1000	10 ^{-9.5} Pa @ 1000°C	10 wt% FeO
Dai and Karato (2009a)	Opx	single crystal natural	8 GPa	600-1200	Mo-MoO ₂	0 & ~420 ppm-wt H ₂ O 10 wt% FeO
Voigt et al. (1979)	Opx	polycrystalline synthetic	0.1-0.2 GPa	500-1000	QFI	
Will et al. (1979)	enstatite	polycrystalline synthetic	0.2 GPa	340-1100	not buffered	
Xu and Shankland (1999)	Opx	polycrystalline	5 GPa	1000-1400	IW	6 wt% FeO + 4 wt% Al ₂ O ₃
Xu and Shankland (1999)	Cpx	synthetic	13 GPa	1000-1400	IW	
Huebner and Voigt (1988)	diopside	single crystal natural	0.1 MPa	800-1300	10 ⁻⁴ -10 ⁻⁹ Pa @ 1000°C 10 ⁻³ -10 ⁻⁷ Pa @ 1200°C	
Wang et al. (1999)	diopside	single crystal natural	0.1 MPa	920-1200	~10 ⁻⁹ MPa	2, 4-41, 37 ppm-wt H ₂ O

13. Discussion

10^{-3} - 10^{-2} S/m. Highly conductive regions within the upper mantle were observed, for example, directly beneath the East Pacific spreading ridge (Baba et al., 2006), at ~ 200 km depth below the Northeast Pacific oceanic lithosphere (Lizzaralde et al., 1995), and at ~ 300 km and ~ 450 km below Superior Province of the Canadian shield, an Archean craton (Schultz et al., 1993). The high conductivities were interpreted either as a conductive phase at grain boundaries, e.g., partial melt (Roberts and Tyburczy, 1999; Gaillard et al., 2008; ten Grotenhuis et al., 2005), iron sulfide (Watson et al., 2010; Ducea and Park, 2000), carbon (Glover, 1996), or, based on the abovementioned recent high-pressure experiments, by proton conduction in olivine (Wang et al., 2006). However, at upper mantle temperatures, electrical conductivity of hydrous olivine is still too low as to explain the high mantle conductivities (Yoshino et al., 2009).

Some indications exist for the presence of partial melt in the upper mantle highly conductive regions. First, Green et al. (2010) found lherzolite to melt during breakdown of pargasite, suggesting the presence of partial melts at depth below 100 km under oceanic lithosphere. Secondly, incompatible elements in general get enriched not only in melt, but also at interfaces such as cracks and grain boundaries. Hiraga et al. (2003) reported enrichment of Ca, Al, Cr, and Ti, and a Mg-depletion in a 5 nm thick zone at the interfaces between olivine crystals in mantle dunite. A similar behaviour was observed for hydrogen (Sommer et al., 2008): OH-enrichment was measured with FTIR-spectroscopy at grain boundaries, cracks, and spinel inclusions. In nominally anhydrous minerals (NAMs) hydrogen is incompatible. Significant amounts of several 100 ppm-wt of H_2O in NAMs are in equilibrium with high environmental hydrogen fugacity. Consequently, hydrogen loss is a widely known phenomenon in nature (Demouchy et al., 2006; Peslier and Luhr, 2006) as well as in experiments including this study (Yoshino et al., 2006, 2009; Wang et al., 2006; Dai and Karato, 2009a), and might trigger partial melting in the upper mantle. Even though only a small portion of melt may be produced by dehy-

13.2. Applicability to Earth's upper mantle

dration, interconnectivity of the melt can be enhanced by shear strain, i.e., by mantle flow ([Hier-Majumder and Kohlstedt, 2006](#)).

The influence of conductive impurities at grain boundaries on the bulk electrical conductivity has already been experimentally investigated in several studies (see citations in the first paragraph of this section). In terms of application of laboratory data on magnetotelluric results, it has to be taken into account that laboratory electrical conductivity is usually inferred from the impedance in the kHz-frequency region, whereas magnetotelluric techniques use very much lower frequencies with periods of several seconds to days for measurements in the mantle. Laboratory measurements in the kHz-region detect movements of charged particles on the nanometer scale, i.e., much shorter than the grain size of samples. Hence, a conductive phase in a polycrystalline sample does not necessarily need to form an interconnected network to enhance electrical conductivity inferred from impedance spectroscopy, and consequently impedance spectroscopy is very sensitive to conductive impurities even if not equally distributed in the sample. This contrasts the dimensions involved in magnetotelluric measurements, in which a highly conductive grain boundary phase in the mantle needs to be interconnected on a much larger scale to significantly enhance electrical conductivity. Consequently, enhanced electrical conductivities observed in the laboratory due to small amounts of a conductive phase is not necessarily applicable to results of magnetotelluric measurements. An example is the electrical conductivity of San Carlos olivine containing 1 vol% of iron sulfide, an amount which is insufficient to be interconnected. Nevertheless, electrical conductivity is enhanced by more than one order of magnitude with respect to plain olivine ([Watson et al., 2010](#)). A second example is the study on natural rocks by [Wang et al. \(2008\)](#). Drill cores of xenolithic mantle rocks were used for electrical conductivity measurements at high pressure. Except for the pyroxenite, the results agree with presynthesized samples and single crystals. The pyroxenite contains 5 vol% of iron oxide which could have caused the high electrical conductivity (Fig. [13.1](#)).

13. Discussion

Grain boundaries enriched in incompatible elements as described by [Hiraga et al. \(2003, 2004\)](#) might also provide pathways of higher mobility for conductive impurity-caused point defects in mantle minerals. [Demouchy \(2010\)](#) reported grain-boundary diffusivity of hydrogen in olivine to be almost three orders of magnitude faster than volume diffusion through the bulk crystals. The higher mobility and concentration of hydrogen related point defects or other conductive defects at grain boundaries in mantle rocks could also be considered as a reason for high electrical conductivity in the upper mantle.

Another property of the upper mantle revealed by magnetotelluric measurements is lateral anisotropy of electrical conductivity. Anisotropic electrical conductivity at the base of the lithosphere was detected for example by [Bahr and Duba \(2000\)](#); [Leibecker et al. \(2002\)](#); [Gatzemeier and Moorkamp \(2005\)](#) below Germany, by [Bahr and Simpson \(2002\)](#) below the Fennoscandian plate, and by [Simpson \(2002\)](#) below the North Central craton of Australia. The electrical anisotropy conforms to the seismic anisotropy and it has been agreed by these authors that the electrical anisotropy is caused by mantle convection producing a shear-texture in the rocks of the upper mantle. [Simpson and Tommasi \(2005\)](#) tested the hypothesis with a theoretical model, which assumed that hydrous olivine and orthopyroxene get crystallographically aligned through shear strain. This lattice preferred orientation (LPO) might cause a macroscopic electrical anisotropy because hydrogen diffusivity, and hence proton conduction, is anisotropic along the three crystallographic axes in both minerals, in particular in hydrous olivine. However, it was concluded that the observed electrical anisotropy cannot be fully explained by the anisotropic electrical conductivity of hydrous olivine and therefore other conduction mechanisms such as conduction at grain boundaries and macroscopic inhomogeneities, must also contribute to the observed anisotropy. Electrical anisotropy in orthopyroxene is similar to olivine with the direction of highest electrical conductivity being about half a log unit higher than the other two directions. Therefore, electrical anisotropy of orthopyroxene, as determined in our study, does not provide

13.2. Applicability to Earth's upper mantle

an explanation for the observed electrical conductivity either. Various laboratory studies on shear-textures in mantle peridotites exist (e.g. [Skemer and Karato \(2008\)](#), [Sundberg and Cooper \(2008\)](#)), but electrical conductivity data of sheared mantle rocks are still lacking.

Part III.

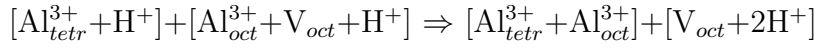
Modelling electrical conductivity with the diffusivity of hydrogen

14. Charge carriers and charge transport mechanisms in orthopyroxene

Due to the usage of synthetic orthopyroxene the number of possible conduction mechanisms is small. In pure enstatite, octahedral vacancies and protons are the major contributors to electrical conduction. Silicon vacancies are assumed to be rare in all samples, because the mixtures for orthopyroxene synthesis contained excess silicon to exclude formation of olivine (Section 2.1). In iron-bearing orthopyroxenes, polaron conduction is an important charge transport mechanism. Polarons are quasi-particles arising from lattice strain around a defect-cation, such as an Fe^{3+} -ion on an octahedral position in the orthopyroxene lattice. The extra positive charge attracts the surrounding oxygen atoms, causing a local strain. In contrast to the polaron caused by trivalent $\text{Al}_{\text{oct}}^{3+}$, the polaron caused by $\text{Fe}_{\text{oct}}^{3+}$ is very mobile, because it moves through passing an electron hole to an adjacent Fe^{2+} -cation. The concentration of mobile polarons equals the concentration of ferric iron and therefore depends on oxygen fugacity. Ferric iron concentration is also enhanced by dehydration through the reaction $\text{H}^+ + \text{Fe}^{2+} \Rightarrow 1/2\text{H}_2 + \text{Fe}^{3+}$ (e.g., Skogby and Rossman (1989); Bromiley et al. (2004); Stalder and Skogby (2007)). Because protons are exchanged with electron holes, electrical conductivity does not change through this reaction in iron-bearing orthopyroxene. The activation energy of polaron conduction is expected to be low compared to ionic conduction, because the transfer of electrons requires fewer energy than the movement of cations. Although orthopyroxenes of the upper mantle have relatively low iron contents (6-8 wt% of FeO

14. Charge carriers and transport mechanisms

and 0.3-0.6 wt% of Fe₂O₃ (Pearson et al., 2003)), polarons are probably important charge carriers. Charge transport mechanisms in aluminous enstatite cannot definitely be denominated, because Al³⁺-cations form various kinds of point-defect complexes, such as [Al_{oct}³⁺+V_{oct}+H⁺] and [Al_{oct}³⁺+Al_{tetr}³⁺], where "oct" and "tetr" denote Al³⁺ on an octahedral position and on a tetrahedral position, respectively, V denotes a vacancy and H⁺ a proton. As discussed in Chapter 8, the point-defect complexes in aluminous enstatite possibly rearrange, e.g.,



Octahedral vacancies charge balanced by two protons, as in pure enstatite, are the resulting protonated point defects from this reaction. This provides a possible explanation for the similarity between electrical conductivity of pure and aluminous enstatite. As hypothesised previously in Chapter 13, the protons bound to Al³⁺-cations on the left side of the reaction might not contribute to electrical conduction, whereas the protons on the right side do. H/D-exchange experiments showed that hydrogen is less mobile due to the stronger bond to Al³⁺-defects than to octahedral vacancies (Chapters 6, 7). The fraction of hydrogen incorporated by charge balancing octahedral vacancies can be estimated in aluminous enstatite from the area of the OH-bands in the FTIR-spectrum, which are also present in pure enstatite. This yields similar concentrations (250-330 ppm-wt H₂O) as in pure enstatite (200-300 ppm-wt H₂O). The reaction implies, that the fraction of mobile protons would increase with time, resulting in a time-dependent increase of electrical conductivity in aluminous samples. However, a continuously increasing electrical conductivity did not occur in this study, possibly due the slow kinetics of the reaction above compared to durations of electrical conductivity experiments, or superimposed dehydration.

Electrical conduction is linked to diffusion by the Nernst-Einstein equation:

$$\sigma = \frac{Dcz^2F^2}{RT} \quad (14.1)$$

with D the diffusion coefficient in $[m^2/s]$, c the concentration in $[mol/m^3]$, z the charge of the conducting species, F in $[C/mol]$ and R in $[J/mol]$ the Faraday's and the gas constant, respectively. Semiconduction is a thermally activated process and its temperature dependence can be described by an Arrhenian equation

$$\sigma = \sigma_0 \exp(-E/RT) \quad (14.2)$$

With $\sigma T = D \cdot \text{const.}$ from Equation 14.1, the following equation can be deduced, which allows direct comparison between diffusion and conduction via the activation energy of diffusion:

$$\sigma T = \sigma_0 T \exp(-E_a/RT) \quad (14.3)$$

The activation energy could be deduced from the linear regression of $\log(\sigma T)$ vs. $1000/T$ by calculating $E_a [kJ/mol] = \text{slope} \cdot R \cdot \ln(10)$. The mechanism of charge transport is discussed in the following by comparing the activation energy of electrical conduction to the activation energy of diffusion of cations and polarons in orthopyroxene.

Dehydration experiments with orthopyroxenes containing 6-12 wt% FeO total iron suggest an activation energy of 140-160 kJ/mol for polaron diffusion in orthopyroxene (Chapters 6, 8). Since dehydration of iron-bearing orthopyroxene is charge-balanced by a counterflux of electron holes, it is assumed that the kinetics of dehydration in iron rich orthopyroxenes equal the mobility of polarons. The H-diffusivity of dehydration of iron rich samples is used to model the electrical conductivity of iron-bearing orthopyroxenes. The diffusivity was determined for the crystallographical direction $\parallel[100]$, but since dehydration is isotropic $\parallel[100]$ and $\parallel[010]$ in pure enstatite (Stalder and Skogby, 2003), this diffusivity was also applied to electrical conductivities measured $\parallel[010]$. Analogously, the mobility of octahedral vacancies is assumed to equal the dehydration kinetics of pure enstatite, as determined by Stalder and Skogby (2003). Hydrogen is incorporated in pure enstatite mainly through charge-balancing octahedral vacancies. In order to maintain local charge neutrality,

14. Charge carriers and transport mechanisms

the two charge-balancing protons can only diffuse together with the vacancy. Therefore, dehydration diffusivity is assumed to equal the diffusivity of octahedral vacancies. The proton mobility in iron-free enstatite is deduced from the diffusivity of H/D-exchange in pure enstatite.

According to the Nernst-Einstein equation, electrical conductivity depends on the concentration of charge carriers (c_i), which add up to the measured electrical conductivity.

$$\sigma = \sum_i \frac{D_i c_i z_i^2 F^2}{RT} \quad (14.4)$$

The main charge carriers are assumed to be protons (H) and electron holes (h), both with charge $z=1$, and octahedral vacancies (V_{oct}) with $z=-2$. The equation then simplifies to:

$$\sigma = \frac{F^2}{RT} (D_h c_h + D_H c_H + D_{V_{oct}} c_{V_{oct}} 4) \quad (14.5)$$

The mix of charge carriers, their relative proportions and mobilities, determines the activation energy of the measured electrical conductivity. As shown in the next chapter, this model well explains the diverse activation energies obtained in this study. The diffusion parameters used for the model calculations are summarized in Table 14.1 and the model parameters are summarized in Table 15.1.

Table 14.1.: Diffusion parameters used for calculating the mobility of charge carriers.

Charge carrier	E_a [kJ/mol]	D_0 [m ² /s]	Source
H ⁺ in pure enstatite \parallel [100]	223.0	0.022	Ch. 7, Stalder and Behrens (2006)
H ⁺ in pure enstatite \parallel [010]	240.6	0.072	Ch. 7, Stalder and Behrens (2006)
H ⁺ in Al-bearing enstatite \parallel [001]	220.0	0.016	Ch. 7
H ⁺ and h ⁺ in Fe-bearing opx \parallel [010]+[100]	151.5	1.2e-05	Ch. 6
V_{Mg} \parallel [010]+[100]	295.0	1.37	Stalder and Skogby (2003)
Al ³⁺ -point-defects \parallel [100]	228.6	1.3e-04	Ch. 6

15. Modelling electrical conductivity

The equation 14.5 is used for modelling the electrical conductivity results, where the point defect concentrations are considered as parameters and fitted to the measured values. The implied polaron concentrations agree with ferric iron contents of similar synthetic orthopyroxenes determined with Mößbauer spectroscopic measurements (Section 3.2). The hydrogen concentrations were determined with FTIR-spectroscopy. Some hydrogen concentrations were estimated based on polarised measurements along two of the three crystallographic directions. The concentration of octahedral vacancies is not known, but (Smyth et al., 2007) synthesized Al- and H-bearing enstatite with 5% vacant octahedral positions. The vacancy concentrations matching the measured electrical conductivities range from 1.3 to 8% of all octahedral positions. In the following, the concentration of octahedral vacancies will always be given as a fraction of total octahedral positions. For example, for pure enstatite **pen5**, 8% vacant octahedral positions are required to match the measured electrical conductivity (Fig. 15.1). The sample was completely dehydrated in an Ar-gas-pressure vessel at 3 kbar and 1200°C for three days prior to the conductivity measurements. Therefore, octahedral vacancies can be assumed to be the major charge carriers in this sample. This is supported by the activation energy of 258 kJ/mol, which is similar to the high activation energy of octahedral vacancy diffusion, 295 kJ/mol.

In the following, the point defects and their respective concentrations obtained from the model calculations are described. In iron-free enstatite, the

15. Modelling electrical conductivity

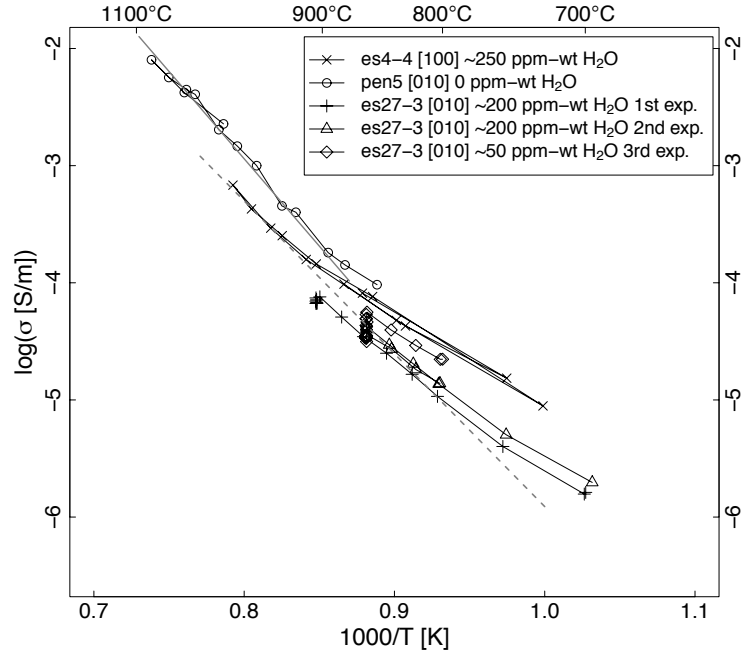


Figure 15.1.: Measured (symbols) and calculated (lines) electrical conductivity of pure enstatite samples. The broken line illustrates the discrepancy between activation energies of electrical conductivities and H-self-diffusion in pure enstatite. It represents calculated proton conductivity in pure enstatite $\parallel[010]$ with 200 ppm-wt H_2O .

octahedral vacancy concentration follows from the difference between the measured values and the calculated electrical conductivities with the measured hydrogen concentrations. In iron-bearing samples, the octahedral vacancy concentration follows from the activation energy. The model equations and the point defect concentrations are summarised in Table 15.1.

15.1. Pure enstatite

In contrast to the abovementioned hydrogen-free pure enstatite pen5, protons are likely to provide an additional contribution to electrical conductivity in hydrogen-bearing pure enstatite. However, the measured electrical conductivities of hydrogen-bearing pure enstatite and low-Al-enstatite with

~ 0.1 wt% Al_2O_3 can neither be modelled with hydrogen self-diffusion in pure enstatite, nor with octahedral vacancy diffusion. The activation energies of electrical conductivity are lower than any available activation energy of diffusion.

Sample **es4-4** shows a change in slope and the beginning of a region of higher activation energy at the highest temperatures, indicating an octahedral vacancy contribution. Electrical conductivities of the samples with low aluminium content are described in the beginning of the next Section 15.2 (the "br"-samples).

Pure enstatite sample **es27-3** was used for three experiments, as described in Chapter 12. The electrical conductivity increased for each experiment, although no continuous increase occurred during the experiments. The results of the first and the second experiment can not be modelled with proton or octahedral vacancy conduction due to the low activation energy of the measured electrical conductivity. The third experiment was carried out at ambient atmosphere and a temperature of 862°C . The temperature was held constant over 72 hours in order to observe the change in electrical conductivity during dehydration of the sample. A decrease of 0.3 log units in electrical conductivity occurred during this time. The decrease can be modelled with a simulated hydrogen concentration profile evolving with time due to dehydration. Dehydration kinetics parameters for pure enstatite are taken from [Stalder and Skogby \(2003\)](#). An initial concentration of 200 ppm-wt H_2O and a surface concentration of 40 ppm-wt H_2O was assumed by calculating concentration profiles according to Equation 5.8 (see Appendix C.3 for the calculated dehydration profiles). For a sample of thickness X , electrical conductivity was calculated for each of the $n = X/\Delta x$ concentration-points c_i in the profile, corresponding to a spatial resolution of $\Delta x = 0.1 \mu\text{m}$.

$$\sigma_i = \frac{F^2}{RT} \cdot c_i \cdot D_H \quad (15.1)$$

For D_H , the diffusivity of protons in pure enstatite obtained from H/D-exchange

15. Modelling electrical conductivity

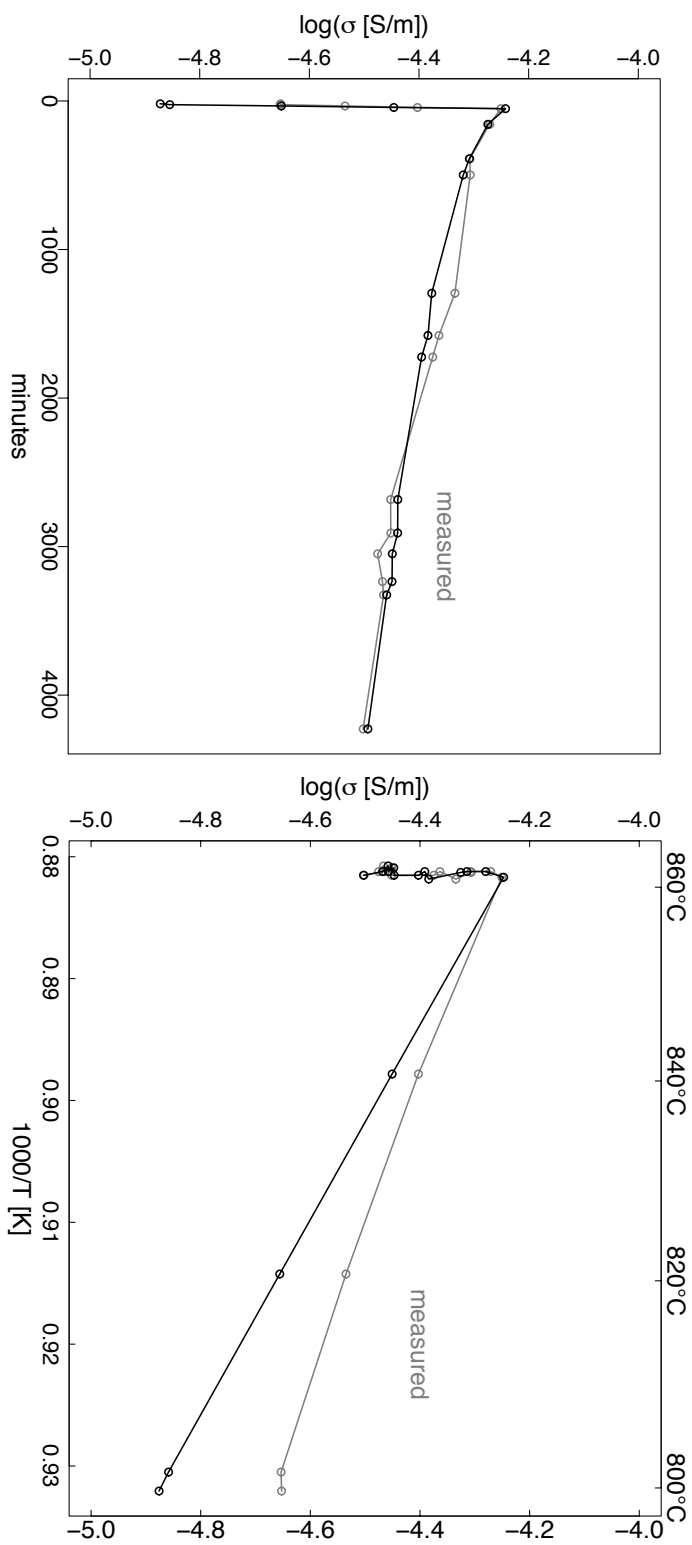


Figure 15.2.: Measured (grey) and calculated electrical conductivity of the third measurement of es27-3 as a function of time and of inverse temperature. The first datapoints, measured during heating, are not reproduced by the model. The decrease at constant temperature can be modelled by assuming a constant contribution of 3% V_{oct} and a continuous dehydration. Dehydrogenation kinetics are from [Stalder and Skogby \(2003\)](#) with an initial concentration of 200 ppm H_2O .

experiments was implied (Table 14.1). The inverse conductivity of each section, the resistances, are equivalent to a series connection of ohmic resistors. Hence, the total resistance ρ of the whole profile equals the sum of all resistivities ρ_i of the profile sections with thickness Δx , scaled to the total profile length X :

$$\rho = \sum_{i=1}^n \rho_i \cdot \Delta x \cdot \frac{1}{X} \quad (15.2)$$

Analogously, the total electrical conductivity σ_{H^+} can be calculated from the sum of the inverse electrical conductivities of the profile sections σ_i :

$$\sigma_{H^+} = \frac{\Delta x}{X} \sum_{i=1}^n \frac{1}{\sigma_i} \quad (15.3)$$

To match the measured electrical conductivity, a contribution of 3% octahedral vacancies to electrical conductivity was added (Tab. 15.1). As with sample es4-4, the low activation energy during the short heating period of the third experiment of sample es27-3 could not be reproduced with the model, since all available mobility parameters possess a higher activation energy (Fig. 15.2). The main consequence of this model calculation is that the decrease can be entirely attributed to hydrogen loss. Due to the fact that protons are not the only charge carriers in this sample, nearly complete dehydration of this pure enstatite leads to a decrease of only 0.3 log units in electrical conductivity, in contrast to the nearly 3 log units between hydrogen-bearing and hydrogen-free orthopyroxenes measured by Dai and Karato (2009a) at 8 GPa.

15.2. Al-bearing enstatite

The electrical conductivity of sample **br1-2a**, enstatite with 0.2 wt% Al_2O_3 , could be modelled similarly to es27-3, but without a contribution of octahedral vacancies. The model was based exclusively on proton conduction, i.e., on the mobility of H^+ in pure enstatite $\parallel[010]$. The sample initially contained more hydrogen than es27-3, was dehydrated only partially during the experiment (32% hydrogen loss), and electrical conductivity decreased slightly more

15. Modelling electrical conductivity

in a much shorter time period (0.4 log units in 10 hours). The common feature of both models is the mismatch in calculated and measured conductivity during the first heating, but the decrease is reproduced well by dehydration (Fig. 15.3). Dehydration was again calculated with Equation 5.8 assuming the dehydration kinetics of Al-bearing enstatite, an initial concentration of 280 ppm-wt H₂O, and a surface concentration of 10 ppm-wt H₂O (see Appendix C.2 for calculated dehydration profiles). Since the sample was heated in hydrogen atmosphere, dehydration was slowed down to approximately the rate of aluminous enstatite. That the dehydration rate of br1-2a is similar to the dehydration rate of enstatite containing 6-7 wt% Al₂O₃ (Chapter 6) should be considered coincidental, because the dehydration rate is probably negatively correlated with the aluminium concentration in enstatite. The mean concentration of the last calculated concentration profile is 141 ppm-wt H₂O, slightly lower than the bulk concentration of 185 ppm-wt H₂O, measured with FTIR-spectroscopy after the experiment.

The two samples **br1-3** and **br1-5** are chemically similar to br1-2a, they contain 0.1 wt% Al₂O₃. All three samples originate from the same synthesis-batch. However, electrical conductivity of br1-3 and br1-5 cannot properly be modelled with protonic conduction in pure enstatite. Both samples are oriented $\parallel(100)$, but their conductivity is slightly lower than that of br1-2a, oriented $\parallel(010)$ (Fig. 12.3). This disagrees with hydrogen diffusion being faster $\parallel[100]$ than $\parallel[010]$ in orthopyroxene. The electrical conductivity of br1-3 and br1-5 can approximately be matched with H⁺-conduction $\parallel[100]$ in pure enstatite and with a concentration of 130 ppm-wt H₂O, but the samples contain 210 and 240 ppm-wt H₂O (Fig. 15.4).

Although the sample **es7-8** contains 6 wt% Al₂O₃, i.e., much more aluminium and more hydrogen than the "br-samples", it exhibits a similar electrical conductivity. Interpretation of the conductivity of Al-bearing enstatite is complicated by the tendency of aluminium cations to form complexes of point-defects. As discussed above, it is also possible that a second Al-rich

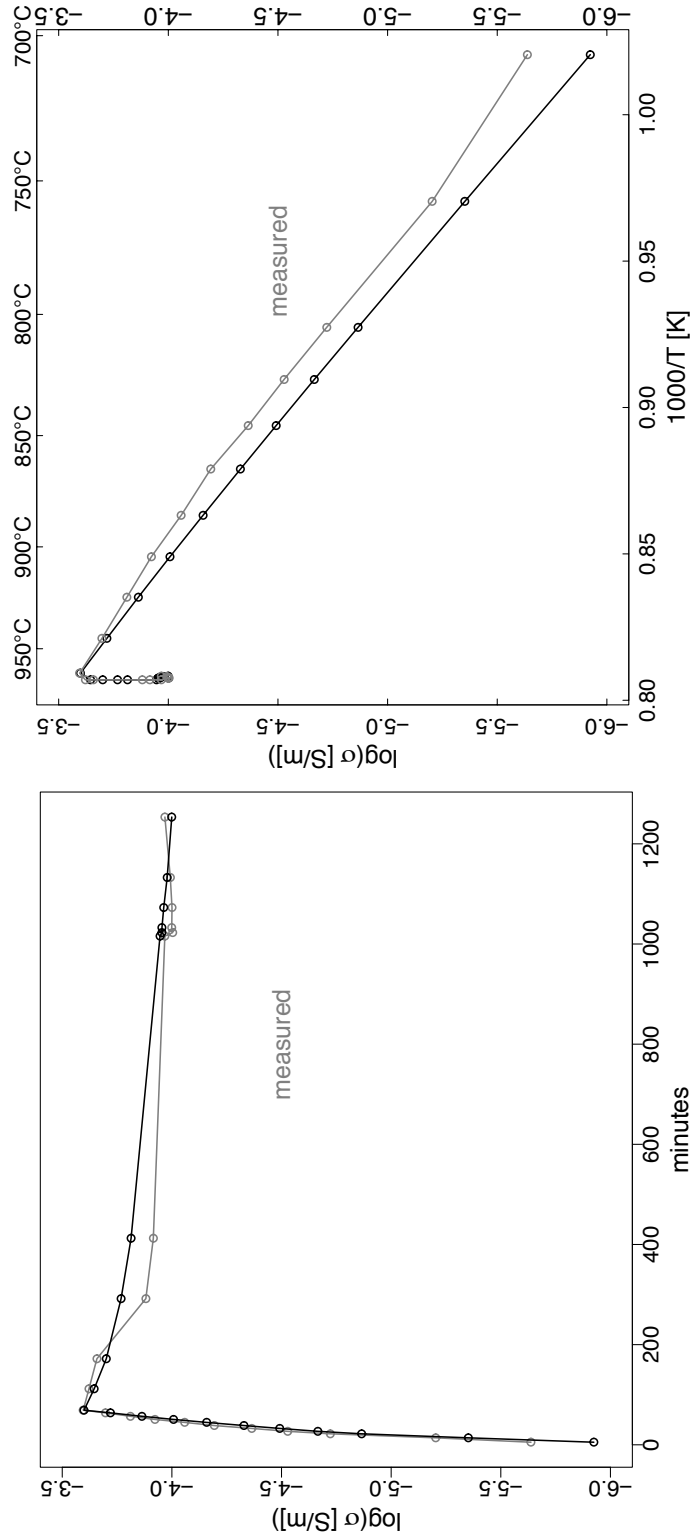


Figure 15.3.: Measured (grey) and calculated electrical conductivity of br1-2a as a function of time and of inverse temperature. The first datapoints measured during heating are not reproduced by the model. The decrease at constant temperature can be modelled by simulating dehydration with the dehydration-kinetics of aluminous enstatite with an initial concentration of 280 ppm H_2O .

15. Modelling electrical conductivity

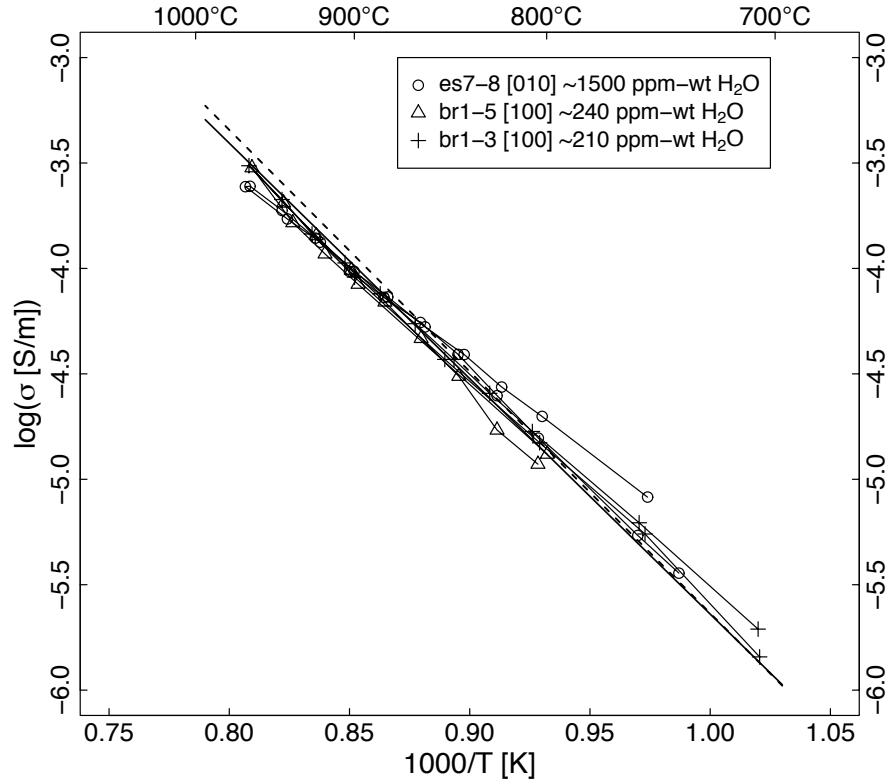


Figure 15.4.: Electrical conductivity of aluminous enstatites. The solid line represents H⁺-conduction $\parallel[100]$ with 130 ppm-wt H₂O, which matches the samples br1-3 and br1-5 but with a too low water content. The dashed line represents some Al³⁺-H⁺-related conduction mechanism with 2.4 wt% Al₂O₃, which could cause electrical conduction in sample es7-8.

phase exsolves in sample es7-8, causing the change to lower activation energy. The first datapoints of es7-8, which are most likely to represent the untreated sample, can be matched with a model which assumes a charge transport mechanism involving Al^{3+} -ions and having the mobility of dehydration of aluminous enstatite. The point-defect concentration required to match the measured values is equivalent to 2.4 wt% Al_2O_3 , assuming that every point-defect contains one Al-atom (Fig. 15.4).

The similarity between electrical conductivity in aluminous enstatite and pure enstatite suggests, that only V_{oct} -related protons contribute to electrical conductivity. However, neither pure enstatite nor aluminous enstatite can clearly be reproduced with calculated proton conduction, assuming the mobility of protons in pure enstatite, because the activation energies of the electrical conductivities are lower than of H-diffusivity. The reason for this are either inaccurate diffusion parameters for H/D-exchange in pure enstatite, or a different conduction mechanism operating in both pure and aluminous enstatite. It can not properly be tested if the electrical conductivity of aluminous enstatite could also be explained by proton conduction in aluminous enstatite because the diffusion parameters from H/D-exchange in aluminous enstatite are poorly constrained.

The Al-bearing samples es11-2a, es11-1, and es11-3 crystallized from the same batch, but they differ slightly in Al-contents (1.8 - 3.7 wt% Al_2O_3) and H-contents (Tab. 12.1 and 12.2). All three samples have about 0.5 log units higher electrical conductivities than the other pure and Al-bearing enstatite samples. They have been synthesized with D_2O and after the electrical conductivity measurements in hydrogen atmosphere, a H/D-diffusion coefficient could be deduced for es11-2a and es11-1, from the hydrogen and deuterium concentration profiles measured with FTIR-spectroscopy across the crystals. Calculated electrical conductivities with these diffusion coefficients and the corresponding $\text{H}_2\text{O}+\text{D}_2\text{O}$ -concentrations are compared to the measured values in Figure 15.5. The calculated electrical conductivities are lower than the

15. Modelling electrical conductivity

measured values, with electrical conductivity of es11-2a being about half a log unit higher than calculated. The activation energy of es11-2a is poorly constrained because the experiment was carried out nearly isothermally, but seems to agree with the activation energy of H/D-diffusion $\parallel[001]$ in aluminous enstatite.

The Haven ratio, the ratio of netto transport of diffusing ions and random diffusion, can not fully account for the observed differences. The netto transport is measured in diffusion experiments, whereas electrical conductivity comprises all ionic jumps, including immediately reversed. The Haven ratio of es11-2a is 0.6, the ratio of es11-1 is only 0.3. However, although poorly constrained, the activation energies of samples **es11-1** and **es11-3** are much lower (165 kJ/mol) than the activation energy of hydrogen diffusion in aluminous enstatite (246 kJ/mol) and in pure enstatite (Tab. 14.1), indicating different charge transport mechanisms. Application of the Haven ratio is therefore probably not appropriate. As for the other aluminous enstatite samples, the electrical conductivities of the es11-samples cannot be interpreted on the basis of existing diffusion data.

15.3. Fe- and Al-bearing orthopyroxene

A diffusion coefficient for H/D-exchange was additionally determined for one enstatite doped with aluminium and iron **es16-3b** (0.5 wt% Al_2O_3 and 1.7 wt% FeO total iron). The calculated protonic conductivity is more than half a log unit lower than the measured value. The sample contains 1.7 wt% FeO total; the fraction of ferric iron was not determined. Assuming an additional contribution of small polarons to electrical conduction corresponding to 10% ferric iron, the difference between the measured and the calculated conductivity at 843°C reduces to 0.14 log units (Fig. 15.6). The resulting Haven ratio is 0.7; it is 0.6 without the additional polaron contribution. The ferric iron content is given here and in the following in percentage of total iron. Mößbauer

15.3. Fe- and Al-bearing orthopyroxene

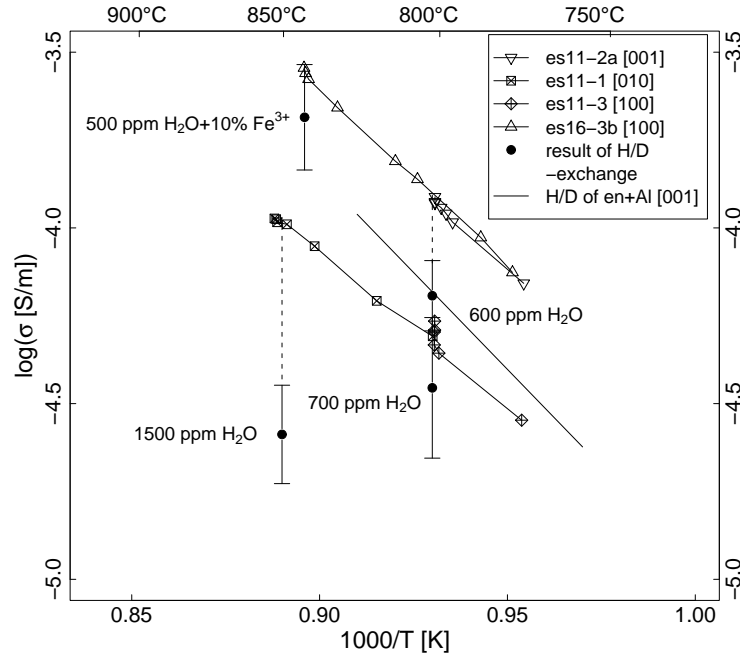


Figure 15.5.: Results of the electrical conductivity measurements with simultaneous H/D-exchange experiments.

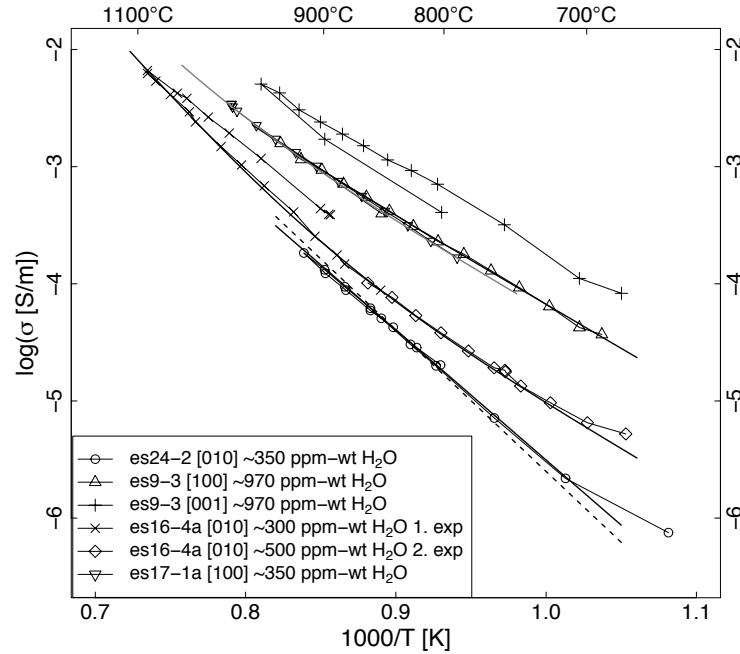


Figure 15.6.: Measured and calculated electrical conductivities of iron and aluminium bearing orthopyroxene samples. For es24-2 the two models are plotted (solid line and dashed line, see text for model description). For es9-3 only the model which includes V_{oct} -conduction is plotted. For es9-3 $\parallel[001]$ no model is available.

15. *Modelling electrical conductivity*

spectroscopic measurements showed that the ferric iron percentage of a similar sample was reduced from $\sim 11\%$ to $\sim 9\%$ after 1:45 h heat treatment in H_2 at 905°C and ambient pressure. The ferric iron content of sample **es16-3b** is probably higher than 9% , but lower than 11% , because it was heated in H_2 for 54 minutes in the combined H/D-exchange and electrical conductivity experiment.

The relatively high activation energy together with an electrical conductivity similar to pure enstatite indicate that the electrical conductivity of sample **es24-2** ($0.4 \text{ wt}\% \text{ Al}_2\text{O}_3$ and $2.0 \text{ wt}\% \text{ FeO}$ total iron) is probably dominated by protons having the mobility as in pure enstatite. The measured values can within range of uncertainty be reproduced by hydrogen diffusion $\parallel[010]$ in pure enstatite and a concentration of $360 \text{ ppm-wt H}_2\text{O}$, approximately the water concentration in this sample. The best fit is obtained with contributions of 0.6% ferric iron content and $280 \text{ ppm-wt H}_2\text{O}$. Both models suggest that electrical conductivity in this sample is determined by proton conduction and that the electronic contribution from ferric iron is minor.

The relatively low activation energy and the high electrical conductivity of **es9-3** ($0.4 \text{ wt}\% \text{ Al}_2\text{O}_3$ and $4.7 \text{ wt}\% \text{ FeO}$ total iron) suggest polaron conduction to be the dominating process. The model which explains the measured electrical conductivity $\parallel[100]$ uses a proton concentration of $970 \text{ ppm-wt H}_2\text{O}$, the water concentration determined with FTIR-spectroscopy, and a polaron concentration corresponding to 5% ferric iron. The mobility of the protons is assumed to be determined by the mobility of the polarons (Table 15.1). The ferric iron content was estimated on the basis of the Mößbauer measurements before and after heating a sample in H_2 , revealing that ferric iron was reduced from 11% to 9% after 1:45 h at 905°C . **es9-3** had already been heat-treated in H_2 in an earlier experiment at 800 to 900°C for two hours. Therefore, 5% ferric iron is a reasonable estimate. A better fit for the high temperature range of the measurement can be obtained by adding a contribution of 3% vacant octahedral positions to the model and reducing the concentration of

15.3. Fe- and Al-bearing orthopyroxene

polarons corresponding to 4.5% ferric iron. The sample had been polished to an oriented cube (Fig. 11.1) and electrical conductivity was measured along all three crystallographic directions. The first measurement along [010] failed, the second measurement \parallel [100] is discussed in this paragraph, and the third measurement along [001] was also successful. However, this measurement cannot be modelled because no data are available for polaron mobility \parallel [001].

The sample **es16-4a** (1.4 wt% Al_2O_3 and 3.7 wt% FeO total iron) was measured twice after being completely dehydrated in an Ar-gas-pressure vessel at 3 kbar and 1200°C for 6 days. During the first measurement in H_2 -gas, the sample regained about 300 ppm-wt H_2O and during the second experiment in ArH_2 -gas, water content of the sample probably remained constant or increased even more, because the sample could potentially incorporate 800 ppm-wt H_2O , the initial water content. FTIR-spectroscopic analyses after the second experiment are not available. The first measurement shows a hysteresis, but the second measurement with new electrodes exactly matches the first datapoint of the first measurement, excluding a time-dependent increase of electrical conductivity. A superimposed increase can also be excluded for the first measurement, because the two datapoints close to 1053°C were measured with a time-lag of 48 minutes, whereas the time intervals between the other datapoints were about five minutes. If electrical conductivity would have increased with time, the arrhenius plot would exhibit a step at 1053°C. The hysteresis in the cooling branch of the first measurement can therefore be attributed to degeneration of electrodes or electronic connections during cooling. Electrical conductivity did not change, despite the superimposed process of continuous rehydration. As mentioned earlier, dehydration or hydration through the iron redox reaction leads to a replacement of polarons by protons with the same mobility, and therefore has no effect on electrical conductivity. The fast rate of rehydration also suggests that es16-4a rehydrated through the iron redox reaction. The continuously increasing slope characterising the electrical conductivity of this sample, indicates at least two conduction mechanisms with

15. *Modelling electrical conductivity*

different activation energies. The measured values can well be reproduced by octahedral vacancy conduction together with a contribution of polarons. Octahedral vacancy concentration is assumed to be 4% of all octahedral positions, the fraction of ferric iron is assumed to be 3%. The polaron contribution might actually be partly replaced by protons with time, this would however not change the result.

Electrical conductivity of sample **es17-1a** (0.1 wt% Al_2O_3 and 10.2 wt% FeO total iron) can analogously be modelled with 6% vacant octahedral positions, protons corresponding to 350 ppm-wt H_2O , and polarons corresponding to 5% ferric iron.

The electrical conductivity of **En2-1**, a natural orthopyroxene from Tanzania with 0.2 wt% Al_2O_3 and 6.6 wt% FeO total iron, is probably dominated by polaron conduction. The activation energy of the measured values is slightly lower than the one of polaron conduction but the discrepancy lies within the range of uncertainty of the activation energy of diffusion (151 ± 65 kJ/mol). The model calculation involves 3% ferric iron. Since the sample contains virtually no hydrogen, proton conduction is not considered.

The natural mantle orthopyroxene **Mex5** (5.5 wt% Al_2O_3 and 7.0 wt% FeO total iron) from a peridotite xenolith originating from San Luis Potosi, Mexico, exhibits an electrical conductivity similar to the synthetic samples. The measured values can be modelled with the same model as the synthetic Fe- and Al-bearing samples, i.e., a contribution of 1.3% octahedral vacancies plus a polaron contribution corresponding to 1.3% ferric iron ($\cong 0.1$ wt% Fe_2O_3). The polaron contribution could also be caused by protons with polaron-mobility corresponding to 130 ppm-wt H_2O , since the sample contained ~ 150 ppm-wt H_2O . As with sample es16-4a, electrical conductivity does not change with time, although the sample is dehydrated during the experiment from measured 141 to 52 ppm-wt H_2O . The hysteresis in electrical conductivity of this sample can be attributed to an increasing interface contribution, probably a degradation of the electrode-sample contact. Therefore, the model is fitted only to the

15.3. Fe- and Al-bearing orthopyroxene

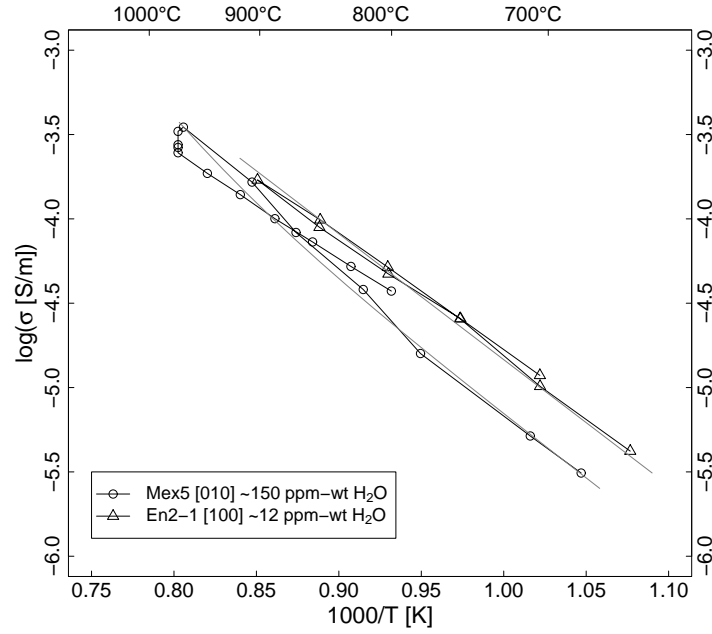


Figure 15.7.: Measured (symbols) and calculated (lines) electrical conductivities of natural orthopyroxenes.

heating branch.

Since the diffusion coefficients used to calculate electrical conductivities, possess an uncertainty that carries over to the resulting concentrations of charge carriers, they should therefore be considered as estimates for the relative contributions of charge carriers to electrical conduction.

Table 15.1.: Overview of equations and charge carrier concentrations used for the mathematical modelling of electrical conductivities according to equation 14.5.

Sample	Model equation	$c_{V_{oct}}$ [mol/m ³]	c_H [mol/m ³]	c_h [mol/m ³]	c_{Al} [mol/m ³]
pen5	$\sigma = F^2/RT \ c_{V_{oct}} \ 4 D_{V_{oct}}^a$	500			
es27-3	$\sigma = \sigma_H + F^2/RT \ c_{V_{oct}} \ 4 D_{V_{oct}}^a$	195	profiles ^b		
br1-2a	$\sigma = \sigma_H$		profiles ^b		
br1-3 & br1-5	$\sigma = F^2/RT \ c_H \ D_{H[100]}^c$		41.6		1550
es7-8	$\sigma = F^2/RT \ c_{Al} \ 9 D_{Al}^d$				
es11-1	$\sigma = F^2/RT \ c_H \ 5.4 \cdot 10^{-14} \ e$		480		
es11-2a	$\sigma = F^2/RT \ c_H \ 3.2 \cdot 10^{-13} \ e$		192		
es11-3	$\sigma = F^2/RT \ c_H \ 1.5 \cdot 10^{-13} \ e$		224		
es16-b	$\sigma = F^2/RT \ c_H \ 8.3 \cdot 10^{-13} + c_h D_h^e$		160	75	
es24-2	$\sigma = F^2/RT \ c_H \ D_{H[010]}^b$		115.2		
	$\sigma = F^2/RT \ c_{H,1} D_{H[010]} + c_{H,2} D_h^{c,f,g}$		89.6	5.6	
es9-3	$\sigma = F^2/RT \ (c_H + c_h) D_h^g$		310.4	104	
	$\sigma = F^2/RT \ c_{V_{oct}} \ 4 D_{V_{oct}} + (c_H + c_h) D_h^{a,g}$	200	310.4	94.5	
es16-4a	$\sigma = F^2/RT \ c_{V_{oct}} \ 4 D_{V_{oct}} + (c_H + c_h) D_h^{a,g}$	270		55	
es17-1a	$\sigma = F^2/RT \ c_{V_{oct}} \ 4 D_{V_{oct}} + (c_H + c_h) D_h^{a,g}$	380	112	238	
En2-1	$\sigma = F^2/RT \ c_h D_h^g$			90	
Mex5	$\sigma = F^2/RT \ c_{V_{oct}} \ 4 D_{V_{oct}} + c_h D_h^{a,g}$	85		41.6	

^a $c_{V_{oct}}$ is the concentration and $D_{V_{oct}}$ is the diffusivity of octahedral vacancies

^b σ_H calculated with simulated dehydration profiles (see text)

^c c_H is the concentration and D_H is the diffusivity of protons in pure enstatite $\parallel[100]$ or $\parallel[010]$

^d c_{Al} is the concentration and D_{Al} the diffusivity of Al-point defects

^eDiffusion coefficient from H/D-exchange during electrical conductivity experiment.

^f $c_{H,1}$ and $c_{H,2}$ are the concentrations of protons bond to octahedral vacancies and to ferric iron, respectively

^g D_h is the diffusivity of polarons or protons in Fe-bearing enstatite

16. Conclusions

(1) Electrical conductivities of the iron-bearing orthopyroxene samples can be modelled with the diffusivities of protons, polarons and octahedral vacancies. The model calculations imply that, due to the difference in activation energy between both charge transport processes, proton and polaron conduction dominate at temperatures below $\sim 900^\circ\text{C}$, whereas octahedral vacancy conduction becomes increasingly important at higher temperatures. The diversity in electrical conductivity and activation energy of the iron-bearing samples is a result of different contributions of polarons, protons and ions to the measured electrical conductivity. According to the model calculations, high electrical conductivities are primarily caused by polaron conduction, because their concentration is higher than that of the equally mobile protons in the higher conductive iron-bearing samples.

(2) Electrical conductivities of iron-free enstatite samples are relatively uniform, regardless of their hydrogen or aluminium content. Most of their activation energies are lower than the activation energy of any up to date available relevant diffusion process. Several possible explanations for electrical conductivity of hydrous pure and aluminous enstatite have been discussed, although none allowed consistent interpretation of the electrical conductivities of pure and aluminous enstatites.

(3) In iron-free enstatites, the concentration of electrically conducting hydrous point defects is much lower than the concentration of anhydrous point defects. Consequently, hydrogen concentration has little influence on electrical conductivity. In iron-bearing orthopyroxenes, a change in hydrogen concentration does not change the electrical conductivity, because the protons are

16. Conclusions

replaced by electron holes through oxidation of iron.

(4) Activation energies of the synthetic samples differ significantly from the ones of natural samples. According to the model calculations, ionic conduction via octahedral vacancies is an important charge transport mechanism in most synthetic samples, but is of minor influence in the natural orthopyroxenes. Electrical conduction of the natural samples arises mainly from polaron conduction. Since the water saturated synthesis conditions greatly enhance crystal growth, they might also enhance the concentration of octahedral vacancies in the synthetic samples with respect to the natural orthopyroxenes.

(5) High electrical conductivities of Earth's upper mantle cannot be explained entirely by the enhancement of electrical conductivity of olivine through hydrogen. Electrical conductivity of the second most abundant mineral in the upper mantle, orthopyroxene, was found to be virtually independent on hydrogen concentration. This implies that highly conductive regions in the upper mantle are probably not caused by proton conduction in the minerals. Hydrogen is potentially able to enhance electrical conductivity of upper mantle rocks, but rather through its tendency to concentrate at grain boundaries and inclusions or through triggering partial melting — processes which may lead to interconnected highly conducting pathways in upper mantle rocks.

Appendix A.

Syntheses and mineral formulas

Table A.1.: Table of Enstatite syntheses in a piston cylinder apparatus at 25 ± 5 kbar in the given temperature range $\pm 5^\circ\text{C}$.

Run	Start mix [wt%]	H ₂ O or D ₂ O	Temperatures [°C] - cooling rate
es1	En = 70 SiO ₂ + 30 MgO	H ₂ O	1400 → 1150 - 10°C/h
es2	En + 5 Fe ₂ O ₃	H ₂ O	1400 → 1150 - 10°C/h
es3	En + 5 Al ₂ O ₃ + 5 Fe ₂ O ₃	H ₂ O	1400 → 1150 - 10°C/h
es4	En	H ₂ O	1400 → 1150 - 10°C/h
es5	En + 5 Al ₂ O ₃ + 5 Fe ₂ O ₃	H ₂ O	1400 → 1150 - 10°C/h
es7	En + 18 Al ₂ O ₃	H ₂ O	1400 → 1150 - 10°C/h
es9	En + 2 Al ₂ O ₃ + 6 Fe ₂ O ₃	H ₂ O	1400 → 1150 - 10°C/h
es11	En + 11 Al ₂ O ₃	D ₂ O	1400 → 1150 - 10°C/h
es15	En + 5 Al ₂ O ₃ + 5 Fe ₂ O ₃	H ₂ O	1400 → 1150 - 10°C/h
es16	En + 3 Al ₂ O ₃ + 6 Fe ₂ O ₃	H ₂ O	1400 → 1150 - 10°C/h
es17	En + 16 Fe ₂ O ₃	H ₂ O	1400 → 1150 - 10°C/h
es23	En	H ₂ O	1400 → 1150 - 10°C/h
es24	En + 5 Al ₂ O ₃ + 5 Fe ₂ O ₃	H ₂ O	1400 → 1150 - 10°C/h
es26	En	H ₂ O	1400 → 1210 - 6°C/h
es27	En	D ₂ O	1400 → 1150 - 6°C/h
es29	En + 8 Al ₂ O ₃	H ₂ O	1400 → 1150 - 6°C/h
Br1	En + 5 Fe ₂ O ₃	H ₂ O	1400 → 1150 - 50°C/h
Br3	En	H ₂ O	1400 → 1150 - 6°C/h
Br4a	En	H ₂ O	1400 → 1150 - 6°C/h
Br5	En + 10 Fe ₂ O ₃	H ₂ O	1400 → 1150 - 50°C/h

Table A.2.: Stoichiometric coefficients of mineral formulas calculated from EMPA-analyses. Tetrahedral Al: $Al_{tet}=2-Si$; octahedral Al: $Al_{oct}=total\ Al-Al_{tet}$; Fe is assumed as ferrous iron.

Sample	Si	Al_{tet}	Mg	Fe	Al_{oct}	Mn	Ca	Na
Electrical conductivity experiments								
es9-3	2.04	0.00	1.80	0.14	0.02	0.00	0.00	0.00
es24-2	2.04	0.00	1.88	0.06	0.02	0.00	0.00	0.00
es16-3b	2.02	0.00	1.90	0.05	0.02	0.00	0.00	0.00
es16-4a	1.94	0.02	1.90	0.11	0.04	0.00	0.00	0.00
Mex5	1.89	0.11	1.62	0.20	0.12	0.00	0.04	0.01
En2-1	2.00	0.00	1.79	0.19	0.00	0.01	0.01	0.00
es17-1a	1.99	0.00	1.71	0.30	0.00	0.00	0.00	0.00
es7-8	1.88	0.07	1.87	0.00	0.18	0.00	0.01	0.00
es11-3	2.02	0.00	1.90	0.00	0.07	0.00	0.00	0.00
es11-2a	2.02	0.00	1.90	0.00	0.08	0.00	0.00	0.00
es11-1	1.93	0.07	1.93	0.00	0.07	0.00	0.00	0.00
Br1-5	2.05	0.00	1.95	0.00	0.00	0.00	0.00	0.00
Br1-2a	2.04	0.00	1.95	0.00	0.01	0.00	0.00	0.00
Br1-3	2.05	0.00	1.94	0.00	0.00	0.00	0.00	0.00
es27-3	2.04	0.00	1.96	0.00	0.00	0.00	0.00	0.00
Dehydration experiments								
es5-3	1.98	0.01	1.94	0.06	0.01	0.00	0.00	0.00
es5-4	1.98	0.02	1.92	0.06	0.01	0.00	0.00	0.00
es5-6	1.98	0.01	1.93	0.07	0.01	0.00	0.00	0.00
es5-7	1.99	0.01	1.95	0.05	0.00	0.00	0.00	0.00
es9-1	1.99	0.01	1.93	0.07	0.00	0.00	0.00	0.00
es9-2	1.98	0.01	1.86	0.14	0.01	0.00	0.00	0.00
es9-5	1.99	0.00	1.90	0.10	0.01	0.00	0.00	0.00
es9-6	1.99	0.00	1.92	0.08	0.01	0.00	0.00	0.00
es7-2	1.87	0.13	1.87	0.00	0.12	0.00	0.00	0.00
es7-3	1.82	0.18	1.81	0.00	0.19	0.00	0.00	0.00
es7-5	1.87	0.13	1.89	0.00	0.11	0.00	0.00	0.00
H/D-exchange experiments								
es3-4	1.98	0.02	1.89	0.09	0.02	0.00	0.00	0.00
es15-2	2.03	0.00	1.86	0.08	0.03	0.00	0.00	0.00
es24-3	2.00	0.00	1.88	0.09	0.03	0.00	0.00	0.00
es5-5	1.98	0.02	1.93	0.07	0.01	0.00	0.00	0.00
es29-2	1.99	0.01	1.90	0.00	0.10	0.00	0.00	0.00
es29-3	2.01	0.00	1.92	0.00	0.07	0.00	0.00	0.00
es29-1b	2.00	0.00	1.90	0.00	0.09	0.00	0.00	0.00
es4-8	2.03	0.00	1.96	0.00	0.00	0.00	0.00	0.00
es4-9	2.04	0.00	1.96	0.00	0.00	0.00	0.00	0.00

Appendix B.

Diffusion experiments

B.1. Dehydration experiments

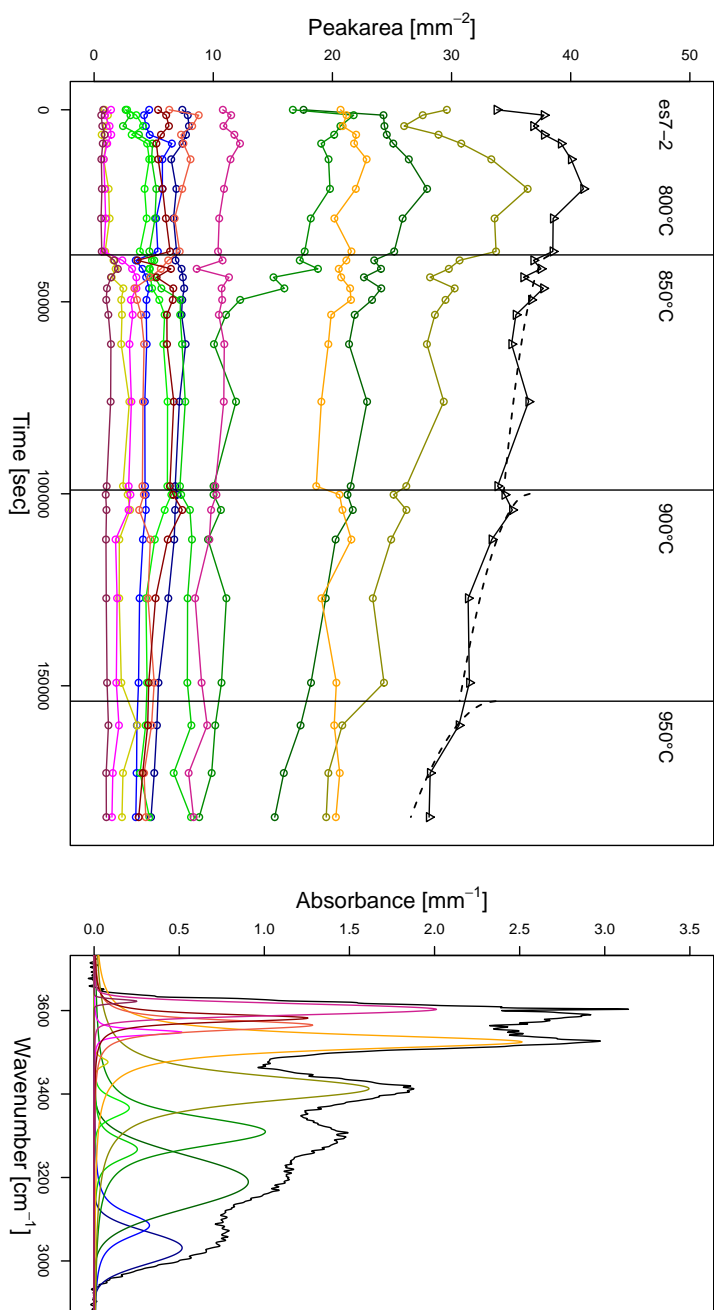


Figure B.1.: Evolution of absorbance with time for all four temperatures in series. Note that OH-absorbance increases at 800°C, subsequent decrease starts at higher temperatures. The colours of peaks in the right spectrum correspond to the colours in the left time series plot. The spectrum is plotted exemplarily, to illustrate the peak model applied by the software Peakfit. The black dataset is the sum of all peaks, scaled by a factor for clarity reasons. Dashed curves are the fitted diffusion equation.

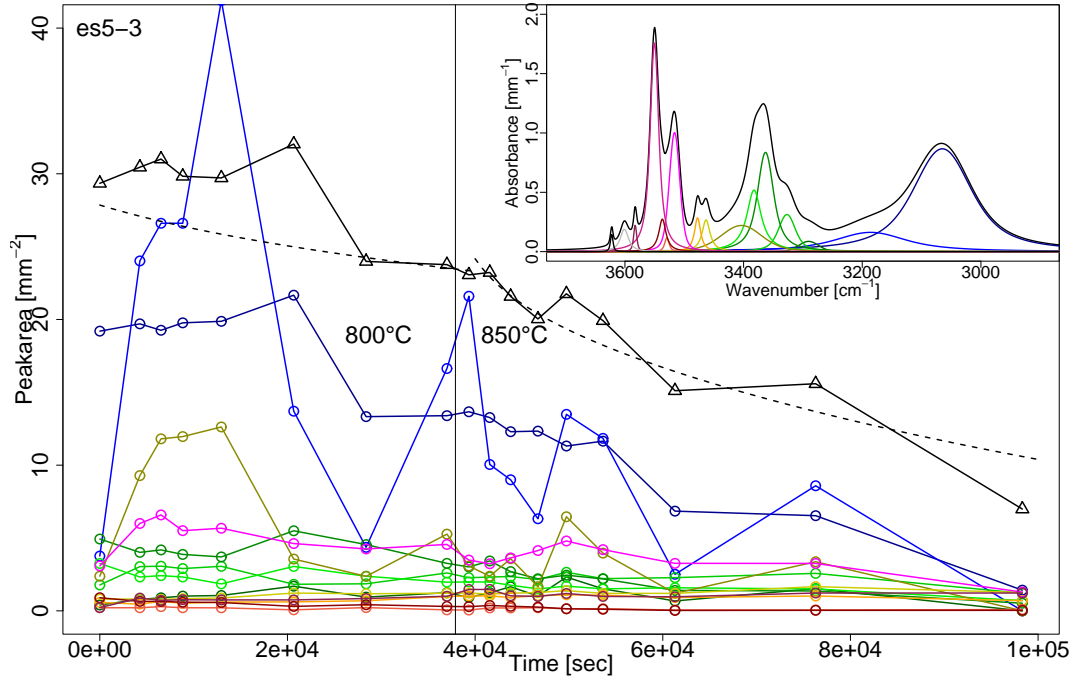


Figure B.2.: Time series for individual peaks (coloured) and sum of peaks (black). The broad peaks around 3200 and 3400 cm^{-1} were not included in the sum, because they show some abnormal behaviour. Nevertheless, OH-absorbance increases during heat treatment at 800°C . Assuming that the relaxation process does not influence the dehydration, all datapoints reflecting the increased absorbance were neglected for the fit of the diffusion equation (dashed curve). The diffusion coefficient deduced from the time series at 800°C has a large uncertainty because the absorbance decreases very little and is superimposed by the increase in absorbance and some scatter of the data. At 850°C the last datapoint was considered to be influenced by the diffusion profiles from the edges of the sample, and was ignored in the diffusion fit.

Appendix B. Diffusion experiments

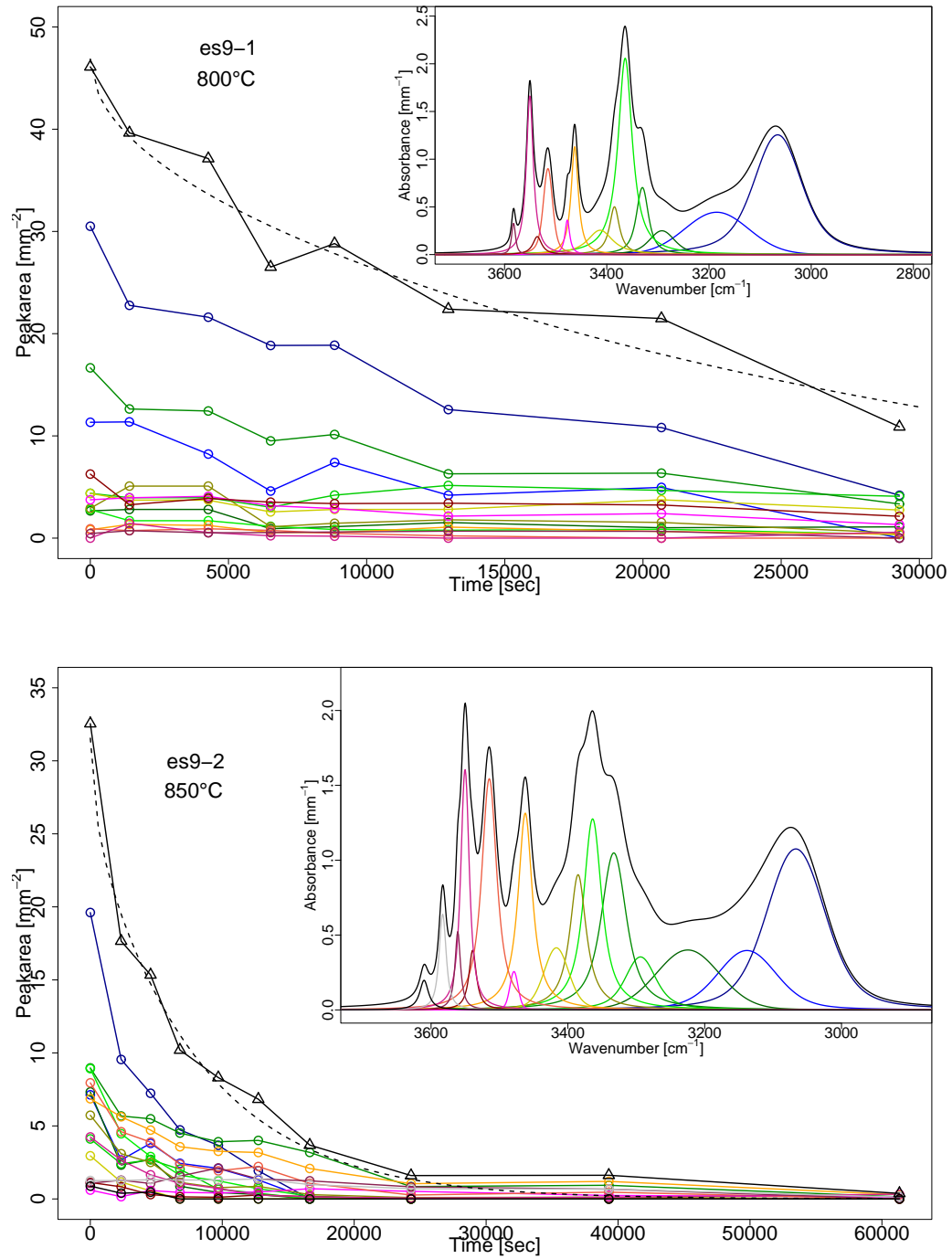


Figure B.3.: Time series of OH-absorbance and fitted diffusion equation (dashed curve).

B.1. Dehydration experiments

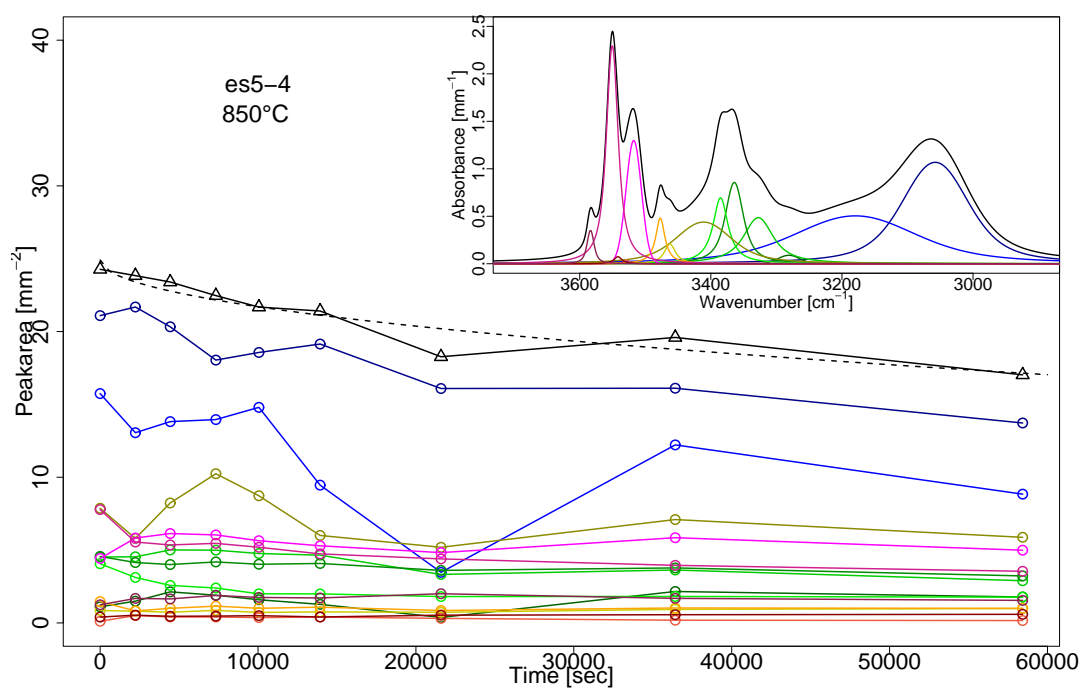


Figure B.4.: Time series of OH-absorbance and fitted diffusion equation (dashed curve). The broad peaks around 3200 and 3400 cm⁻¹ were not included in the sum, because they show some abnormal behaviour.

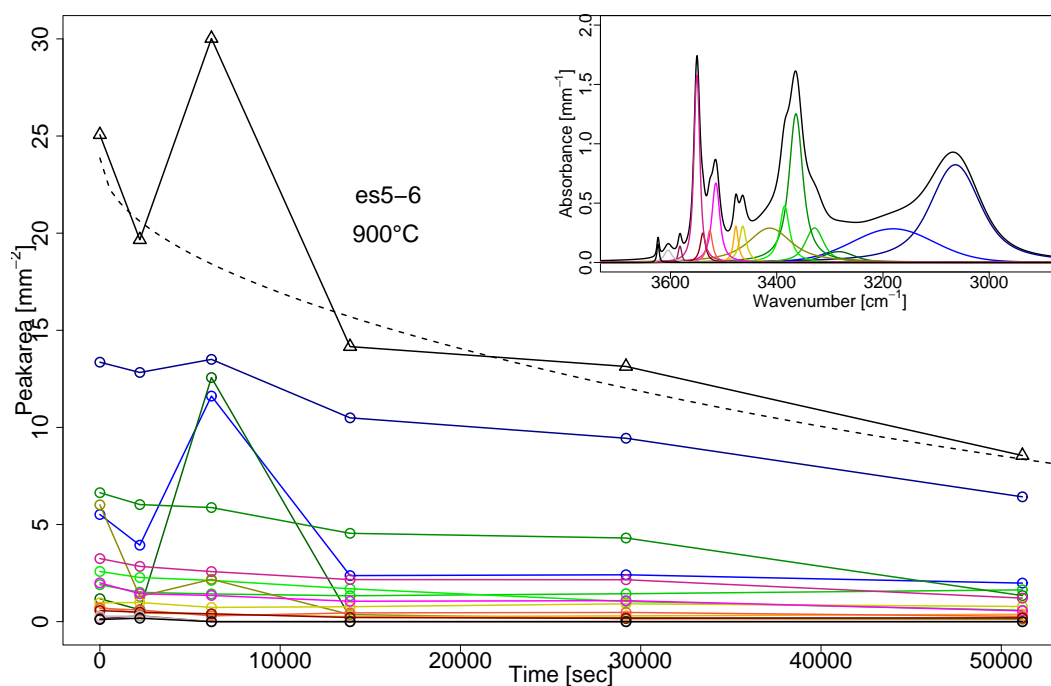


Figure B.5.: Time series of OH-absorbance and fitted diffusion equation (dashed curve). The third datapoint is regarded as an outlier and is not included in the fit of the diffusion equation. Reproducibility is probably reduced by the sinusoidal baseline of all spectra of this sample.

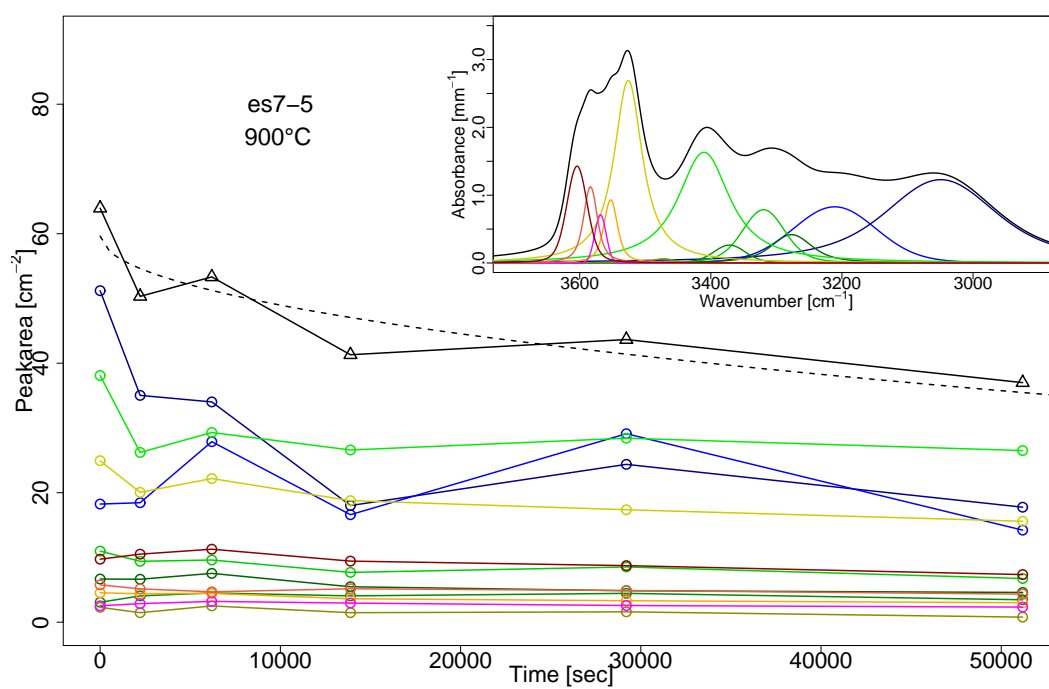


Figure B.6.: Time series of OH-absorbance and fitted diffusion equation (dashed curve). The broad peak around 3200 cm⁻¹ was neglected in the sum, because it showed some abnormal behaviour.

Appendix B. Diffusion experiments

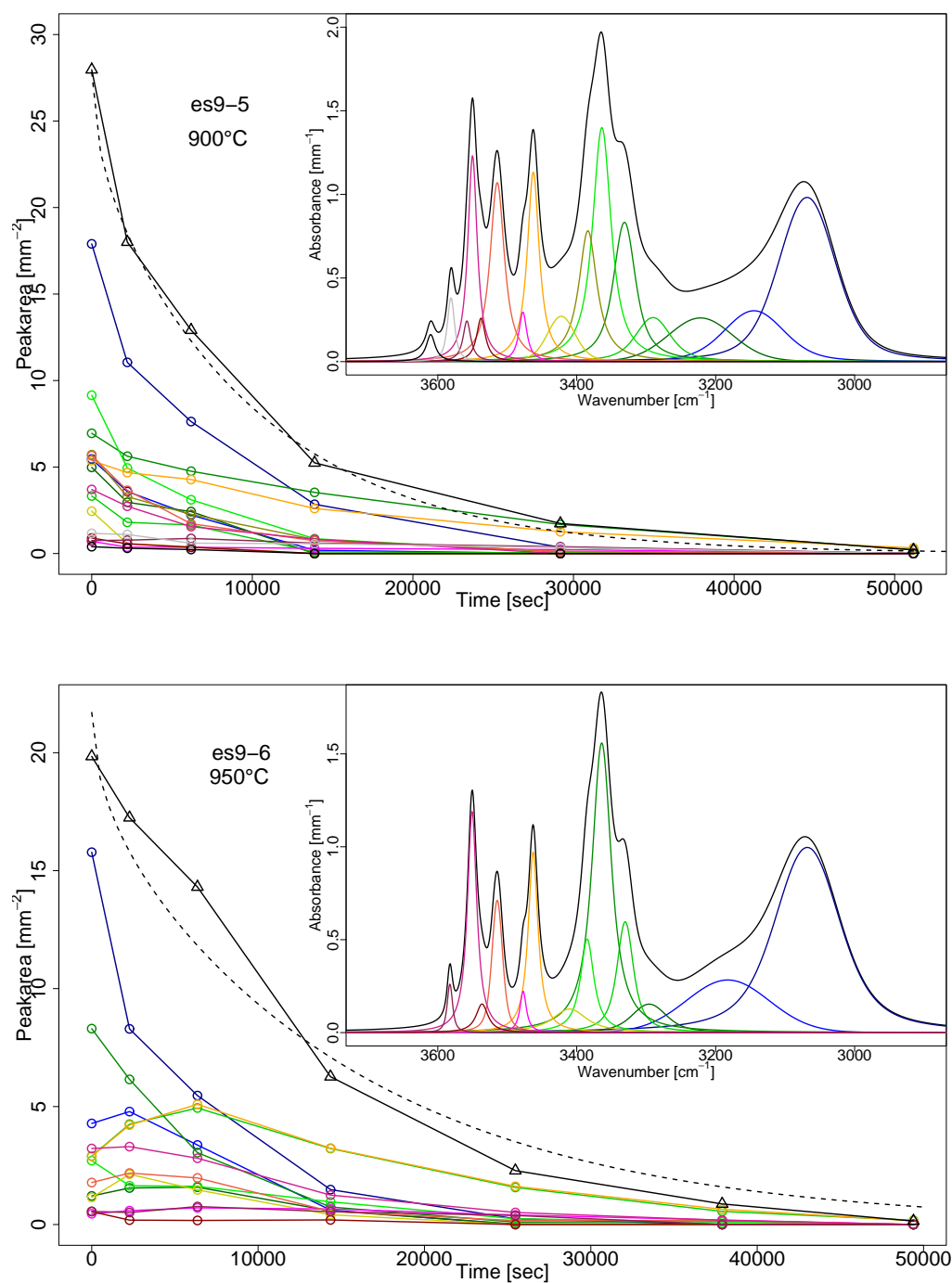


Figure B.7.: Time series of OH-absorbance and fitted diffusion equation (dashed curve). Note the increase of the Fe³⁺-related OH-peaks around 3330 and 3460 cm⁻¹ in the lower plot, which reflects the increase of Fe³⁺-content in the sample during tempering in air.

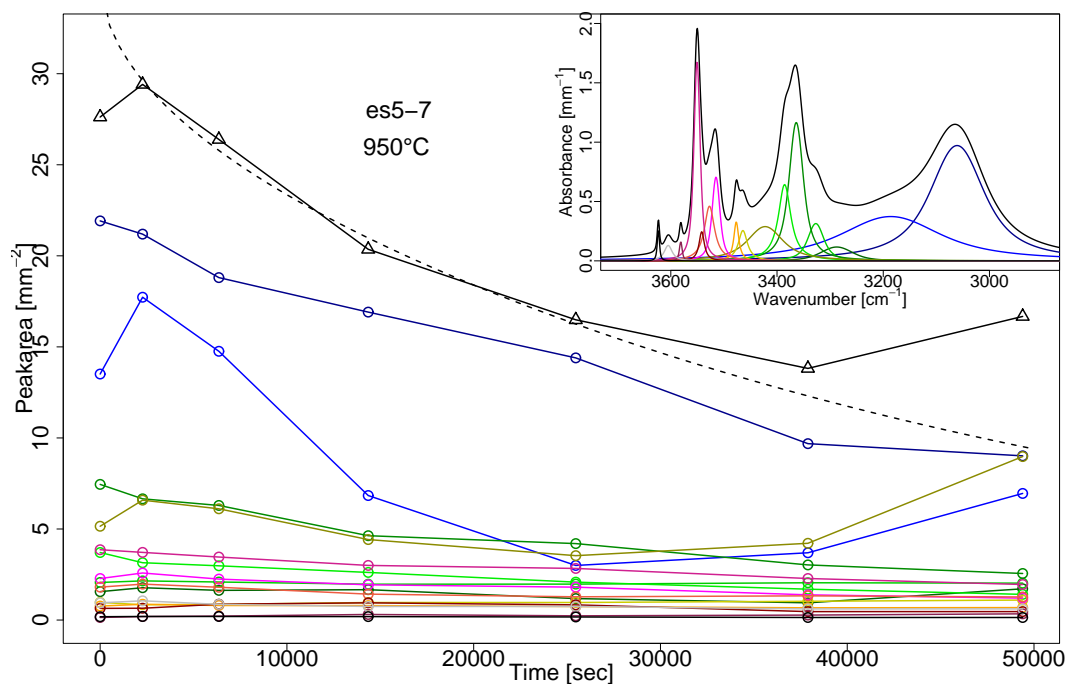


Figure B.8.: Time series of OH-absorbance and fitted diffusion equation (dashed curve). The two broad peaks around 3200 and 3400 cm^{-1} show some abnormal behaviour. In this case it was not appropriate to neglect these two peaks, because they have a significant influence on the trend of the sum. If the two peaks were neglected, the diffusion coefficient would be 0.3 log units lower. Here, the first datapoint is neglected to avoid the increase in OH-absorbance, caused mainly by the two abnormal peaks. IR-spectra of the last two datapoints were of bad quality with a high background. The last two datapoints were therefore neglected in the fit of the diffusion equation.

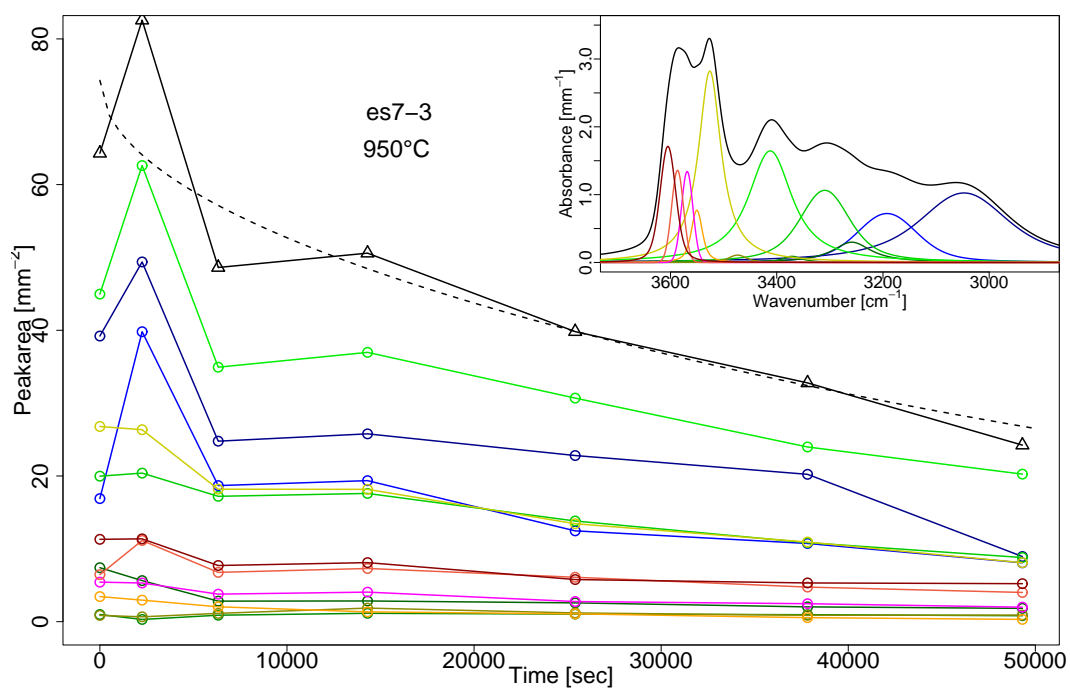


Figure B.9.: Time series of OH-absorbance and fitted diffusion equation (dashed curve). Since all peaks are affected by the scatter in the first three timepoints, a problem of baseline subtraction is assumed here. All data are included in the fit of the diffusion equation.

B.1. Dehydration experiments

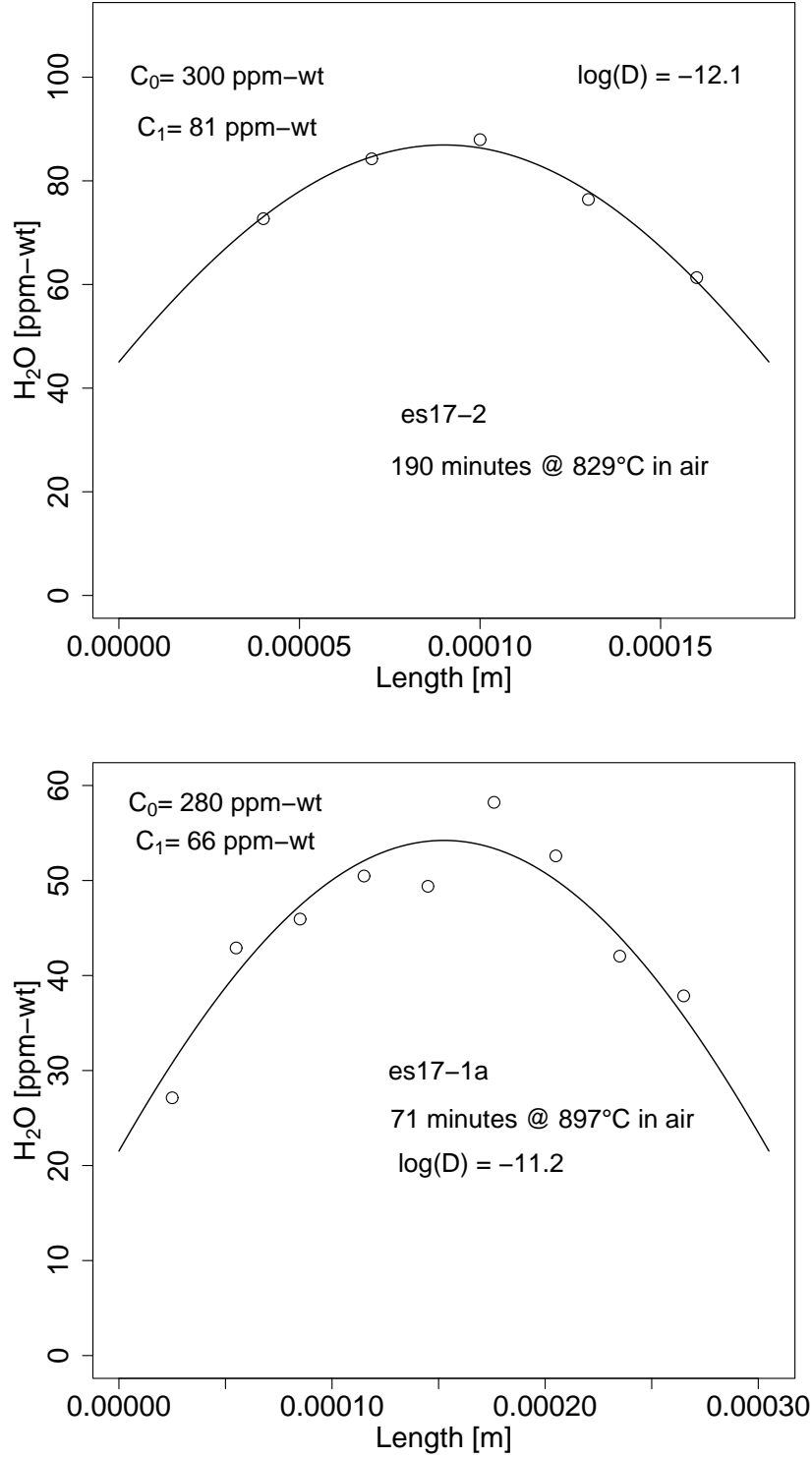


Figure B.10.: Concentration profiles of samples es17-2 and es17-1a: points are measured concentrations, the curve is the fitted diffusion equation with parameters C_0 as initial concentration and C_1 as surface concentration.

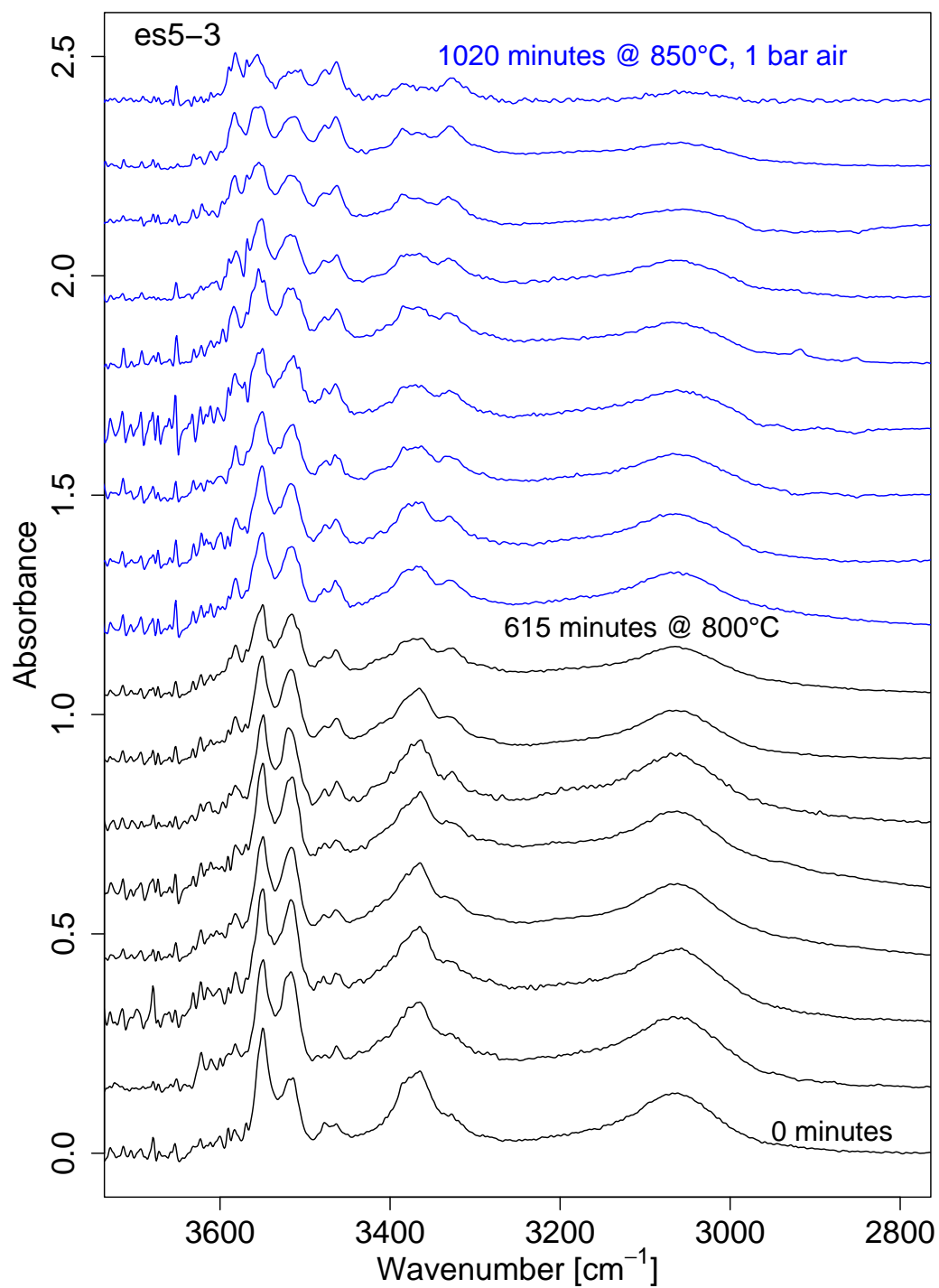


Figure B.11.: Consecutive spectra after each dehydration step of sample es5-3.

B.1. Dehydration experiments

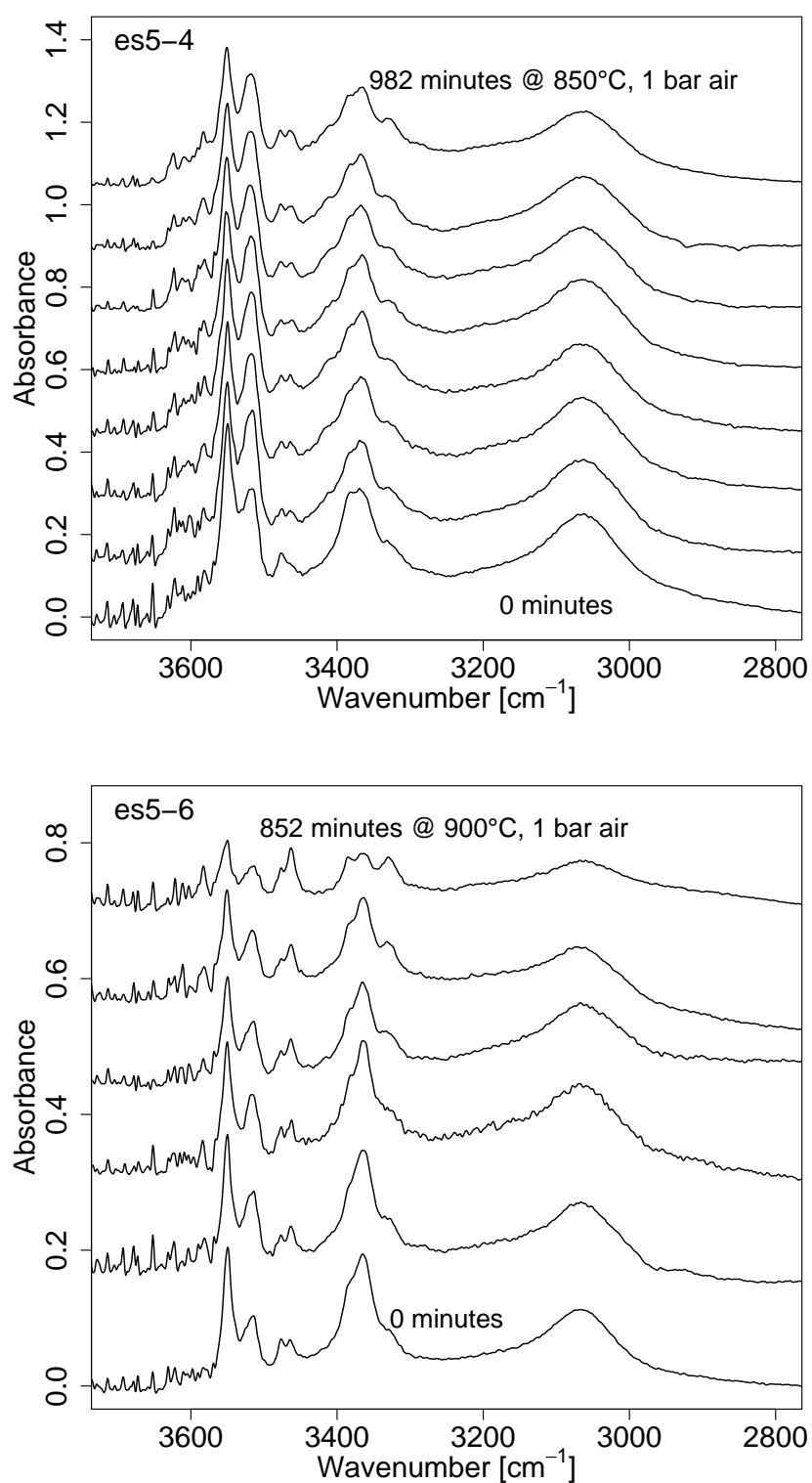


Figure B.12.: Consecutive spectra after each dehydration step of samples es5-4 and es5-6.

Appendix B. Diffusion experiments

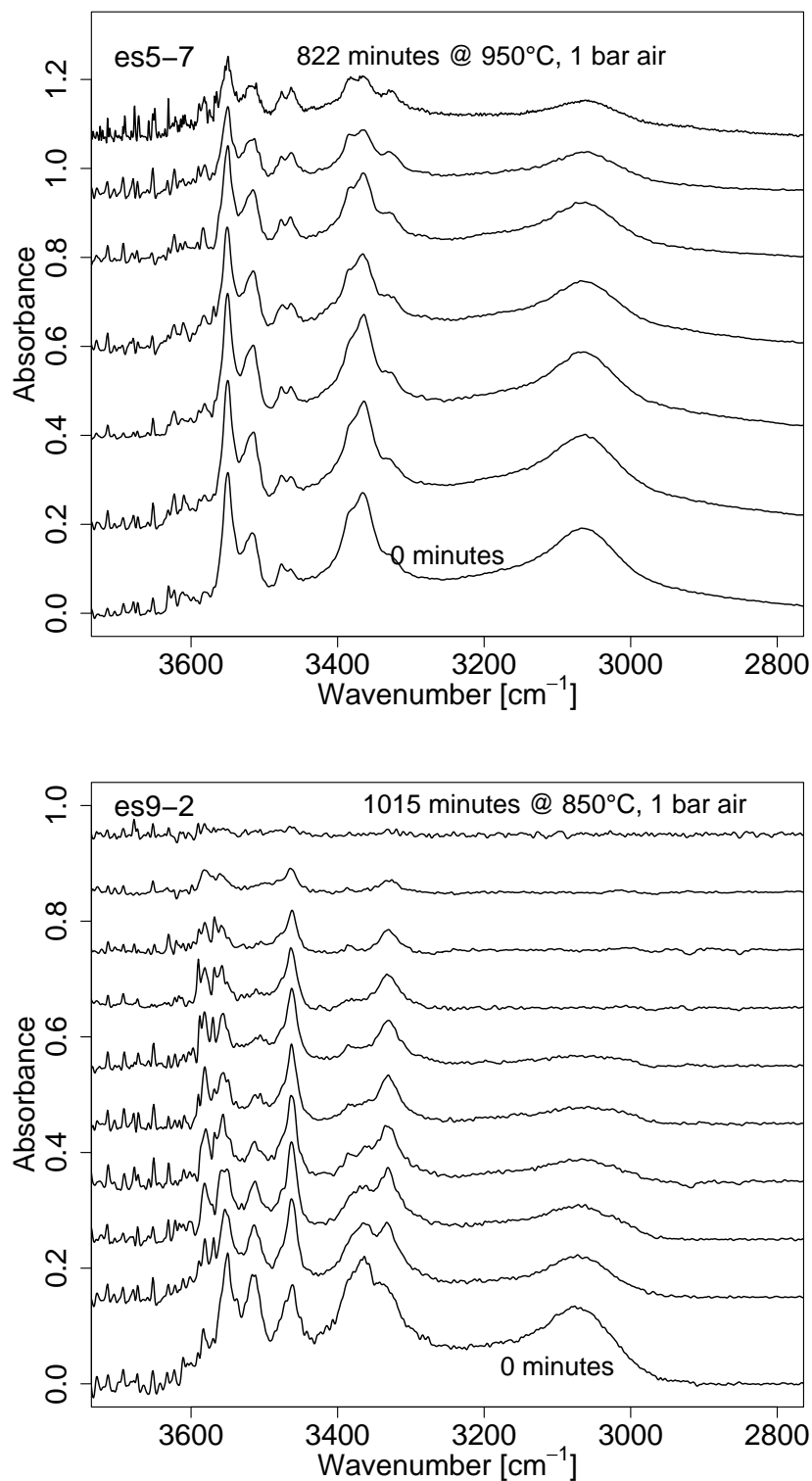


Figure B.13.: Consecutive spectra after each dehydration step of samples es57 and es9-2.

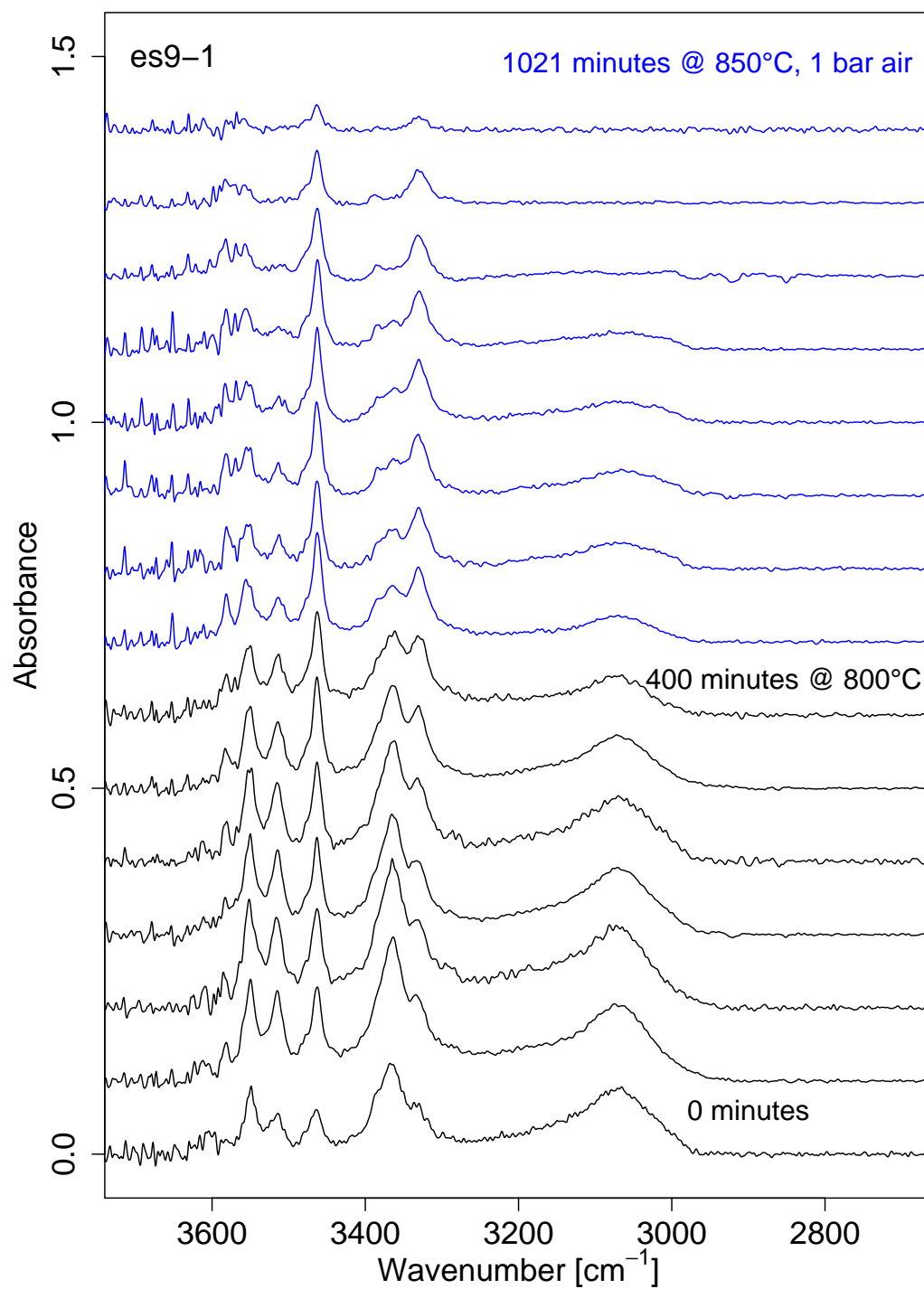


Figure B.14.: Consecutive spectra after each dehydration step of sample es9-1.

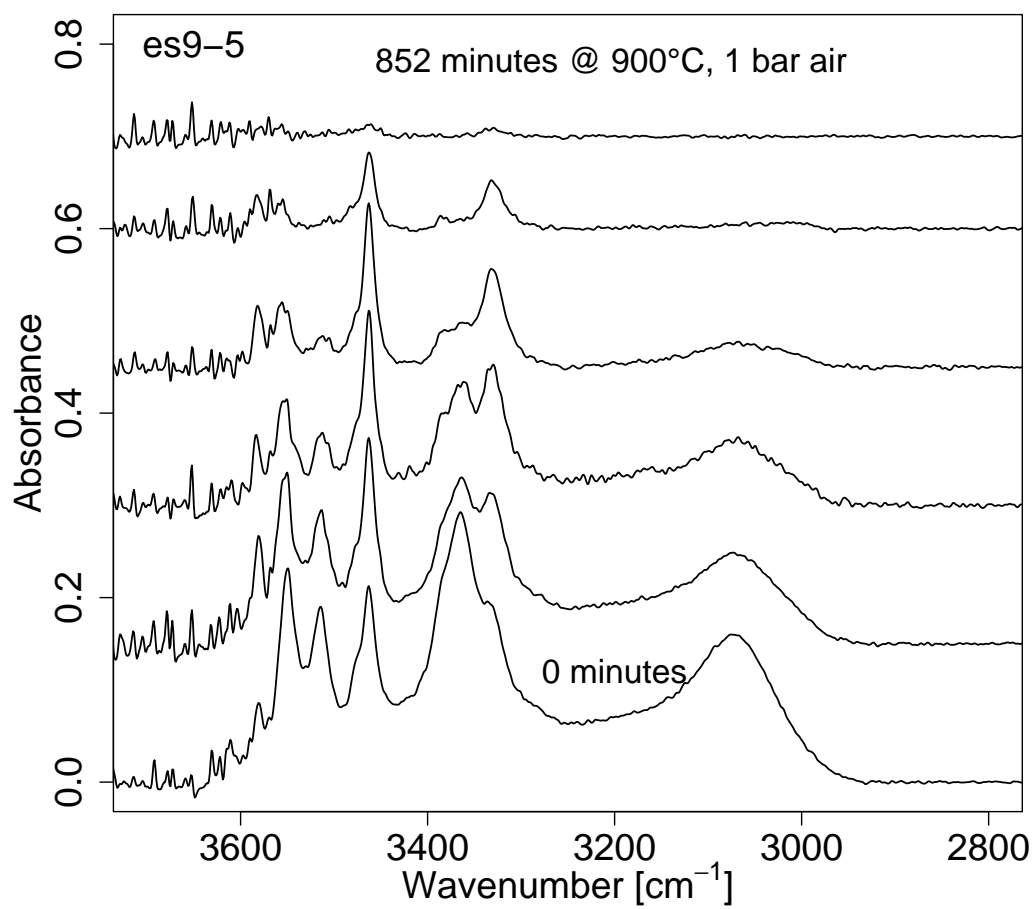


Figure B.15.: Consecutive spectra after each dehydration step of sample es9-5.

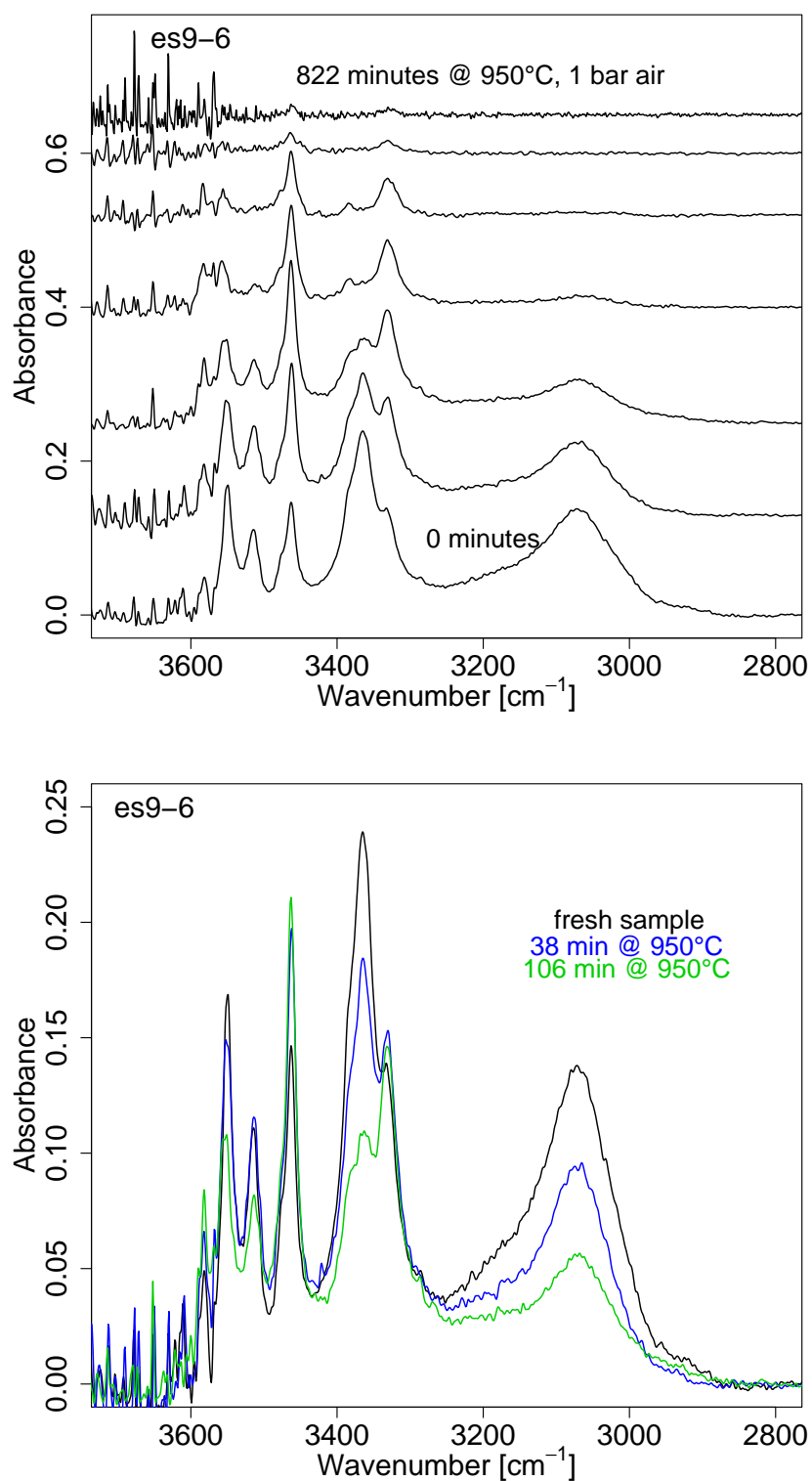


Figure B.16.: Consecutive spectra after each dehydration step of sample es9-6. Note the increase of Fe³⁺-related OH-bands around 3330 and 3460 cm⁻¹ with time.

Appendix B. Diffusion experiments

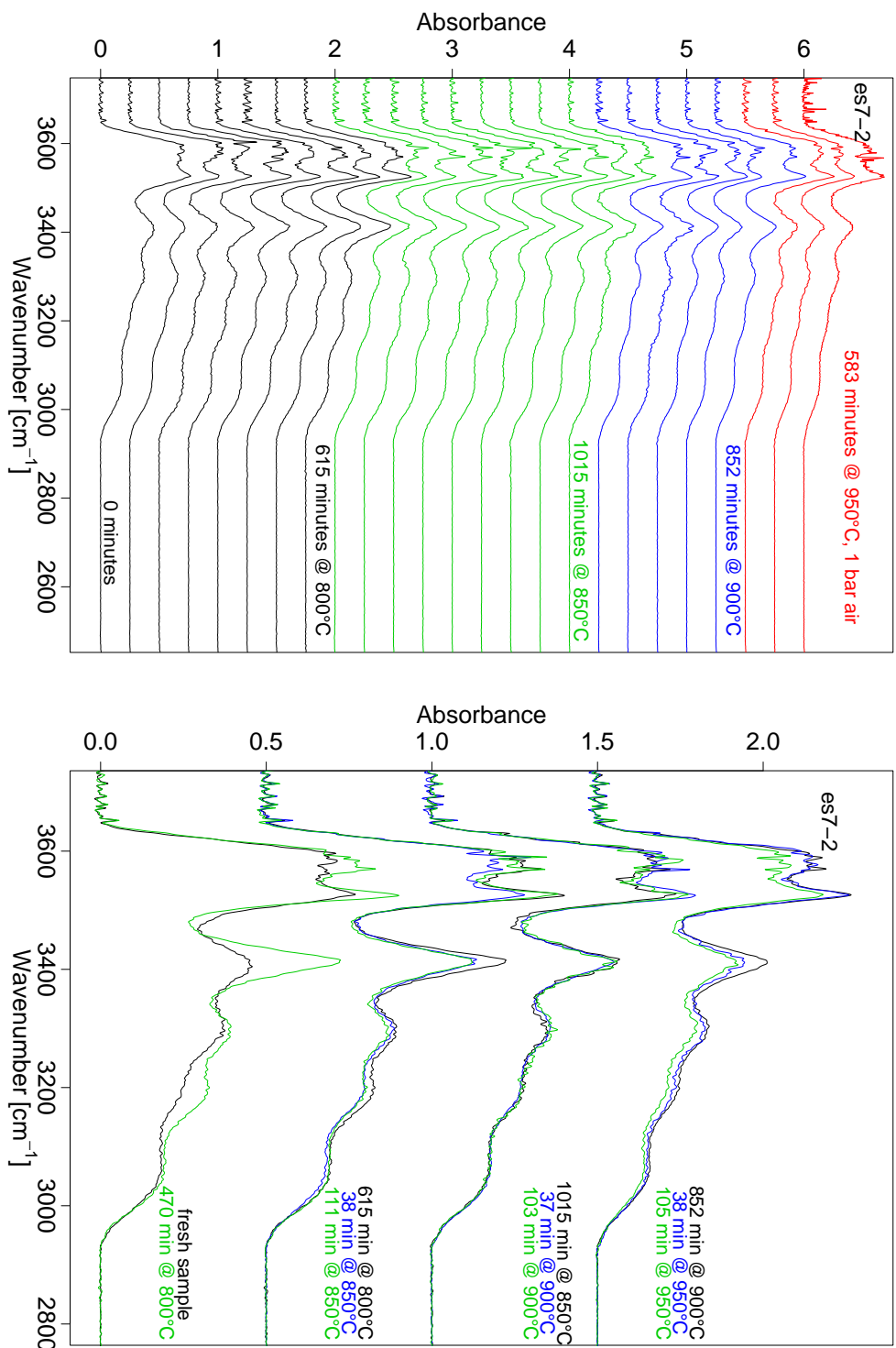


Figure B.17: Consecutive spectra after each dehydrations step of sample es7-2. The right plot illustrates, that the initial increase of absorbance is mainly due to the increase of the peaks around 3200 and 3400 cm⁻¹.

B.1. Dehydration experiments

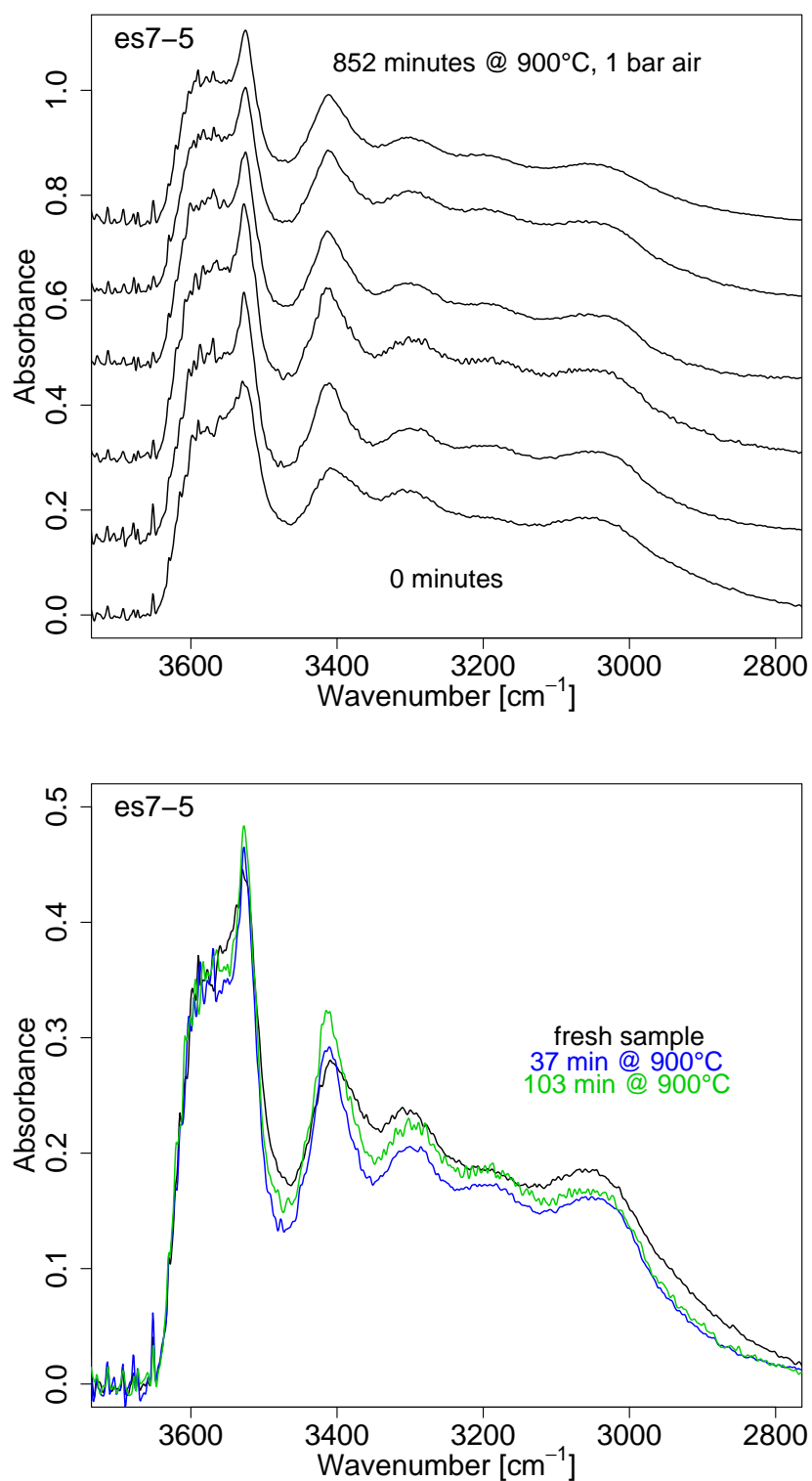


Figure B.18.: Consecutive spectra after each dehydration step of sample es7-5. Note the increase of absorbance with time.

Appendix B. Diffusion experiments

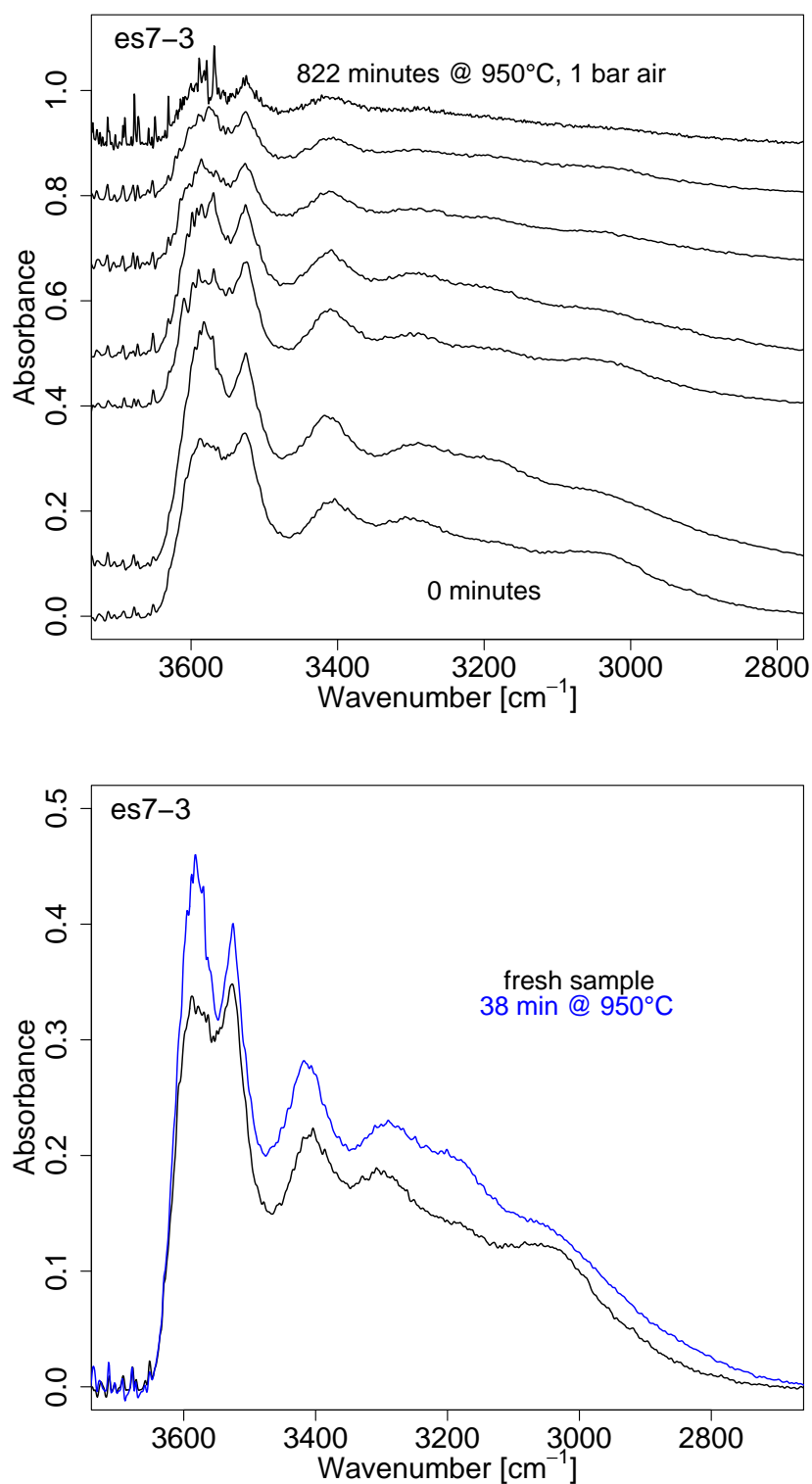


Figure B.19.: Consecutive spectra after each dehydration step of sample es7-3. Note the increase of absorbance with time.

B.1. Dehydration experiments

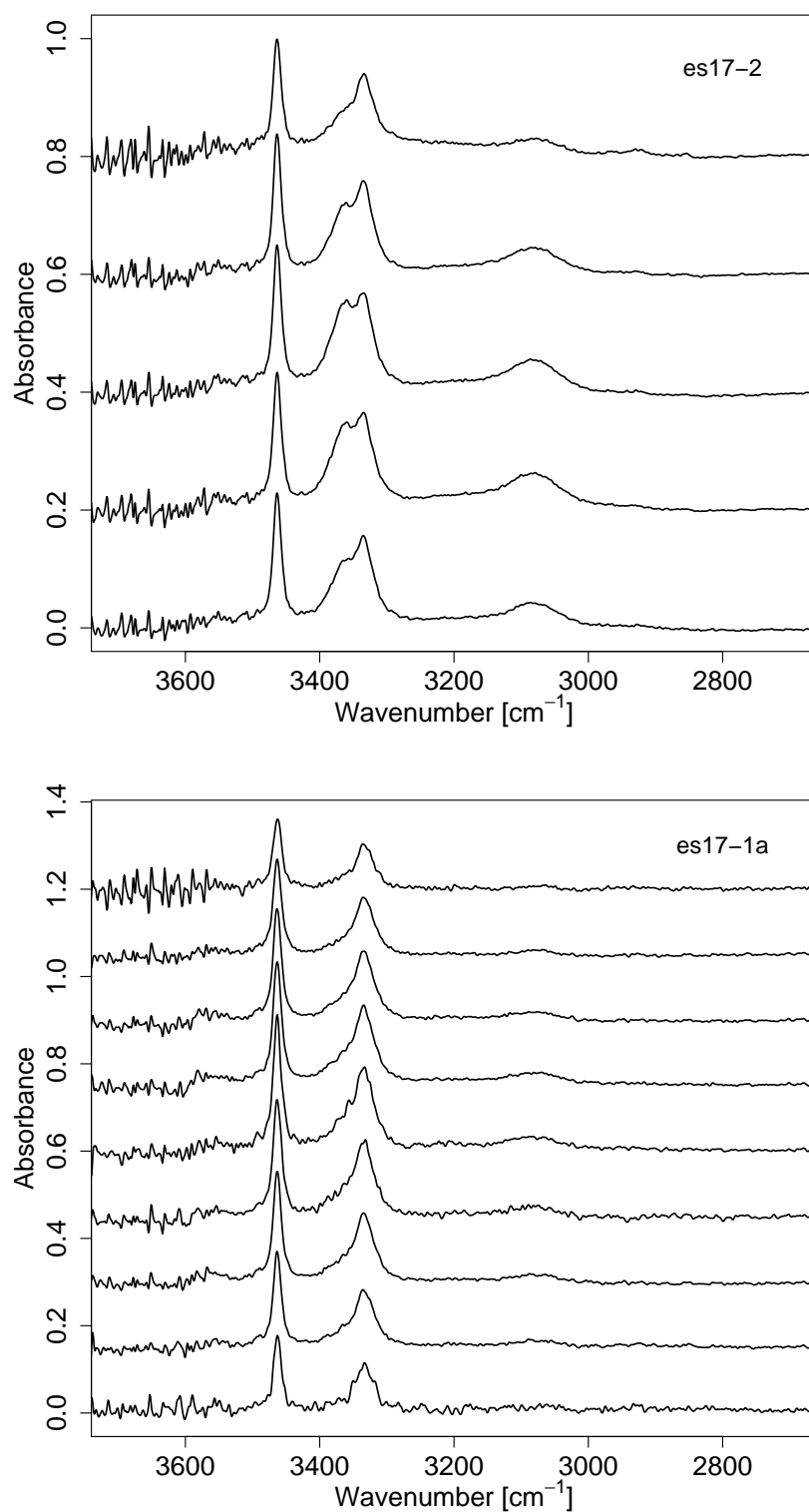


Figure B.20.: Spectra of the profiles of samples es17-2 and es17-1a.

B.2. H/D-exchange experiments

B.2. H/D-exchange experiments

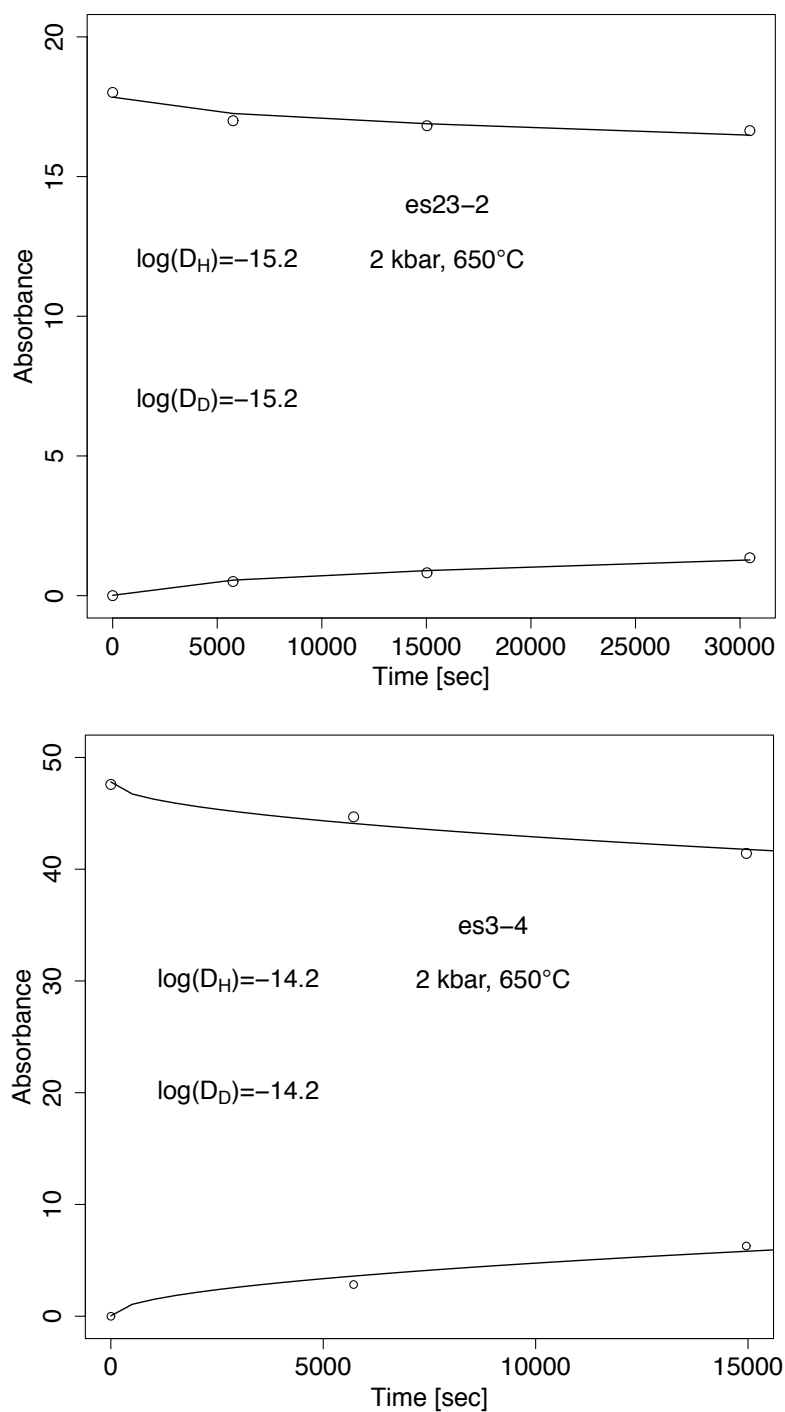


Figure B.21.: Time series of OH- and OD-absorbance (circles) with fitted diffusion equation (lines). $\log(D_H)$ and $\log(D_D)$: logarithm of the resulting diffusion coefficients of hydrogen and deuterium respectively.

Appendix B. Diffusion experiments

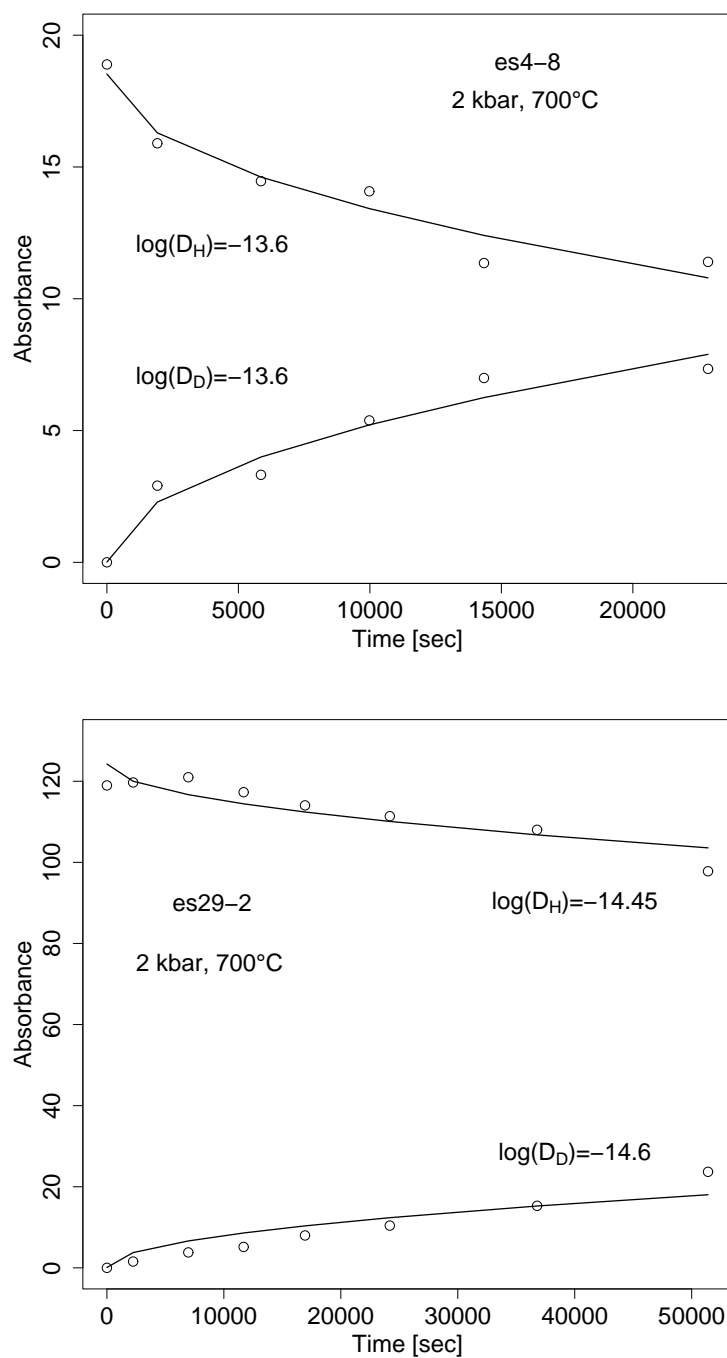


Figure B.22.: Time series of OH- and OD-absorbance (circles) with fitted diffusion equation (lines). Note that due to the increase in OH-absorbance of sample es29-2, the diffusion coefficient of this sample may be underestimated.

B.2. H/D-exchange experiments

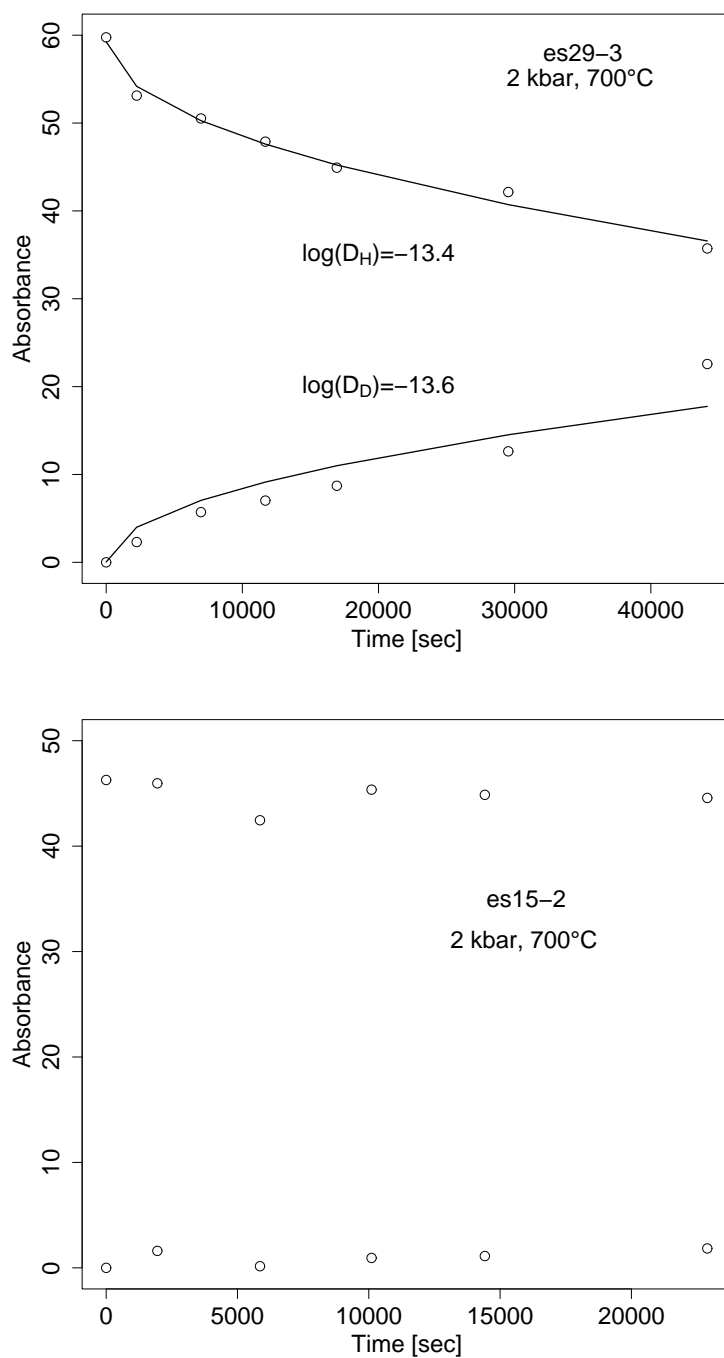


Figure B.23.: Time series of OH- and OD-absorbance (circles) with fitted diffusion equation (lines). The absorbance of sample es15-2 virtually did not change over time, possibly due to a leaky capsule in one experiment. Therefore, no reliable diffusion coefficient could be deduced from this time series (see also the consecutive spectra [B.29](#)).

Appendix B. Diffusion experiments

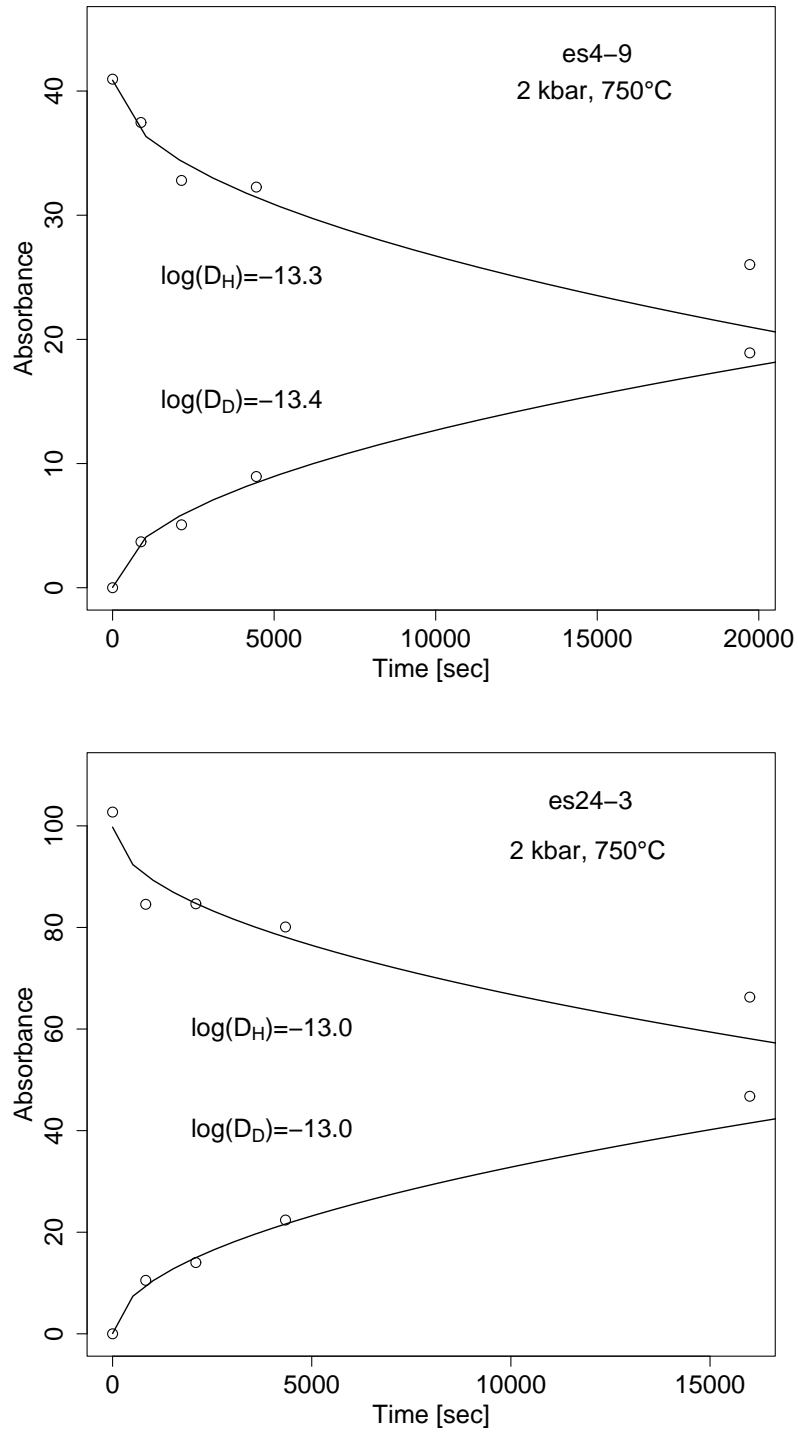


Figure B.24.: Time series of OH- and OD-absorbance (circles) with fitted diffusion equation (lines).

B.2. H/D-exchange experiments

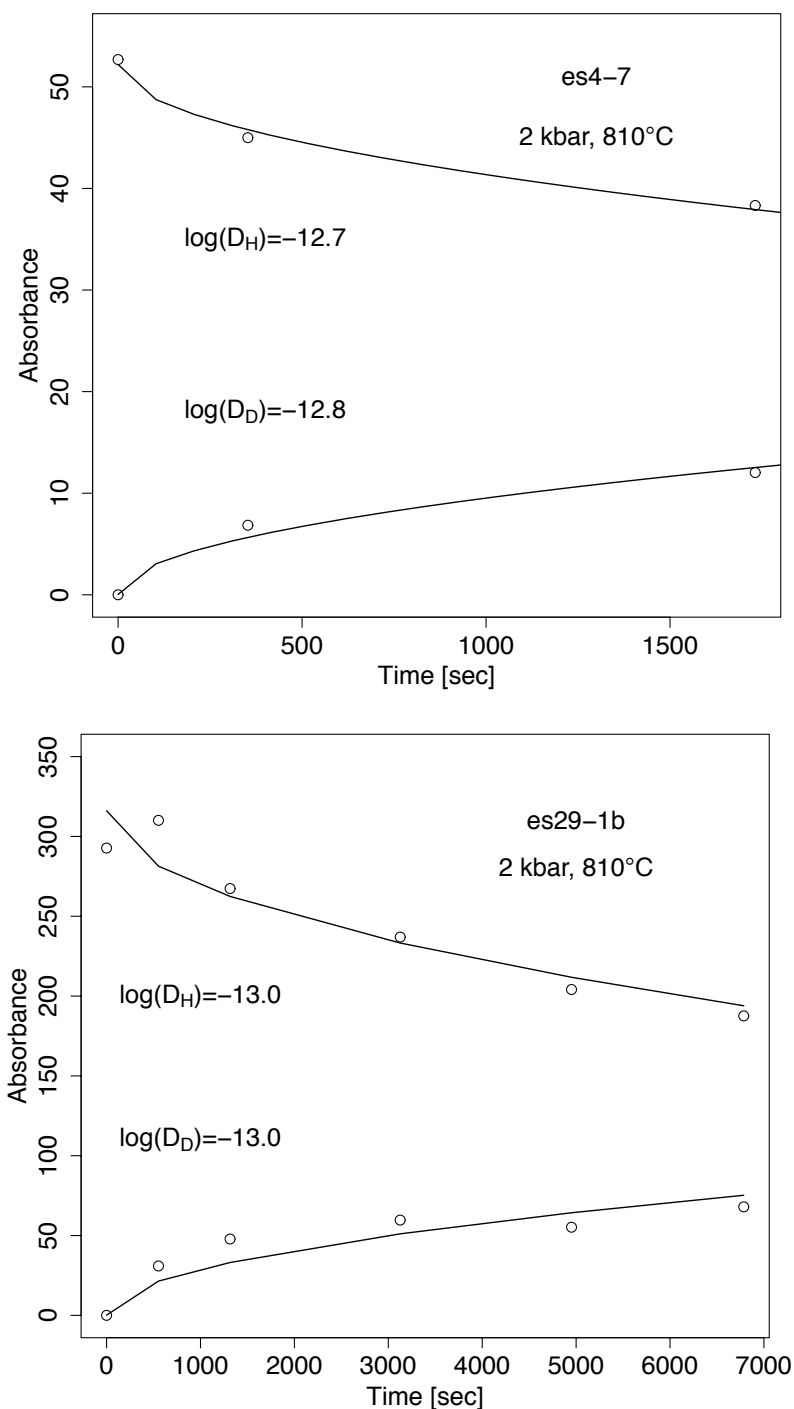


Figure B.25.: Time series of OH- and OD-absorbance (circles) with fitted diffusion equation (lines). The diffusion coefficients of es29-1b were calculated with the half thickness of the sample instead of the whole thickness because the profile measured across the sample revealed a cleavage plane parallel to the faces in the middle of the crystal plate [B.36](#).

Appendix B. Diffusion experiments

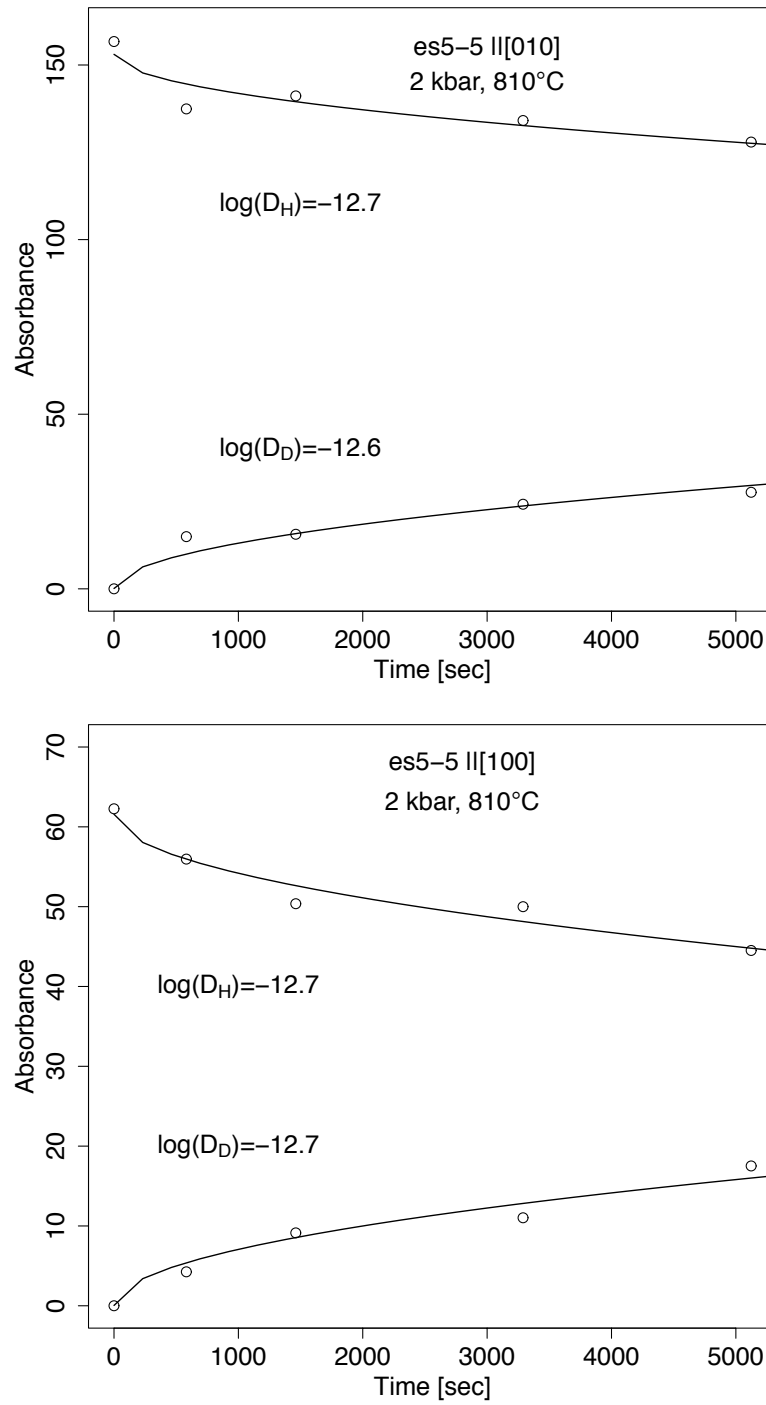


Figure B.26.: Time series of OH- and OD-absorbance (circles) with fitted diffusion equation (lines).

B.2. H/D-exchange experiments

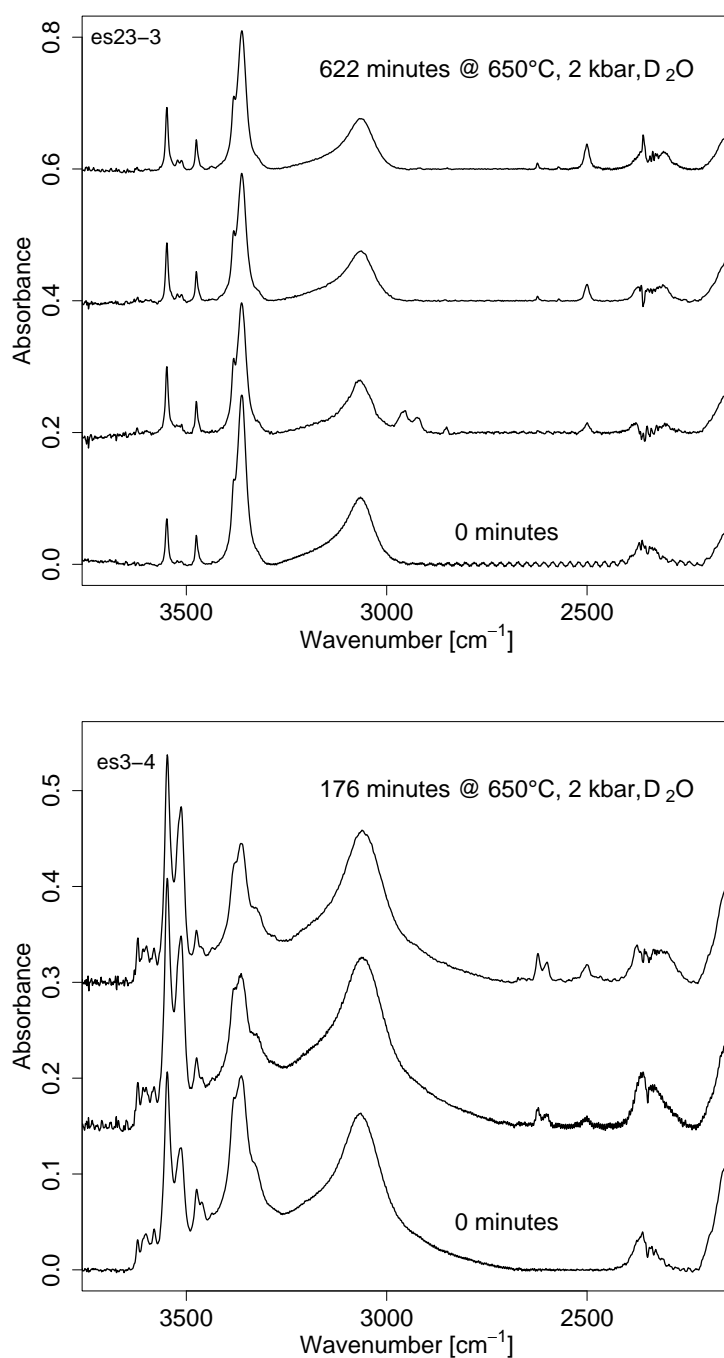


Figure B.27.: Consecutive IR-spectra showing the range of OH-absorbance between 3650 and 2800 cm^{-1} and the OD-absorbance between 2700 and 2200 cm^{-1} . Pure enstatite sample es23-2 shows some IR-bands which are characteristic for aluminium bearing enstatite. According to the EMPA analysis, Al_2O_3 -content of this sample is about 300 ppm-wt, but this small contamination has already a weak influence on the IR-spectra.

Appendix B. Diffusion experiments

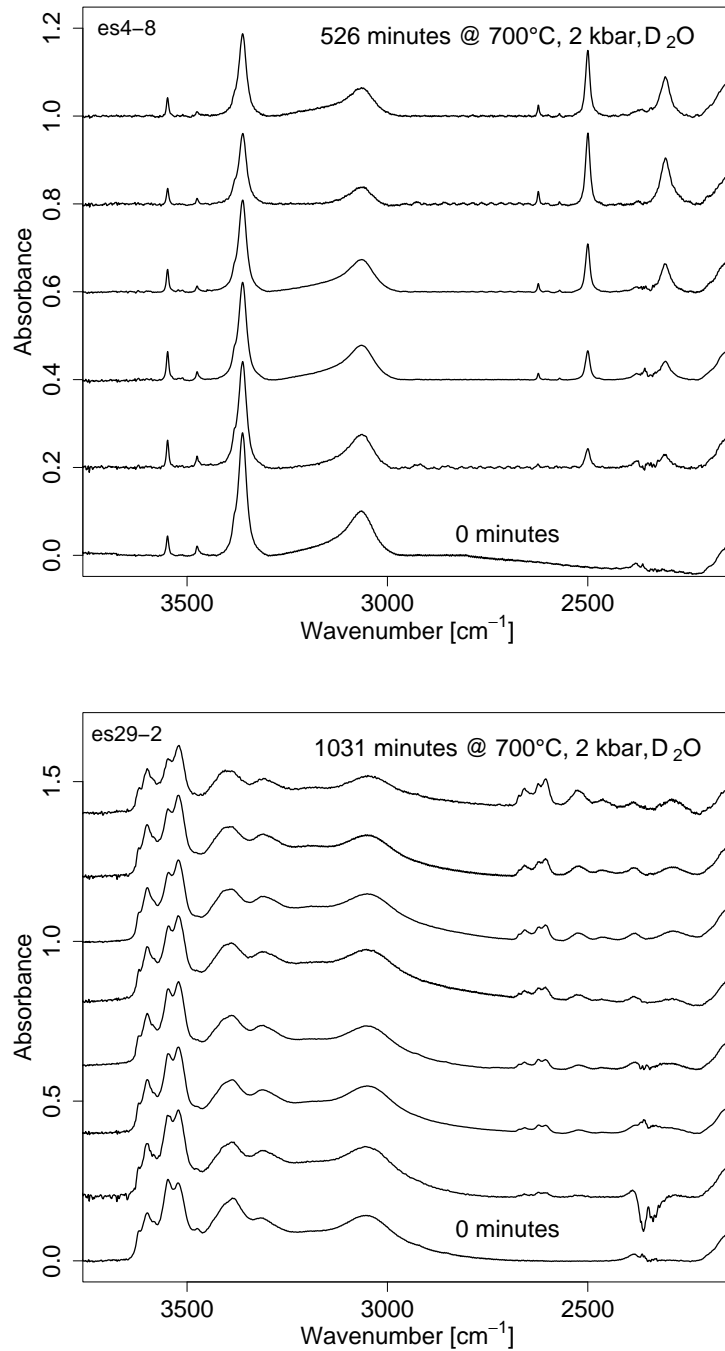


Figure B.28.: Consecutive IR-spectra showing the range of OH-absorbance between 3650 and 2800 cm⁻¹ and the OD-absorbance between 2700 and 2200 cm⁻¹. Pure enstatite sample es4-8 shows some IR-bands which are characteristic for aluminium bearing enstatite. According to the EMPA analysis, Al₂O₃-content of this sample is about 400 ppm-wt, but this small contamination has already a weak influence on the IR-spectra.

B.2. H/D-exchange experiments

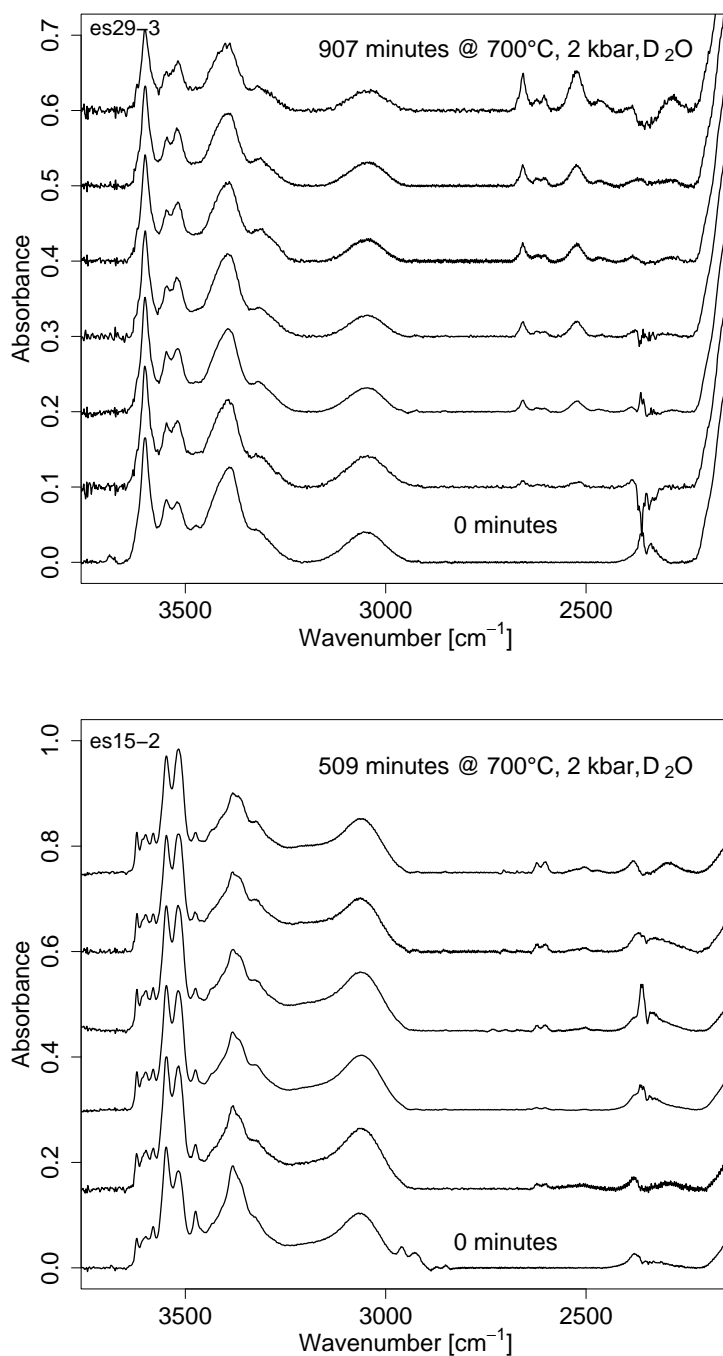


Figure B.29.: Consecutive IR-spectra showing the range of OH-absorbance between 3650 and 2800 cm⁻¹ and the OD-absorbance between 2700 and 2200 cm⁻¹. The OD-absorbance in the third lowermost spectrum of sample es15-2 is less than before, suggesting a leaky capsule in the second H/D-exchange experiment. This may be the reason for the only small change in OH- and OD-absorbances in this sample.

Appendix B. Diffusion experiments

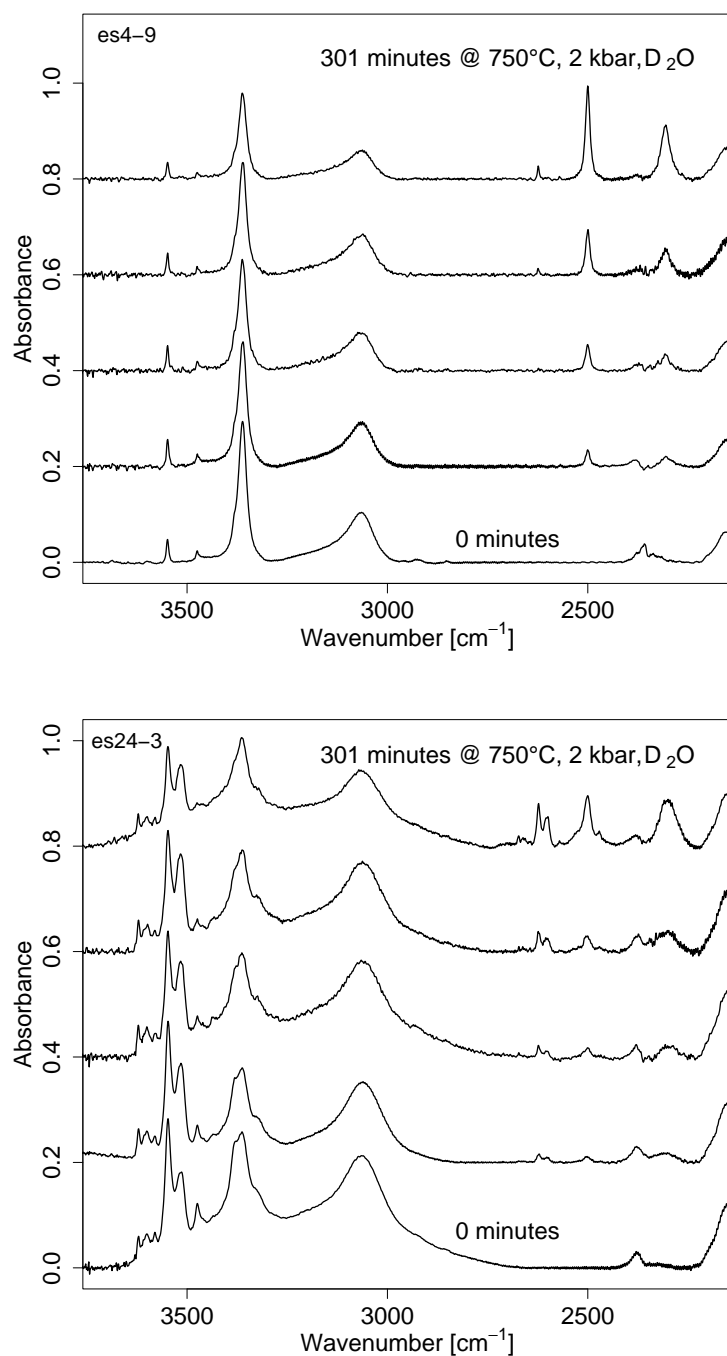


Figure B.30.: Consecutive IR-spectra showing the range of OH-absorbance between 3650 and 2800 cm^{-1} and the OD-absorbance between 2700 and 2200 cm^{-1} . Pure enstatite sample es4-9 shows some IR-bands which are characteristic for aluminium bearing enstatite. According to the EMPA analysis, Al_2O_3 -content of this sample is about 300 ppm-wt.

B.2. H/D-exchange experiments

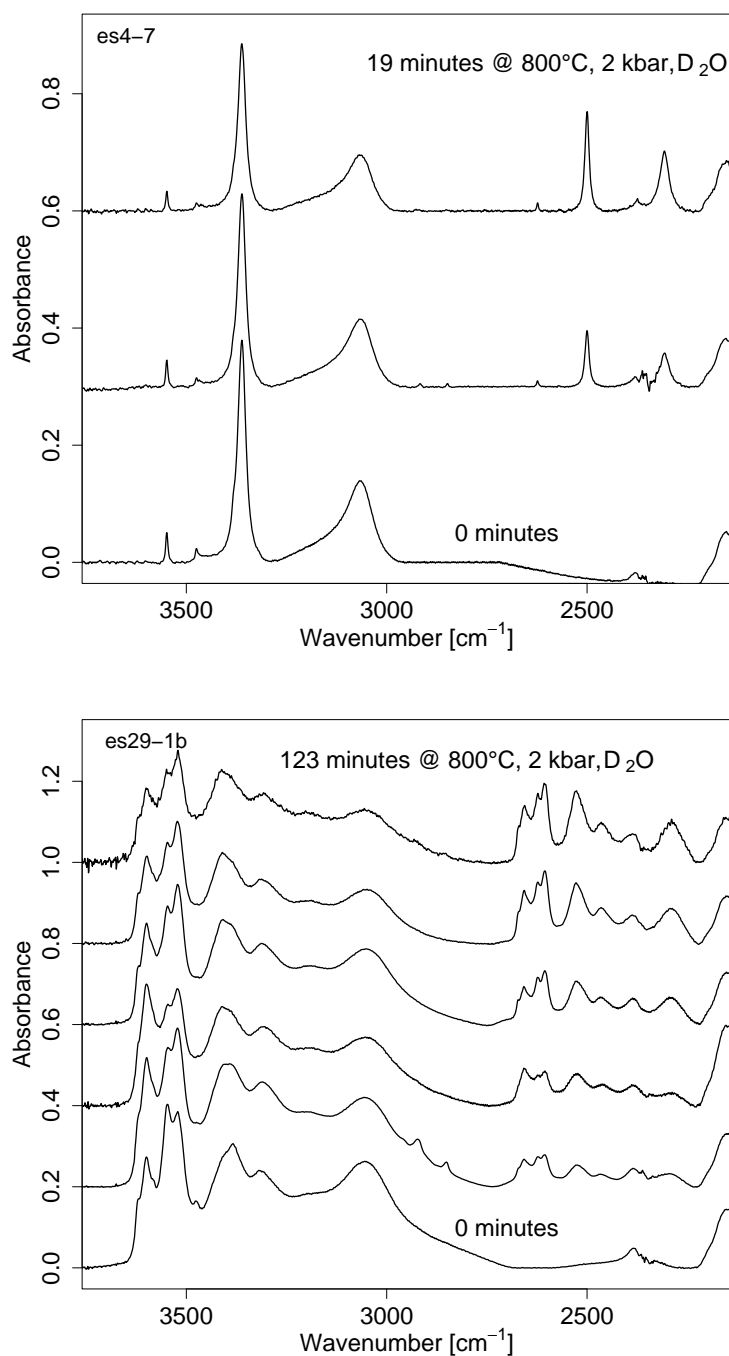


Figure B.31.: Consecutive IR-spectra showing the range of OH-absorbance between 3650 and 2800 cm^{-1} and the OD-absorbance between 2700 and 2200 cm^{-1} . Pure enstatite sample es4-7 shows some IR-bands which are characteristic for aluminium bearing enstatite. According to the EMPA analysis, Al_2O_3 -content of this sample is about 300 ppm-wt.

Appendix B. Diffusion experiments

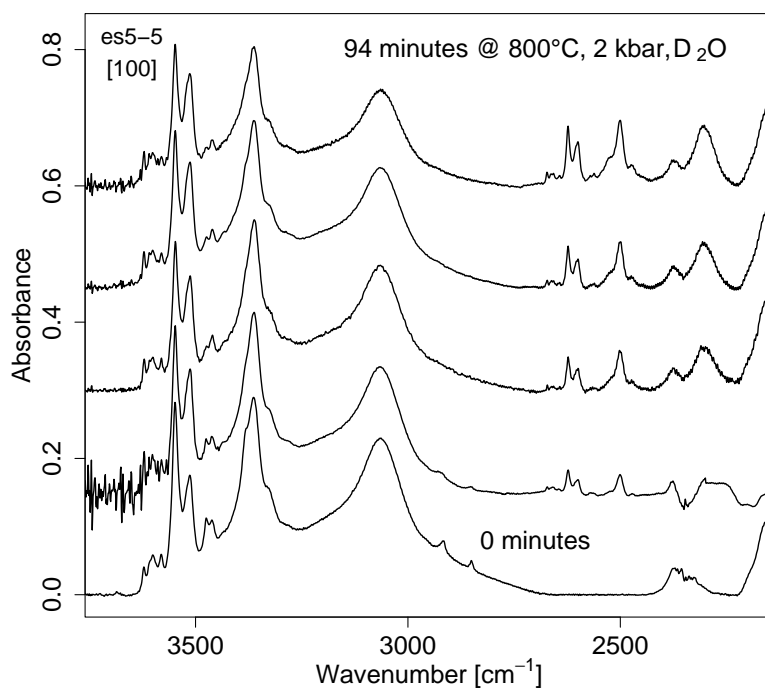


Figure B.32.: Consecutive IR-spectra showing the range of OH-absorbance between 3650 and 2800 cm^{-1} and the OD-absorbance between 2700 and 2200 cm^{-1} .

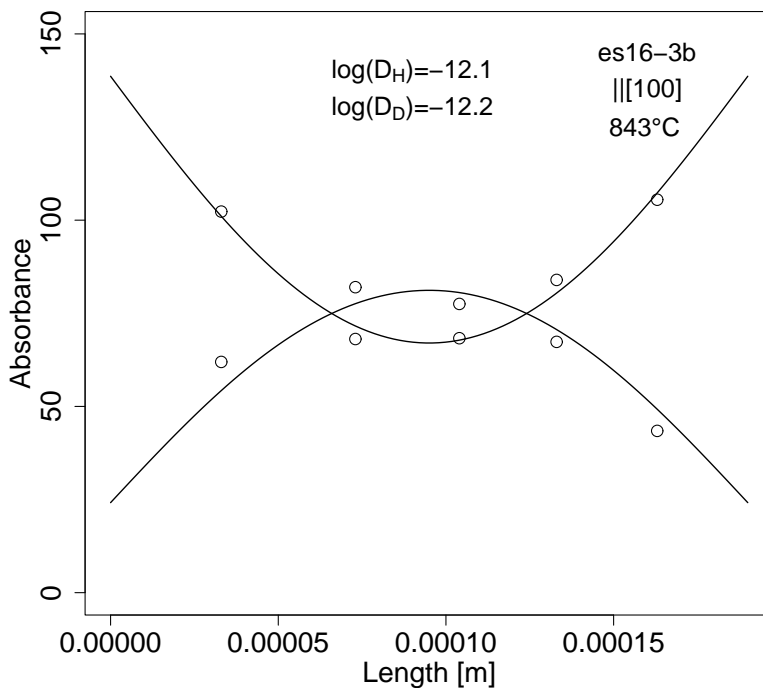


Figure B.33.: Profile of OH- and OD-absorbance, measured perpendicular to the original faces of the crystal plates.

B.2. H/D-exchange experiments

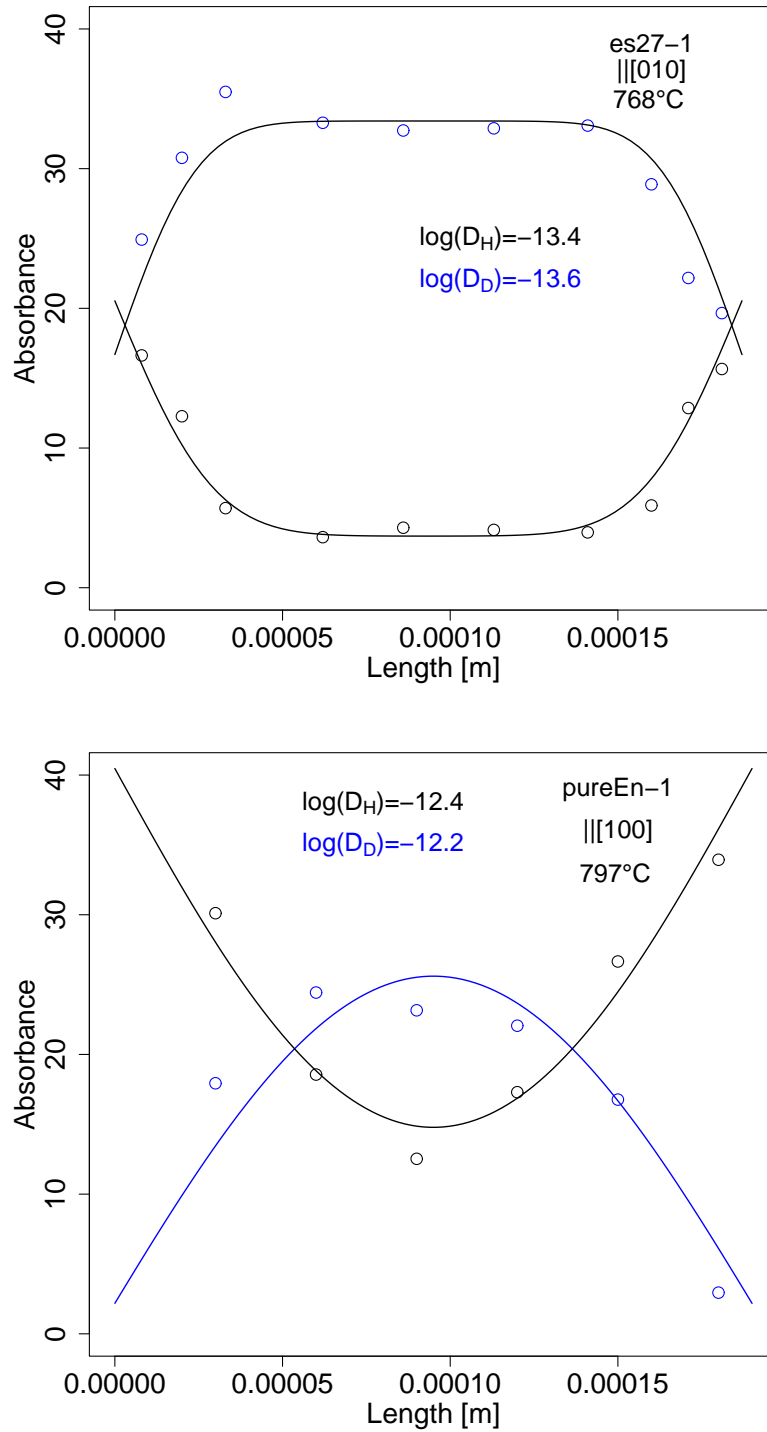


Figure B.34.: Profiles of OH- and OD-absorbance, measured perpendicular to the original faces of the crystal plates.

Appendix B. Diffusion experiments

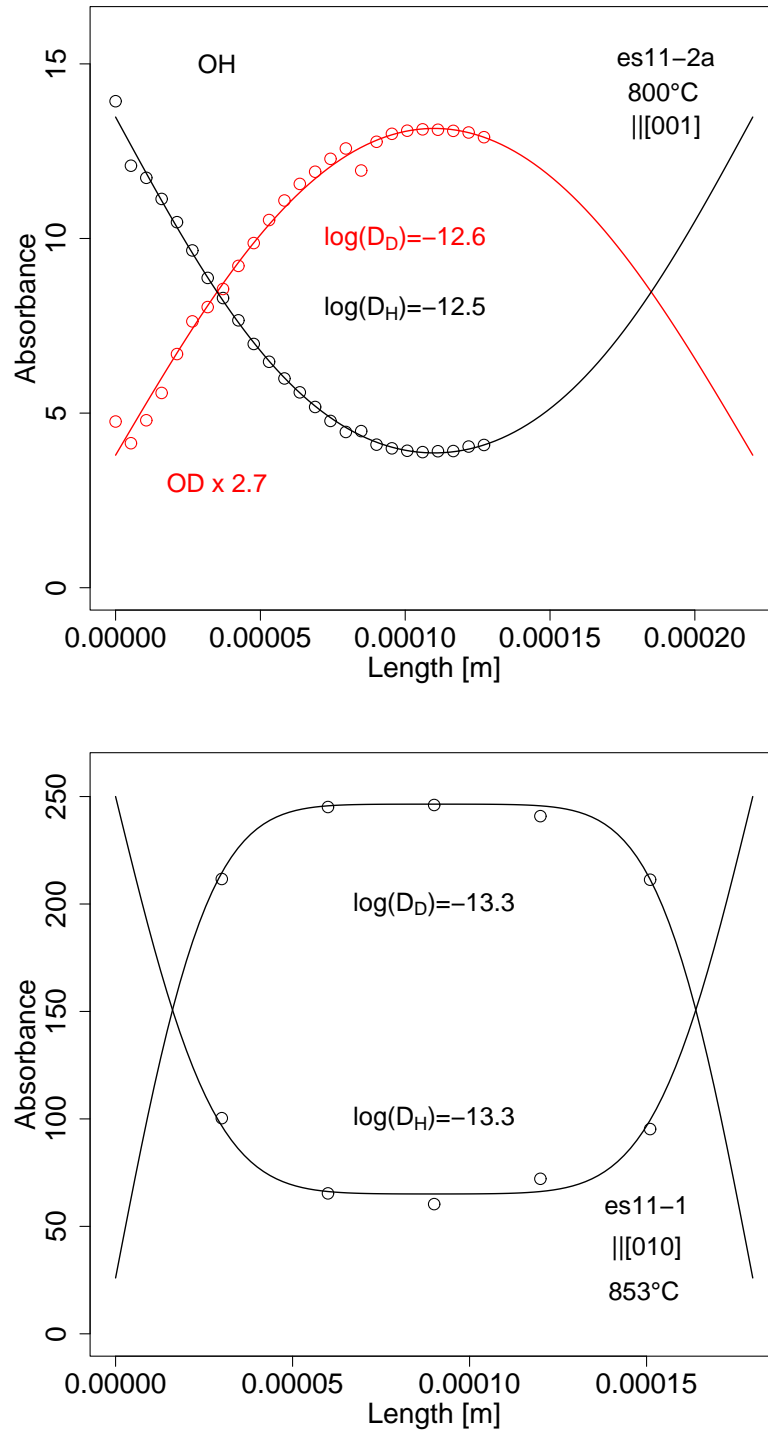


Figure B.35.: Profiles of OH- and OD-absorbance, measured perpendicular to the original faces of the crystal plates.

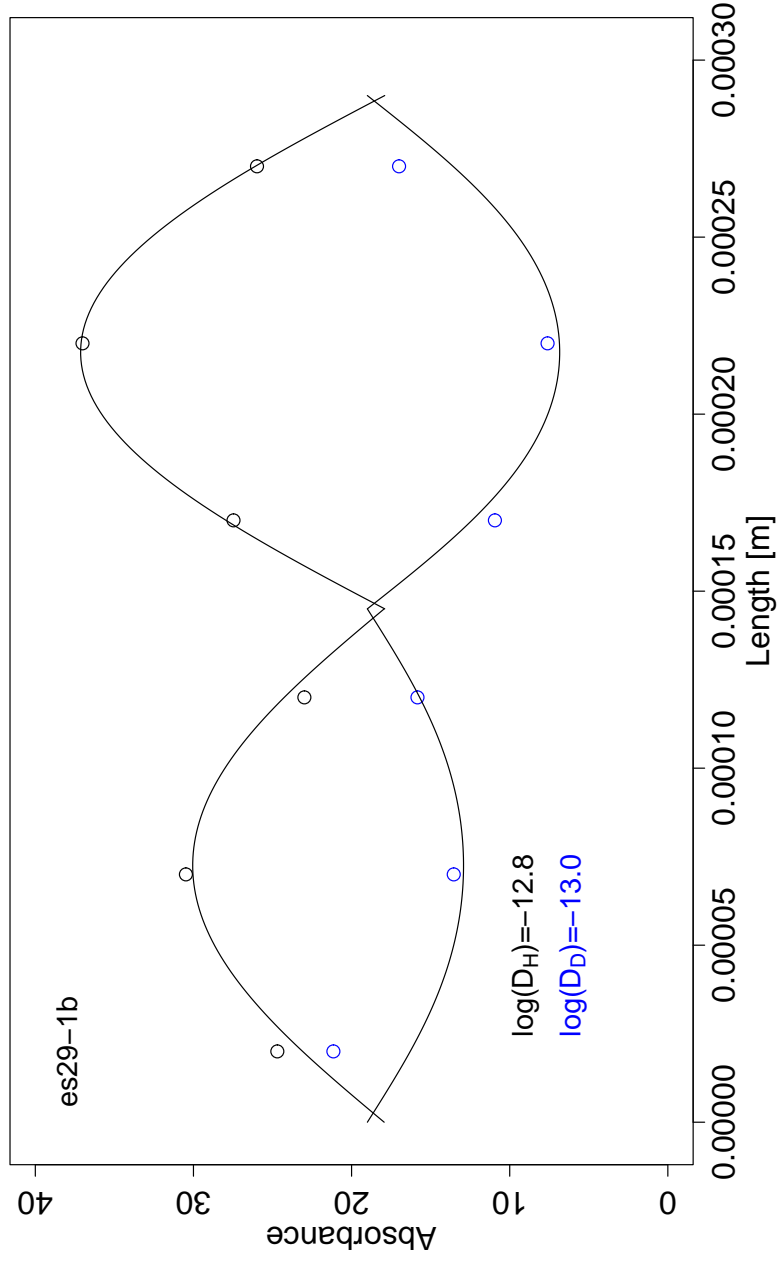


Figure B.36.: Profiles of OH- and OD-absorbance of es29-1b, measured perpendicular to the original faces of the plate. The decreasing OH- and increasing OD-absorbance in the middle of the profile reveal a cleavage plane which was originally oriented parallel to the faces of the crystal plate and was therefore invisible under the microscope. The diffusion coefficients derived from the double-arc fit were confirmed by fitting the time series with the half sample thickness.

Appendix C.

Electrical conductivity

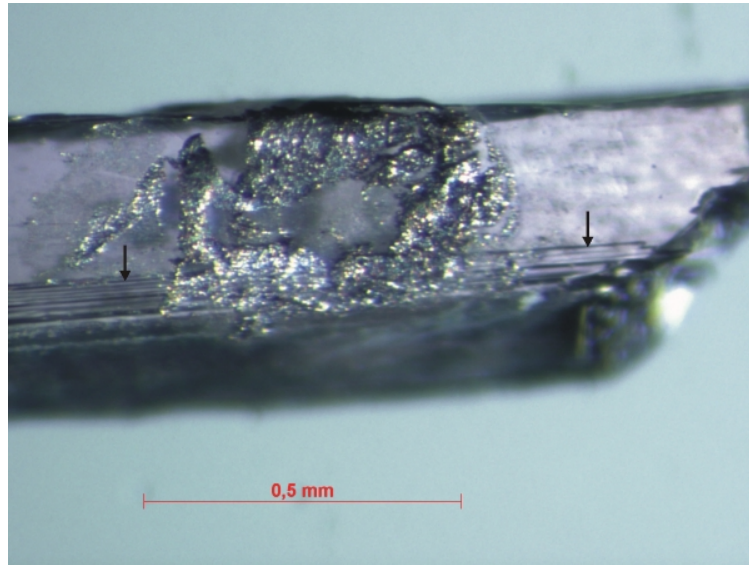


Figure C.1.: Microphotograph of sample br1-2a taken after the experiment. The arrows indicate several thin lamellae, probably talc.

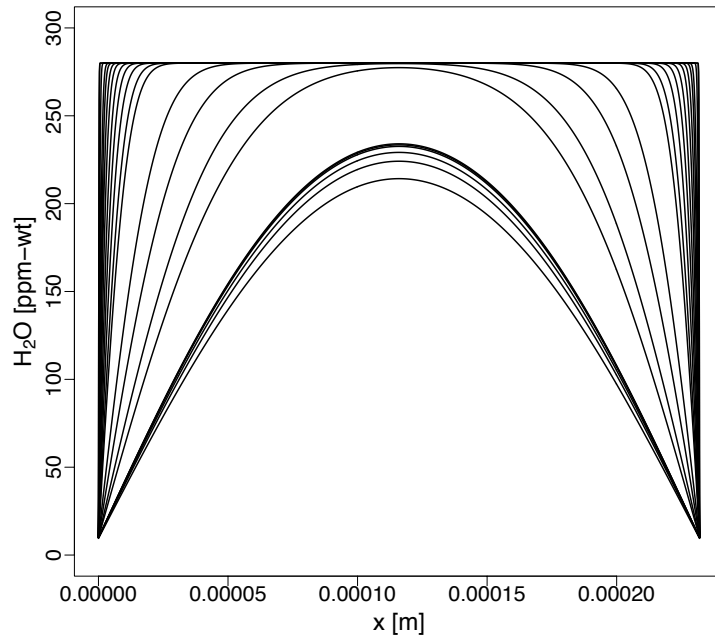


Figure C.2.: Calculated evolution of H₂O-concentration of br1-2a with time during tempering in H₂.

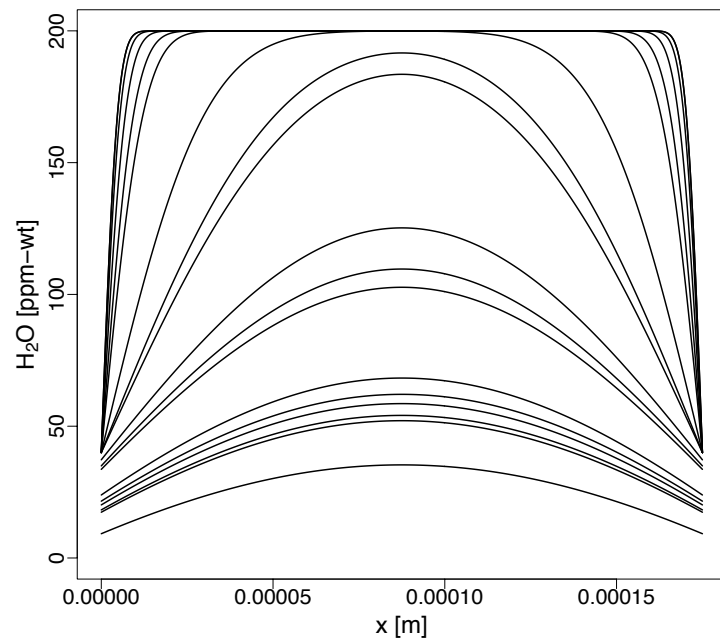


Figure C.3.: Calculated evolution of H₂O-concentration of es27-3 with time during tempering in air.

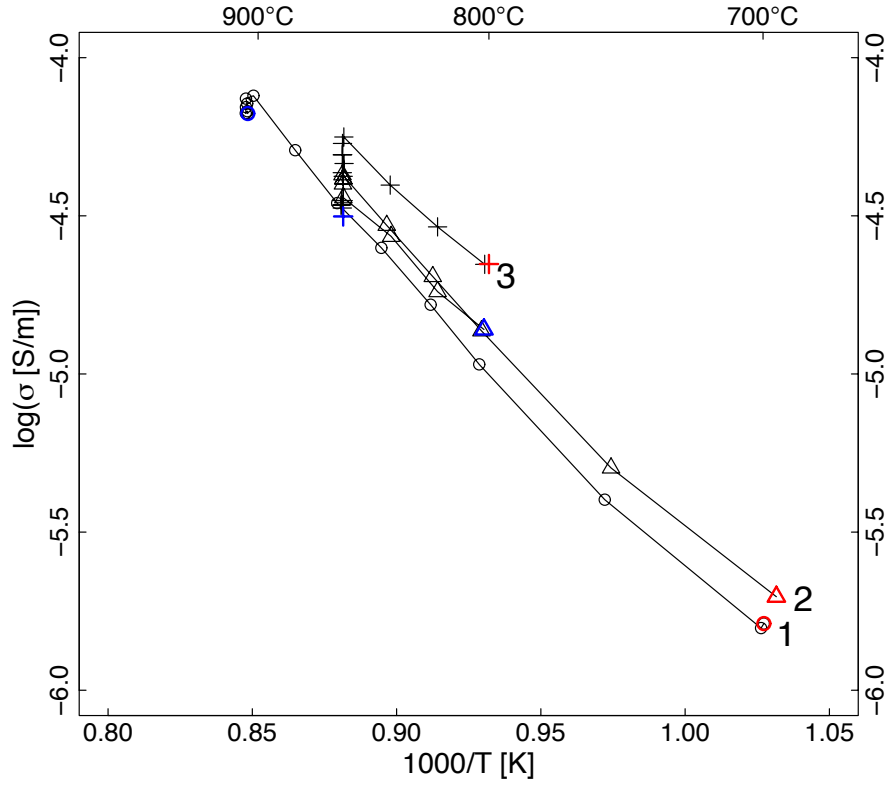


Figure C.4.: To illustrate the evolution of electrical conductivity with time, the succession of the three experiments of es27-3 are indicated by the numbers and the first (red datapoint) and the last (blue datapoint) measurement of each experiment are indicated. The fact that electrical conductivity increases from experiment to experiment but remains constant during the first two experiments, can not be explained by equilibration or alteration of the sample. The sample was quenched after each experiment and after removal from the sample-cell was analysed with FTIR-spectroscopy. To fix it again in the sample cell, a small amount of Pt-paste was added. To remove organic compounds of the Pt-paste, the sample cell assembly was fired in air at 400°C for 10 minutes. Alteration of the sample through this heat treatment is very unlikely.

Bibliography

- Anderson, A. and Burnham, C. (1965). The solubility of quartz in supercritical water. *Am. J. Sci.*, 263:494–511.
- Asimow, P., Dixon, J., and Langmuir, C. (2004). A hydrous melting and fractionation model for mid-ocean ridge basalts: Application to the Mid-Atlantic Ridge near the Azores. *Geochem. Geophys. Geosyst.*, 5(1).
- Baba, K., Tarits, P., Chave, A., Evans, R., Hirth, G., and Macki, R. (2006). Electrical structure beneath the northern MELT line on the East Pacific Rise at 15°45'S. *Geophys. Res. Lett.*, 33:L22301.
- Bahr, K. and Duba, A. (2000). Is the asthenosphere electrically anisotropic? *Earth Planet. Sci. Lett.*, 178:87–95.
- Bahr, K. and Simpson, F. (2002). Electrical anisotropy below slow- and fast-moving plates: paleoflow in the upper mantle? *Science*, 295:1270–1272.
- Bell, D. and Rossman, G. (1992). Water in Earth's mantle: The role of nominally anhydrous minerals. *Science*, 255:1391–1397.
- Bolfan-Casanova, N. (2005). Water in the earth's mantle. *Mineral. Mag.*, 69(3):229–257.
- Bolfan-Casanova, N., Keppler, H., and Rubie, D. (2000). Water partitioning between nominally anhydrous minerals in the MgO-SiO₂-H₂O system up to 24 GPa: implications for the distribution of water in the Earth's mantle. *Earth Planet. Sci. Lett.*, 182:209–221.
- Bolfan-Casanova, N., Keppler, H., and Rubie, D. (2003). Water partitioning at 660 km depth and evidence for very low water solubility in magnesium silicate perovskite. *Geophys. Res. Lett.*, 30(17):1905.
- Bolfan-Casanova, N., Mackwell, S., Keppler, H., McCammon, C., and Rubie, D. (2002). Pressure dependence of H solubility in magnesiowüstite up to 25 GPa: Implications for the storage of water in the Earth's lower mantle. *Geophys. Res. Lett.*, 29:1029–1032.

Bibliography

- Bromiley, G., Keppler, H., McCammon, C., Bromiley, F., and Jacobsen, S. (2004). Hydrogen solubility and speciation in natural, gem-quality chromian diopside. *Am. Mineral.*, 89:941–949.
- Carpenter Woods, S., Mackwell, S., and Dyar, D. (2000). Hydrogen in diopside: diffusion profiles. *Am. Mineral.*, 85(3–4):480–487.
- Carslaw, H. and Jaeger, J. (1959). *Conduction of heat in solids*. Oxford Science Publications.
- Chen, S., Hiraga, T., and Kohlstedt, D. (2006). Water weakening of clinopyroxene in the dislocation creep regime. *J. Geophys. Res.*, 111:B08203.
- Crank, J. (1975). *The Mathematics of Diffusion*. Oxford University Press, second edition.
- Dai, L. and Karato, S. (2009a). Electrical conductivity of orthopyroxene: Implications for the water content of the asthenosphere. *Proc. Jpn. Acad., Ser. B*, 85:466–475.
- Dai, L. and Karato, S. (2009b). Electrical conductivity of wadsleyite at high temperatures and high pressures. *Earth Planet. Sci. Lett.*, 287(1-2):277–283.
- Demouchy, S. (2010). Diffusion of hydrogen in olivine grain boundaries and implications for the survival of water-rich zones in the Earth’s mantle. *Earth Planet. Sci. Lett.*, 295(1-2):305–313.
- Demouchy, S., Jacobsen, S., Gaillard, F., and Stern, C. (2006). Rapid magma ascent recorded by water diffusion profiles in mantle olivine. *Geology*, 34(6):429–432.
- Dixon, J., Dixon, T., Bell, D., and Malservisi, R. (2004). Lateral variation in the upper mantle viscosity: role of water. *Earth Planet. Sci. Lett.*, 222:451–467.
- Duba, A., Dennison, M., Irving, A., Thornber, C., and Huebner, J. (1979). Electrical conductivity of aluminous orthopyroxene. *Lunar and Planetary Institute*, pages 318–319.
- Duba, A., Heard, H., and Schock, R. (1976). Electrical conductivity of orthopyroxene to 1400°C and the resulting selenotherm. *Proc. Lunar Sci. Conf. 7th*, 3:3173–3181.
- Ducea, M. N. and Park, S. K. (2000). Enhanced mantle conductivity from sulfide minerals, Southern Sierra Nevada, California. *Geophys. Res. Lett.*, 27(16):2405–2408.

- Frey, F. and Prinz, M. (1978). Ultramafic inclusions from San Carlos, Arizona: Petrologic and geochemical data bearing on their petrogenesis. *Earth Planet. Sci. Lett.*, 38(1):129–176.
- Frost, D. (2008). The upper mantle and the transition zone. *Elements*, 4:171–176.
- Funke, K. (2002). *Skript Apparative Methoden in der Physikalischen Chemie: Impedanzspektroskopie*. Institut für Physikalische Chemie, Universität Münster.
- Gaetani, G. and Grove, T. (1998). The influence of water on melting of mantle peridotite. *Contrib. Mineral. Petrol.*, 131(4):323–346.
- Gaillard, F., Malki, M., Iacono-Marziano, G., Pichavant, M., and Scaillet, B. (2008). Carbonatite melts and electrical conductivity in the asthenosphere. *Science*, 322:1363–1365.
- Gatzemeier, A. and Moorkamp, M. (2005). 3D modelling of electrical anisotropy from electromagnetic array data: hypothesis testing for different upper mantle conduction mechanisms. *Phys. Earth Planet. Inter.*, 149:225–242.
- Glover, P. (1996). Graphite and electrical conductivity in the lower continental crust: a review. *Phys. Chem. Earth*, 21(4):279–287.
- Green, D., Hibberson, W., Kovács, I., and Rosenthal, A. (2010). Water and its influence on the lithosphere-asthenosphere boundary. *Nature*, 467:448–451.
- Heinrich, W. and Besch, T. (1992). Thermal history of the upper mantle beneath a young back-arc extensional zone: ultramafic xenoliths from San Luis Potosí, Central Mexico. *Contrib. Mineral. Petrol.*, 111(1):126–142.
- Hercule, S. and Ingrin, J. (1999). Hydrogen in diopside: Diffusion, kinetics of extraction-incorporation, and solubility. *Am. Mineral.*, 84:1577–1587.
- Hier-Majumder, S., Anderson, I., and Kohlstedt, D. (2005). Influence of protons on Fe-Mg interdiffusion in olivine. *J. Geophys. Res.*, 110:B02202.
- Hier-Majumder, S. and Kohlstedt, D. (2006). Role of dynamic grain boundary wetting in fluid circulation beneath volcanic arcs. *Geophys. Res. Lett.*, 33:L08305.
- Hiraga, T., Anderson, I., and Kohlstedt, D. (2003). Chemistry of grain boundaries in mantle rocks. *Am. Mineral.*, 88:1015–1019.

Bibliography

- Hiraga, T., Anderson, I., and Kohlstedt, D. (2004). Grain boundaries as reservoirs of incompatible elements in the Earth's mantle. *Nature*, 427:699–703.
- Hirschmann, M. (2006). Water, melting, and the Deep Earth H₂O cycle. *Annu. Rev. Earth Planet. Sci.*, 34:629–653.
- Hirth, G., Evans, R., and Chave, A. (2000). Comparison of continental and oceanic mantle electrical conductivity: Is the archaic lithosphere dry? *Geochem. Geophys. Geosyst.*, 1:2000GC000048.
- Hirth, G. and Kohlstedt, D. (1996). Water in the oceanic upper mantle: implications for rheology, melt extraction and the evolution of the lithosphere. *Earth Planet. Sci. Lett.*, 144(1–2):93–108.
- Hofmann, A. (1997). Mantle geochemistry: the message from oceanic volcanism. *Nature*, 385:219–229.
- Hofmeister, A. (2004). Enhancement of radiative transfer in the upper mantle by OH in minerals. *Phys. Earth Planet. Inter.*, 146(3–4):483–495.
- Hofmeister, A., Pertermann, M., Branlund, J., and Whittington, A. (2006). Geophysical implications of reduction in thermal conductivity due to hydration. *Geophys. Res. Lett.*, 33:L11310.
- Huang, X., Xu, Y., and Karato, S. (2005). Water content in the transition zone from electrical conductivity of wadsleyite and ringwoodite. *Nature*, 434:746–749.
- Huebner, J. and Voigt, D. (1988). Electrical conductivity of diopside: evidence for oxygen vacancies. *Am. Mineral.*, 73:1235–1254.
- Ingrin, J., Hercule, S., and Charton, T. (1995). Diffusion of hydrogen in diopside: Results of dehydration experiments. *J. Geophys. Res.*, 100:15,489–15,499.
- Jernberg, P. and Sundqvist, T. (1983). *A versatile Mößbauer analysis program*. Uppsala University report, Institute of Physics (UIP-1090).
- Jung, H. and Karato, S. (2001). Water-induced fabric transitions in olivine. *Science*, 293(5534):1460–1463.
- Karato, S. (1990). The role of hydrogen in the electrical conductivity of the upper mantle. *Nature*, 347:272–273.
- Karato, S. and Jung, H. (1998). Water, partial melting and the origin of the seismic low velocity and high attenuation zone in the upper mantle. *Earth Planet. Sci. Lett.*, 157:193–207.

- Karato, S., Jung, H., Katayama, I., and Skemer, P. (2008). Geodynamic significance of seismic anisotropy of the upper mantle: New insights from laboratory studies. *Annu. Rev. Earth Planet. Sci.*, 36:59–95.
- Kerrick, D. and Connolly, J. (2001). Metamorphic devolatilization of subducted marine sediments and the transport of volatiles into the Earth’s mantle. *Nature*, 411:293–296.
- Kitamura, M., Kondoh, S., Morimoto, N., Miller, G., Rossman, G., and Putnis, A. (1987). Planar oh-bearing defects in mantle olivine. *Nature*, 328:143–145.
- Kohlstedt, D., Keppler, H., and Rubie, D. (1996). Solubility of water in the α , β , and γ phases of $(\text{Mg,Fe})_2\text{SiO}_4$. *Contrib. Mineral. Petrol.*, 123(4):345–357.
- Kohlstedt, D. and Mackwell, S. (1998). Diffusion of hydrogen and intrinsic point defects in olivine. *Z. Phys. Chem.*, 207:147–162.
- Kohn, S., Roome, B., Smith, M., and Howes, A. (2005). Testing a potential mantle geohygrometer; the effect of dissolved water on the intracrystalline partitioning of Al in orthopyroxene. *Earth Planet. Sci. Lett.*, 238:342–350.
- Kovács, I., O’Neill, H., Hermann, J., and Hauri, E. (2010). Site-specific infrared O-H absorption coefficients for water substitution into olivine. *Am. Mineral.*, 95:292–299.
- Leibecker, J., Gatzemeier, A., Hönig, M., Kuras, O., and Soyer, W. (2002). Evidence of electrical anisotropic structures in the lower crust and the upper mantle beneath the Rhenish Shield. *Earth Planet. Sci. Lett.*, 202:289–302.
- Lemaire, C., Kohn, S., and Brooker, R. (2004). The effect of silica activity on the incorporation mechanisms of water in synthetic forsterite: a polarised infrared spectroscopic study. *Contrib. Mineral. Petrol.*, 147:48–57.
- Libowitzky, E. and Rossmann, G. (1997). An IR absorption calibration for water in minerals. *Am. Mineral.*, 82:1111–1115.
- Lizzaralde, D., Chave, A., Hirth, G., and Schultz, A. (1995). Northeastern Pacific mantle conductivity profile from long-period magnetotelluric sounding using Hawaii-to-California submarine cable data. *J. Geophys. Res.*, 100(B9):17,837–17,854.
- Mackwell, S., Kohlstedt, D., and Paterson, M. (1985). The role of water in the deformation of olivine single crystals. *J. Geophys. Res.*, 90(B13):11,319–11,333.

Bibliography

- Manthilake, M., Matsusaki, T., Yoshino, T., Yamashita, S., Ito, E., and Katsura, T. (2009). Electrical conductivity of wadsleyite as a function of temperature and water content. *Phys. Earth Planet. Inter.*, 174(1–4):10–18.
- Matveev, S., O'Neill, H., Ballhaus, C., Taylor, W., and Green, D. (2001). Effect of silica activity on OH⁻ IR spectra of olivine: implications for low-aSiO₂ mantle metasomatism. *J. Petrol.*, 42:721–729.
- Médard, E. and Grove, T. (2008). The effect of H₂O on the olivine liquidus of basaltic melts: experiments and thermodynamic models. *Contrib. Mineral. Petrol.*, 155:417–432.
- Mei, S. and Kohlstedt, D. L. (2000a). Influence of water on plastic deformation of olivine aggregates 1. Diffusion creep regime. *J. Geophys. Res.*, 105(B9):21457–21469.
- Mei, S. and Kohlstedt, D. L. (2000b). Influence of water on plastic deformation of olivine aggregates 2. Dislocation creep regime. *J. Geophys. Res.*, 105(B9):21471–21481.
- Meibom, A. and Anderson, D. (2003). The statistical upper mantle assemblage. *Earth Planet. Sci. Lett.*, 217:123–139.
- Mierdel, K. and Keppler, H. (2004). The temperature dependence of water solubility in enstatite. *Contrib. Mineral. Petrol.*, 148:305–311.
- Novak, A. (1973). Hydrogen bonding in solids. correlation of spectroscopic and crystallographic data. In *Plenary lecture at the first European Crystallographic Meeting, Bordeaux*.
- Özkan, O. and Moulson, A. (1970). The electrical conductivity of single-crystal and polycrystal aluminium oxide. *J. Phys. D: Appl. Phys.*, 3(6):983–987.
- Pearson, D., Canil, D., and Shirey, S. (2003). Mantle samples included in volcanic rocks: Xenoliths and diamonds. In Holland, H. D. and Turekian, K. K., editors, *Treatise on Geochemistry*, pages 171–275. Pergamon, Oxford.
- Peslier, A. (2010). A review of water contents of nominally anhydrous natural minerals in the mantles of Earth, Mars and the Moon. *J. Volcanol. Geotherm. Res.*, 197:239–258.
- Peslier, A. H. and Luhr, J. F. (2006). Hydrogen loss from olivines in mantle xenoliths from Simcoe (USA) and Mexico: Mafic alkalic magma ascent rates and water budget of the sub-continental lithosphere. *Earth Planet. Sci. Lett.*, 242:302–319.

- Prechtel, F. and Stalder, R. (2010). FTIR spectroscopy with a focal plane array detector: A novel tool to monitor the spatial OH-defect distribution in single crystals applied to synthetic enstatite. *Am. Mineral.*, 95:888–891.
- Ranero, C., Morgan, F., McIntosh, K., and Reichert, C. (2003). Bending-related faulting and mantle serpentinization at the Middle America trench. *Nature*, 425:367–373.
- Rauch, M. and Keppler, H. (2002). Water solubility in orthopyroxene. *Contrib. Mineral. Petrol.*, 143:525–536.
- Roberts, J. and Tyburczy, J. (1999). Partial-melt electrical conductivity: Influence of melt composition. *J. Geophys. Res.*, 104(B4):7055–7065.
- Rüpke, L., Morgana, J., Hort, M., and Connolly, J. (2004). Serpentine and the subduction zone water cycle. *Earth Planet. Sci. Lett.*, 223:17–34.
- Schultz, A., Kurtz, R. D., Chave, A. D., and Jones, A. G. (1993). Conductivity discontinuities in the upper mantle beneath a stable craton. *Geophys. Res. Lett.*, 20(24):2941–2944.
- Shito, A., Karato, S., Matsukage, K., and Nishihara, Y. (2006). Towards mapping of three-dimensional distribution of water in the upper mantle from velocity and attenuation tomography. In *Earth’s deep water cycle*, number 168 in Geophysical Monograph Series. American Geophysical Union.
- Simpson, F. (2002). Intensity and direction of lattice-preferred orientation of olivine: area electrical and seismic anisotropies of the Australian mantle reconcilable? *Earth Planet. Sci. Lett.*, 203:535–547.
- Simpson, F. and Tommasi, A. (2005). Hydrogen diffusivity and electrical conductivity of a peridotite mantle. *Geophys. J. Int.*, 160:1092–1102.
- Skemer, P. and Karato, S. (2008). Sheared lherzolite xenoliths revisited. *J. Geophys. Res.*, 113:B07205.
- Skogby, H. and Rossman, G. (1989). OH[−] in pyroxene: an experimental study of incorporation mechanisms and stability. *Am. Mineral.*, 74:1059–1069.
- Smyth, J. (1989). Electrostatic characterization of oxygen in minerals. *Geochim. Cosmochim. Acta*, 53:1101–1110.
- Smyth, J., Kawamoto, T., Jacobsen, S., Swope, R., Hervig, R., and Holloway, J. (1997). Crystal structure of monoclinic hydrous wadsleyite [β -(Mg,Fe)₂SiO₄]. *Am. Mineral.*, 82:270–275.

Bibliography

- Smyth, J., Mierdel, K., Keppler, H., Langenhorst, F., Dubrovinsky, L., and Nestola, F. (2007). Crystal chemistry of hydration in aluminous orthopyroxene. *Am. Mineral.*, 92:973–976.
- Sommer, H., Regenauer-Lieb, K., Gasharova, B., and Siret, D. (2008). Grain boundaries: a possible water reservoir in the Earth’s mantle? *Mineral. Petrol.*, 94:1–8.
- Stalder, R. (2002). Synthesis of enstatite single crystals at high pressure. *Eur. J. Mineral.*, 14:637–640.
- Stalder, R. (2004). Influence of Fe, Cr and Al on hydrogen incorporation in orthopyroxene. *Eur. J. Mineral.*, 16:703–711.
- Stalder, R. and Behrens, H. (2006). D/H exchange in pure and Cr-doped enstatite: implications for hydrogen diffusivity. *Phys. Chem. Minerals*, 33:601–611.
- Stalder, R., Klemme, S., Ludwig, T., and Skogby, H. (2005). Hydrogen incorporation in orthopyroxene: interaction of different trivalent cations. *Contrib. Mineral. Petrol.*, 150:473–485.
- Stalder, R. and Ludwig, T. (2007). OH incorporation in synthetic diopside. *Eur. J. Mineral.*, 19:373–380.
- Stalder, R., Purwin, H., and Skogby, H. (2007). Influence of Fe on hydrogen diffusivity in orthopyroxene. *Eur. J. Mineral.*, 19:899–903.
- Stalder, R. and Skogby, H. (2002). Hydrogen incorporation in enstatite. *Eur. J. Mineral.*, 14:1139–1144.
- Stalder, R. and Skogby, H. (2003). Hydrogen diffusion in synthetic and natural orthopyroxene. *Phys. Chem. Minerals*, 30:12–19.
- Stalder, R. and Skogby, H. (2007). Dehydration mechanisms in synthetic Fe-bearing enstatite. *Eur. J. Mineral.*, 19:201–216.
- Stocker, R. L. (1978). Variation of electrical conductivity in enstatite with oxygen partial pressure: Comparison of observed and predicted behavior. *Phys. Earth Planet. Inter.*, 17:34–40.
- Sundberg, M. and Cooper, R. (2008). Crystallographic preferred orientation produced by diffusional creep of harzburgite: Effects of chemical interactions among phases during plastic flow. *J. Geophys. Res.*, 113:B12208.

- ten Grotenhuis, S., Drury, M., Spiers, C., and Peach, C. (2005). Melt distribution in olivine rocks based on electrical conductivity measurements. *J. Geophys. Res.*, 110:B12201.
- Tenner, T., Hirschmann, M., Withers, A., and Hervig, R. (2009). Hydrogen partitioning between nominally anhydrous upper mantle minerals and melt between 3 and 5 GPa and applications to hydrous peridotite partial melting. *Chem. Geol.*, 262:42–56.
- Voigt, R., Seifert, K.-F., and Will, G. (1979). Die elektrische Leitfähigkeit von Pyroxenen der Reihe $\text{MgSiO}_3\text{--FeSiO}_3$ bei 10 und 20 kbar unter definierten thermodynamischen Bedingungen. *N. Jb. Miner. Mh.*, 7:296–308.
- Wang, D., Li, H., Yi, L., and Shi, B. (2008). The electrical conductivity of upper-mantle rocks: water content in the upper mantle. *Phys. Chem. Minerals*, 35:157–162.
- Wang, D., Mookherjee, M., Xu, Y., and Karato, S. (2006). The effect of water on the electrical conductivity of olivine. *Nature*, 443:977–980.
- Wang, Z., Ji, S., and Dresen, G. (1999). Hydrogen-enhanced electrical conductivity of diopside crystals. *Geophys. Res. Lett.*, 26(6):799–802.
- Watson, H., Roberts, J., and Tybureczy, J. (2010). Effect of conductive impurities on electrical conductivity in polycrystalline olivine. *Geophys. Res. Lett.*, 37:L02302.
- Will, G., Cemic, L., Hinze, E., Seifert, K.-F., and Voigt, R. (1979). Electrical conductivity measurements on olivines and pyroxenes under defined thermodynamic activities as a function of temperature and pressure. *Phys. Chem. Minerals*, 4:189–197.
- Xu, Y. and Shankland, T. J. (1999). Electrical conductivity of orthopyroxene and its high pressure phases. *Geophys. Res. Lett.*, 26(17):2645–2648.
- Xu, Y., Shankland, T. J., and Duba, A. (2000). Pressure effect on electrical conductivity of mantle olivine. *Phys. Earth Planet. Inter.*, 118:149–161.
- Yoshino, T., Manthilake, G., Matsuzaki, T., and Katsura, T. (2008). Dry mantle transition zone inferred from the conductivity of wadsleyite and ringwoodite. *Nature*, 451:326–329.
- Yoshino, T., Matsuzaki, T., and Shatskiy (2009). The effect of water on the electrical conductivity of olivine aggregates and its implications for the electrical structure of the upper mantle. *Earth Planet. Sci. Lett.*, 288:291–300.

Bibliography

Yoshino, T., Matsuzaki, T., Yamashita, S., and Katsura, T. (2006). Hydrous olivine unable to account for conductivity anomaly at the top of the asthenosphere. *Nature*, 443:973–976.